Elucidating structure-function relationships in a functionallygraded quick-release biointerface

Lucia Youssef

Department of Chemistry

McGill University , Montreal

Quebec, Canada

FEBRUARY 17, 2025

A thesis submitted to McGill University in partial fulfillment of the

requirements of the degree of Doctor of Philosophy

©Lucia Youssef, 2025

Table on Content

Abstra	ct4
Résum	né5
Ackno	wledgements8
Contri	bution to Original Knowledge9
Contri	bution of Authors11
List of	Figures
List of	Abbreviations
Chapte	er 1
Introd	uction
1.	Comprehensive Literature Review
1.1.	Interactions at Interfaces
1.2.	Mechanical mismatch at solid interfaces
1.3.	Bioinspiration in the development of functional interfaces
1.4.	Functional Gradients in Biomaterials34
1.5.	Interfaces in <i>Mytilus edulis</i> mussel byssus
1.5.1.	Distal-Proximal Thread Interface
1.5.2.	From the threads to the byssus stem
1.6.	Dynamic living / non-living interface
2.	Chapter 2: A strong quick-release biointerface in mussels mediated by serotonergic
cilia-b	ased adhesion58
2 1	Abstract 59

2.2.	Introduction	59
2.3.	Results and Discussion	62
2.4.	Acknowledgements	75
2.5.	References and Notes	76
2.6.	Supplementary Material	80
3.	Chapter 3: A dynamic bio-interface in mussels mediated by a me	chanoresponsive
interr	mediate filament-based biopolymer	100
3.1.	Abstract	101
3.2.	Introduction	102
3.3.	Results	106
3.4.	Discussion	118
3.5.	Conclusion	121
3.6.	Materials and Methods	122
3.7.	Acknowledgements	132
3.8.	References	133
3.9.	Supplementary material	139
4.	Chapter 4: Fabrication of Tunable Mechanical Gradients by Muss	els via Bottom-Up
Self-A	Assembly of Collagenous Precursors	142
4.1.	Abstract	143
4.2.	Introduction	144
4.3.	Results	148
4.4.	Discussion	162

4.5.	Conclusion	. 167
4.6.	Methods	. 168
4.7.	Acknowledgements	. 173
4.8.	References	. 173
4.9.	Supplementary Materials	. 180
5.	Comprehensive Discussion	. 187
6.	Final Conclusions and Summary	. 201
7.	Main References	. 204

Abstract

Design of advanced medical implants, such as brain-computer interfaces, tissue scaffolds, and artificial muscles must consider mechanical compatibility of the implant with soft tissues and the eventual release of the implant after its useful lifetime. Indeed, interfacial stresses generated at the junction between the soft tissue and hard devices having unlike properties are a major cause of failure. Yet, nature has evolved effective solutions to overcome mechanical mismatch through functionally graded interfaces. For instance, the mussel provides an ideal model to design gradients. It fabricates an abiotic protein-based fiber, known as byssus, to anchor in marine habitats by connecting the soft living tissue of the mussel to rocky surfaces. Mechanical mismatch exists between the stiff distal and softer proximal region of the thread, between the proximal region of the thread and the stem (onto which multiple threads are connected), and between the stem and the soft living tissue of the mussel. Given the inherent challenges of connecting mechanically mismatched materials, understanding the underlying structure-function relationships and formation of these interfaces is crucial. Currently, little is known about the biochemical and structural design of these junctions or how they are formed. Moreover, the mussel also offers a remarkable example of a strong, yet quick-release bio-interface between living tissue and a non-living biopolymeric material — an attribute that is rarely observed in natural systems.

Here, I focus my investigation on understanding the composition, structure, function, and formation of gradients in the stem-tissue and distal-proximal interfaces. To achieve this, I applied a cross-disciplinary experimental approach to elucidate how these complex gradients are formed

and function. In Chapter 2, I explored the neurally-controlled quick release of the byssus stem based on cilia movement. The stem divides into numerous biphasic wavy sheets that interdigitate with the living tissue. Sheets are composed of both a collagenous component resembling the properties found in mussel threads and a non-collagenous component in direct contact with the living tissue, particularly the cilia. In Chapter 3, I report the characterization of the outer lamellae component at the living non-living interface given its potential importance in mediating stem release. Here, Raman spectroscopy, fiber X-ray diffraction, and immunofluorescence was employed to determine the identity and structural changes of the unknown protein under applied forces, revealing a novel coiled coil protein, possibly implicated as a mechanobiological sensor. Finally, in Chapter 4, I explore the functionally graded design at the distal/proximal interface of byssal threads. I utilized mechanical testing coupled with video-extensometery, confocal Raman spectroscopy, advanced electron microscopy, and histological staining to delineate the composition, structure, function, and formation of the thread gradient. Overall, I discovered that mussels exhibit remarkable control over the formation and function of the graded interfaces in the byssus through meticulous control of biochemical components and their structural organization at multiple length scales. Extracted principles from these studies have relevance for novel design of functionally graded materials, advanced bio-implants, and for engineering quick release interfaces in soft robotics.

Résumé

La conception d'implants médicaux de pointe, tels que les interfaces cerveau-ordinateur, les tissus synthétiques, ou les muscles artificiels, doit tenir compte des compatibilités mécaniques

de l'implant avec les tissus mous qui l'entourent et son retrait éventuel après utilisation. En effet, les contraintes interfaciales générées à la jonction entre les matériaux vivants et non vivants, aux propriétés différentes, constituent une cause majeure de défaillance. Pour autant, la nature a su développer des solutions pour surmonter de potentielles incompatibilités mécaniques grâce à des interfaces graduellement fonctionnelles. La moule constitut un modèle idéal pour concevoir de tels propriétés graduelles. En effet, pour s'ancrer dans différents habitats marins, la moule fabrique une fibre à base de protéines abiotiques nommée byssus capable de connecter les tissus mous de la moule aux surfaces rocheuses. Une incompatibilité mécanique existe dans cette fibre ; d'abord entre la région distale rigide et la région proximale plus molle; puis entre la région proximale du byssus et le pédoncule (sur laquelle plusieurs fibres sont connectées); et enfin entre le pédoncule et le tissu vivant mou de la moule. Considérant les défis pour connecter ces matériaux mécaniquement incompatibles, il est donc essentiel de comprendre les relations structure-fonction sous-jacentes et la formation de ces interfaces. Cependant, la moule constitue également un exemple remarquable d'interface biologique robuste et à libération rapide entre le tissue vivant de la moule et des biopolymères non-vivants, chose rarement observée dans la Nature.

Ici, je concentre mes recherches sur la compréhension de la composition, la structure, la fonction et la formation des gradients interfaciaux des régions distale-proximale et colonne-tissu. Pour cela, j'ai appliqué une approche expérimentale interdisciplinaire pour élucider la formation et le fonctionnement de ces gradients complexes. Dans le chapitre 2, j'explore le contrôle neural et la libération rapide de la colonne du byssus basée sur des mouvement ciliaires. La colonne se divise

en de nombreuses plaques biphasiques ondulées qui s'entrecroisent avec le tissu vivant. Chacune de ces plaques comprend des composés non collagéniques en contact direct avec le tissue vivant, particulièrement les cils. Dans le chapitre 3, je propose une caractérise complète de la lamelle externe et de ses composants; à l'interface entre matériel vivant et non-vivant expliquant leur importance potentielle dans la médiation de la libération de la colonne. Ici, la spectroscopie Raman, la diffraction des rayons X sur fibre, et l'immunofluorescence furent utilisées pour identifier différentes protéines encore inconnues et déterminer leurs transitions structurales à la suite de différentes contraintes mécaniques, révélant une nouvelle protéine en superhélice (coiled coil), possiblement employée comme bio mécano senseur. Enfin, dans le chapitre 4, j'explore la conception de gradient fonctionnels aux interfaces des fibres de byssus. Pour ce faire j'ai eu recours à des tests mécaniques couplés à des expériences de vidéo-extensomètrie, de spectroscopie Raman confocale, de microscopie électronique de pointe, et différentes coloration histologiques pour définir la composition, la structure, la fonction, et la formation des gradients au sien des fibres. En conclusion, j'ai découvert que les moules présentent un contrôle remarquable en ce qui concerne la formation et la fonctionnalisation d'interfaces dans le byssus grâce à une régulation fine des composants biochimiques, organisationnels, et structuraux à plusieurs échelles. Les principes extraits de ces études sont pertinents pour la conception de nouveaux matériaux graduellement fonctionnels, des bio-implants de pointe et pour l'ingénierie d'interfaces à libération rapide en robotique molle.

Acknowledgements

First, I would like to express my gratitude to McGill University for providing me with the opportunity to pursue my studies and for fostering a stimulating academic environment. I am also grateful to the Natural Sciences and Engineering Research Council of Canada (NSERC), and the Fonds de Recherche du Québec (FRQ) for their generous financial support. I would like to extend my appreciation to the administration of the Department of Chemistry at McGill University for their constant guidance, and for keeping me informed of all necessary requirements throughout my degree program. Moreover, thanks to Professor Adam Hendricks and his research group for their valuable insights and knowledge in conducting experiments and interpreting results, as well as to Professor Van de Ven's group for their assistance with equipment usage.

I would also like to acknowledge Dr. Hatem Titi in the MC² team of Chemistry Department for his continuous help with SAXS/WAXS measurements, and the FEMR team at Strathcona for granting me access to their facilities. Their expertise and collaboration have been instrumental in the success of this research.

I am grateful to my committee members, Professors Anthony Mittermaier, Audrey Moores, and Hanadi Sleiman (replacing Prof. Moores), for their constructive feedback and guidance throughout my doctoral journey.

A special thanks to my fellow group members for fostering a collaborative and supportive atmosphere in the lab. I would like to particularly acknowledge Tobias and Max, former PhD students, whose guidance and assistance in the early stages of my PhD—especially in working with mussels and training on instruments—were critical to my progress. I would also like to thank Jenaes for being an excellent collaborator and colleague. Further gratitude goes to Dr. Jehle and Dr. Prowse for their unwavering support in troubleshooting and providing guidance on sample preparation, which was crucial to the success of my experiments. I would also like to thank Austin Richard and Alexandre Poulhazan for helping translate the English abstract.

Finally, I would like to express my appreciation to my supervisor, Professor Matthew Harrington, for being an exceptional mentor. Your endless support, guidance, and commitment to my academic growth have been influential to my success. Thank you for always being there to teach, advise, and create opportunities for my development.

Contribution to Original Knowledge

Chapter 1 provides a comprehensive literature review, highlighting the motivations behind the bioinspired approaches in designing functional interfaces. Chapter 2 through 4 presents the research findings discussed in the body of the thesis. The material includes findings from two published manuscripts on which I am a co-first author and one manuscript currently under preparation, which will be ready for submission in early 2025.

During my research, the original multidisciplinary approach taken was a driving factor in understanding the exceptional mechanics of the byssus at multiple scales. To function efficiently, the byssus mitigates mechanical mismatch between the soft mussel tissue and the stiff rocky surface. Indeed, the byssus is a complex composite of different structures, each with a specific functional purpose. While each structure has been well characterized, the interfaces linking them—critical for the overcoming mechanical stress and multifunctionality of the byssus—have not been thoroughly studied. Here, I focused on soft-hard and living-nonliving interfaces providing a number of original insights and knowledge on the underlying structure-function relationships and fabrication of both the living/non-living interface between the byssus stem root and generator, as well as between the stiff distal and softer proximal region of the thread.

While previous research has focused on the self-assembly of the byssus components, my work builds on this by examining how such processes can be tuned at the interfaces. Specifically, I investigated how mussels adapt the fabrication of the interfaces in response to environmental factors and explored the underlying mechanisms driving these adaptive changes. This was accomplished by examining the subtle structural and compositional features of the byssus at the distal-proximal transition using various techniques and correlating these features with functional responses. In addition, optimizing sample preparation for accurate measurements was crucial, including refining sectioning methods and understanding the conditions necessary for obtaining high-resolution Raman microspectroscopic compositional images. I also experimented with modifying histological techniques to enhance imaging for advanced microscopy. Furthermore,

this research addresses the challenge of capturing these dynamic responses within the hidden biointerfaces of the mussel's generator, which have been overlooked.

Contribution of Authors

The work reported in this thesis involved collaboration with other researchers as the cross-disciplinary techniques necessitated specialized knowledge and skills. I acknowledge the support and contributions from colleagues and collaborating labs, whose expertise complemented my own and significantly enhanced the quality and depth of the research, as will be mentioned below.

Chapter 1. The figures used to give a comprehensive background on literature do not constitute original work. Relevant credits and permissions are specified in the figure captions.

Chapter 2. I am co-first author of the published manuscript described in this chapter and played a lead role writing the manuscript under my supervisor's guidance. I performed histological analysis and confocal Raman spectroscopic imaging of tissues, performed investigations of neurotransmitter-dependent cilia response, and developed a method for and performed measurements of neurotransmitter-dependent interface mechanics. The other co-first author Jenaes Sivasundarampillai performed initial histological and Raman analysis, and generated 3D reconstruction of electron microscopy and μ CT data. Dr. Paul Zaslansky and Dr. Franziska Jehle assisted with acquiring μ CT and FIB-SEM data, respectively. Dr. Deniz Eren helped acquire STEM images and Dr. Tobias Priemel assisted in video tracking analysis of ciliary beating.

Chapter 3. I acquired the majority of the data appearing in this chapter, which represents a manuscript in preparation that I have played the lead role in writing under my supervisor's guidance. I performed protein extraction studies, histological analysis, immunohistochemical staining and imaging, confocal Raman spectroscopic mapping, ATR-FTIR spectroscopic measurements, WAXD measurements and analysis, and 3D FIB-SEM data reconstruction. The sequence of the MSP-1 protein characterized in this section was initially identified by Jenaes Sivasundarampillai during his MSc thesis work. However, the presence of this protein was still putative at that point and had not been definitively identified as a legitimate protein in the tissue. Dr. Franziska Jehle and Dr. Deniz Eren provided assistance in acquiring FIB-SEM and STEM datasets. Supporting figures S8 and S9, along with figure 19, were created by Prof. Jackson. Dr. Emily Prowse assisted in initial measurements and immunostaining imaging, while Prof. Adam Hendricks provided guidance on the analysis of immunostaining data. However, I further troubleshot these experiments and acquiring the final images used in the chapter.

Chapter 4. I am co-first author of the published manuscript described in this chapter and played a lead role in writing the manuscript under my supervisor's guidance. I performed extensive video extensometry-based mechanical measurements of the functional gradient in mussel byssal threads and developed an analysis approach for identifying the spatial profile of the gradient. I harnessed confocal Raman spectroscopic imaging to visualize the corresponding compositional gradient in byssal threads and to identify protein precursors in the mussel foot tissues. The other co-first author Dr. Max Renner-Rao purified and identified the core vesicle subpopulations using SDS-PAGE, MALDI-TOF, and Raman spectroscopy, and assembled core vesicles into fibers. To

obtain information on the structure of the distal-proximal transition at a high-resolution, Dr. Franziska Jehle and Dr. Deniz Eren helped acquire the STEM images.

List of Figures

Main Figures

Figure 1.1.Rearrangement of units at interfaces.	22
Figure 1.2 Mechanical behavior of two materials having different stiffness (Ei)	25
Figure 1.3. Interfaces in advanced biomedical devices.	27
Figure 1.4. Engineered living materials encompasses the Design–Build–Test–Learn (D	BTL)
approach	30
Figure 1.5.Interfaces in biological materials.	33
Figure 1.6. Types of gradients in nature	34
Figure 1.7. Chemical and structural gradients in biological systems.	39
Figure 1.8. The Mytilus edulis mussel produces several byssal threads	42
Figure 1.9. Mytilus edulis byssus hierarchical structure and composition	44
Figure 1.10.Mechanical testing on byssus.	46
Figure 1.11. SEM images and illustration of the hierarchical structure of the stem and gener	rator
	50
Figure 1.12.Schematics representing the storage of precursors in foot and the self assemb	ly of
byssal thread	54
Figure 1.13.TEM images of the cervical crevice region	55
Figure 1.14.Microscopy images of the granules stored in the generator septa	56
Figure 2.1 Mussel byssus stem root microscale hierarchical structure	61
Figure 2.2. Structural and compositional analysis of the stem generator biointerface	66
Figure 2.3. Histological and spectroscopic characterization of stem release	67

Figure 2.4.Role of cilia and neurotransmitters in stem release
Figure 3.1. Overview of mussel byssus stem root biointerface
Figure 3.2. Extraction, sequence and localization of mussel stem protein-1 (MSP-1) 108
Figure 3.3. Electron microscopic characterization of stem root biointerface
Figure 3.4. Conformational characterization of mussel byssus stem root outer lamellar layer (OLL)
Figure 3.5.Mechanically induced alpha to beta conformational transition in the stem root OLL
Figure 4.1.Hierarchical structure of the mussel byssus
Figure 4.2. Real-time mechanical response of different segments in a byssal thread 149
Figure 4.3. Variation in lengths of the proximal, transition and distal region and whole thread
mechanics
Figure 4.4. Ultrastructural analysis of byssal thread gradient structure
Figure 4.5. Confocal Raman spectroscopic mapping of the transition region of byssal threads 156
Figure 4.6.Biochemical characterization and assembly of precursor vesicles
Figure 4.7. Model of byssal thread gradient formation and function
Supporting Figures
Figure S 2-1. Anatomy of a jettisoned byssus
Figure S 2-2. Mechanical testing setup for forced byssus pullout studies
Figure S 2-3. Mechanical testing plots of forced stem release under different conditions 93
Figure S 2-4.Mechanically induced byssus release 94
Figure S 2-5.FIB-SEM reconstruction of the generator-stem biointerface

Figure S 2-6.Comparative Raman spectra from stem and generator compared to the proxima
byssal thread and tendon 90
Figure S 2-7 .Tracking cilia movements 9
Figure S 2-8. Generator cilia beating speed as a function of consecutive treatment with serotonia
and metergoline9
Figure S 3-1Sequences with similarity to M. edulis mussel stem protein 1 (MSP-1) 139
Figure S3-2Genomic locations, exon/intron structures and sequence14
Figure S 4.7-1.Image tracking tool to determine the strain of individual segments comprising
thread as a function of time and applied force
Figure S 4.7-2.Real-time mechanical response of different segments from four threads acquired
from a single mussel
Figure S 4.7-3. Additional real-time mechanical response plots of different threads acquired fron
another mussel
Figure S 4.7-4. Confocal Raman spectroscopy of byssal threads
Figure S 4.7-5.Purification using only distal tissue

List of Abbreviations

3Y-TZP - Zirconia polycrystals doped with yttria

ATR-FTIR - Attenuated total reflectance Fourier transform infrared spectroscopy

BMI - Brain-machine interface

CC - Coiled coil

cDNA - Complementary deoxyribonucleic acid

CCDC39 - Coiled-coil domain-containing protein 39

DA - Dopamine

DIC - Differential interference contrast

DOPA - 3,4-dihydroxyphenylalanine

ECM - Extracellular matrix

ELMs - Engineered living materials

FIB-SEM - Focused ion beam scanning electron microscopy

Gly - Glycine

His - Histidine

HRDs - Histidine-rich domains

ILL - Inner lamellar layer

kDa - Kilodalton

LC - Liquid crystal

MET - Metergoline

Mfp - Mussel foot protein

Micro-CT - Micro computed tomography

MPa - Megapascal ((Newton/meter²) \times 10⁶)

MSP - Mussel stem protein

OLL - Outer lamellar layer

PAGE - Polyacrylamide gel electrophoresis

PCE-μCT - Phase contrast-enhanced micro-computed tomography

preCol - Prepepsinized collagen

Phe - Phenylalanine

PLM - Polarized light microscopy

PTMP - Proximal thread matrix protein

RACE - Rapid amplification of cDNA ends

SDS - Sodium dodecyl sulfate

SIM - Structured illumination microscopy

STEM - Scanning transmission electron microscopy

TMP - Thread matrix protein

WAXD - Wide-angle X-ray diffraction

von Willebrand factor type A (vWA) - von Willebrand factor type A

PEEK - Polyether-ether-ketone

PLA - Polylactic acid

NCX - Sodium-calcium exchanger

RTT - Rat tail tendon

Chapter 1

Introduction

Interfaces are fundamental to material design in a vast array of applications such as glues, coatings, and bioimplants, as they dictate how materials interact with each other and the surroundings¹⁻⁴. Among the various types of interfaces—such as liquid-solid, gas-liquid, gas-solid, and liquid-liquid—the solid-solid interface stands out as particularly critical⁵. For instance, the interface between adhesives and substrates plays a crucial role in determining the strength and durability of the resulting bonds, similarly, in the biomedical context, such interfaces are key for ensuring the compatibility and longevity of implants within the human body^{1, 2, 4, 5}. Despite its significance, creating effective solid-solid interfaces still poses substantial challenges for engineers³. Adhesives, for instance, often fail in wet environments, and abrasion-resistant coatings for flexible substrates struggle to achieve a balance between hardness and extensibility ^{6, 7}. Additionally, bioimplants frequently encounter failures due to mismatches in mechanical properties with surrounding tissues, and when removal becomes necessary, complications can arise, leading to tissue damage and potential inflammation⁸. Yet, nature offers solutions to these challenges⁹. In this work, I will explore how mussels achieve strong yet reversible attachment to surfaces in turbulent conditions using the byssus – an array of tough, protein-based adhesive fibers that establish a robust mechanically graded interface between the soft tissue of the mussel and hard rocky seashore surfaces. These insights are particularly significant for developing advanced biomedical devices and implants, such as brain-machine interfaces. Nevertheless, the mechanisms that enable such functional performances of the are not yet fully elucidated.

To provide relevant background and context to this work, I will first consider the formation of interfaces and the key properties that make them functionally important. Specifically, I will focus on the challenges to creating interfaces between materials having dissimilar mechanical properties, such as between soft living tissues and the stiff devices. Afterwards, I will highlight literature on solutions that bioengineers have implemented to overcome these challenges, while emphasizing the more effective strategies that nature has evolved to address those issues. In the following chapters, I will employ a multidisciplinary approach to understand how various interfaces in the mussel byssus are fabricated and will investigate the structure-function relationships that define the remarkable performance of these interfaces. In chapter 2, I will focus on the quick-release biointerface at the boundary between the non-living byssus and living mussel tissue. In particular, I will explore the role of interactions between the lamellae and cilia in stem root release and investigate neurochemical factors that may trigger the activity of cilia. I will further focus on the structural description of the cilia and biphasic lamellae of the byssus stem root and analyze the mechanical strength at their interface. Subsequently, in chapter 3, I will delve deeper into characterizing the composition and function of the non-living component of the stem root interface, i.e., the lamellae. In particular, I will investigate the protein composition and explore the distinctive mechanoresponsive behavior of the lamella. Finally, beyond the living/non-living interface, in chapter 4, I will investigate the soft-hard interface present at the transition between the distal-proximal region of the mussel byssal thread core. This section focuses on characterizing the composition, structure, and mechanics of the functionally graded interface, which collectively contributes, along with other interfaces, to

mitigating the mechanical mismatch between the mussel's soft living tissue and the stiff adhesive plaque.

1. Comprehensive Literature Review

1.1. Interactions at Interfaces

Interfaces in materials arise at regions where two distinct phases meet—one phase may be liquid or solid, while the other can be solid, liquid, or gas ³. At these boundaries between different phases, atoms or molecules can have different properties from those of the individual bulk phases. For instance, surface atoms and molecules often possess significantly different energies and reactivities compared to those in the bulk of materials in which atoms and molecules experience a more uniform force field due to interaction with neighboring molecules³. In solids, atoms have limited mobility compared to liquids or gases, meaning they do not easily move from the bulk material to the surface (Fig. 1.1)³. As a result, adjustments to atomic positions occur mainly through changes in the spacing between surface atoms, rather than significant movement of atoms from the interior³. These changes become more pronounced when a different material meets the solid surface, or when external forces such as pressure or mechanical stress are applied³. This leads to new surface energy configurations, which refer to the excess energy at the surface of a material compared to its interior³.

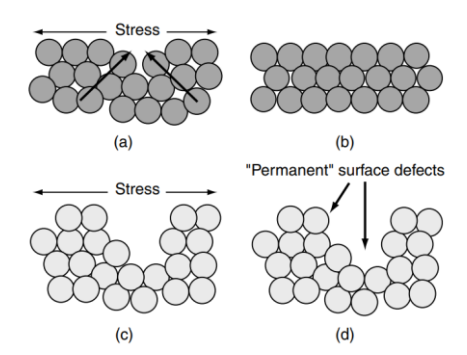


Figure 1.1.Rearrangement of units at interfaces. a) a liquid surface under stress with "vacancies"; b) molecules beneath the surface quickly move toward the stressed regions to restore balance; c) a solid surface under stress exhibiting multiple defects; d) molecules will not easily flow into the stressed areas, because of limited mobility, leaving the defects intact and resulting in a higher surface energy³. Copyright © 1999, John Wiley and Sons ³.

Scientists are particularly interested in understanding such interactions at interfaces for adhesion purposes. For example, in the biomedical field, there is an increasing demand for adhesives and sealants that function in wet environments for a vast range of operations and treatments which require synthetic and/or natural macromolecules to adhere to biological tissues for a prolonged time in the body⁷. This can include sealants that prevent the leakage of biological fluids, including lymph, cerebrospinal fluid, and gastrointestinal juices⁷. Additionally, fetal surgery is a growing field of medicine which can improve and save lives of children with debilitating or terminal diagnoses¹⁰. Yet, this carries a risk of premature birth because sutures cannot be used to close incisions in the amniotic sac¹⁰. Effective surgical adhesives could solve this crucial challenge ¹⁰. Understanding the unique properties of interfaces is crucial for the design of such advanced adhesives.

Another class of materials that can enhance the performance of interfaces in solids is coatings ¹¹.For example, coatings comprised of hard alloys based on Ni, Co, and Fe can serve as a protection against abrasive wear and fatigue failure in tools for the mining, oil, and gas industrieswhere components interact, slide, and rotate against each other 12. For that purpose, researchers have put efforts to enhance the mechanical properties and hardness of wear-resistant coatings by incorporating nanoparticles such as SiO₂, TiO₂, alumina (Al₂O₃), and zirconium dioxide (ZrO₂) ¹³. Nonetheless, adequate bonding to the substrate remains an important prerequisite for the long-term function and particularly crucial in composite coatings on the relatively compliant substrates¹⁴. Similarly, with the expanding interest on integrating bioimplants, such as dental implants, joint prosthesis, and spinal fixations, with tissues to restore the natural function of specific body parts, researchers have been exploring how to prepare anti-wear coatings even on implantable devices for better adhesion with the soft tissue, and higher toughness and hardness as well as lower coefficient of friction¹⁴. One approach is the application of hard-soft coatings, like TiN/Ti multilayer coatings along with additional surface treatments or surface coatings ^{14, 15}. However, another key factor in ensuring the effectiveness of these coatings for the various applications lies in preventing internal stresses that could lead to interfacial debonding¹⁴.

1.2. Mechanical mismatch at solid interfaces

To have a deeper understanding of the origins of the stresses generated at interfaces between materials with unlike properties, we will examine what happens when two different adjoined structural materials A and B, having different stiffness values, E_A and E_B and/or different Poisson's ratios V_A and V_B , are loaded in tension (Fig. 1.2)¹⁶. Stiffness determines the amount of deformation

(strain) a material will experience under a given applied stress. Poisson ratio quantifies the extent of lateral deformation in a material when subjected to uniaxial loading 16 . For example, a value of 0.3 for a cylinder under load implies that the diameter reduces by 30% for every 100% increase in length 16 . In this example, we can imagine two cylinders of materials A and B with identical cross-section and length, joined at a common interface 16 . Applying a tensional stress on the joined cylinders results in a longitudinal strain on each material determined by their individual stiffness values E_A and E_B and a radial strain determined by the resulting longitudinal strains and the respective Poisson's ratio 16 . If the radial strains are not equal in the two cylinders at a given applied stress, then an interfacial stress will develop at the interface 16 . Essentially, the different degrees of radial deformation in the two materials will give rise to interfacial stresses at the contact zone that act normal to the applied stress, σ_z (Fig. 1.2) 16 . These stresses are composed of two elements, σ_r and σ_θ , interfacial radial and circumferential stress, respectively, and can be determined using equation 1^{16} .

$$\sigma_{\theta} = \sigma_{r} = [v_{B} - v_{A}E_{B}/E_{A}][\sigma_{z}/(1 - v_{B})]$$
 (1) ¹⁶

According to this equation, interfaces between materials with identical stiffness and Poisson ratios (i.e., same material) result in a radial interfacial strain σ_r value of 0, as would be expected ¹⁶. However, when either the stiffness or Poisson ratios of the two materials are different, the magnitude of the radial interfacial strain will increase ¹⁶. If it gets large enough, this could result in structural failure that often takes the form of delamination in the contact zone ¹⁶.

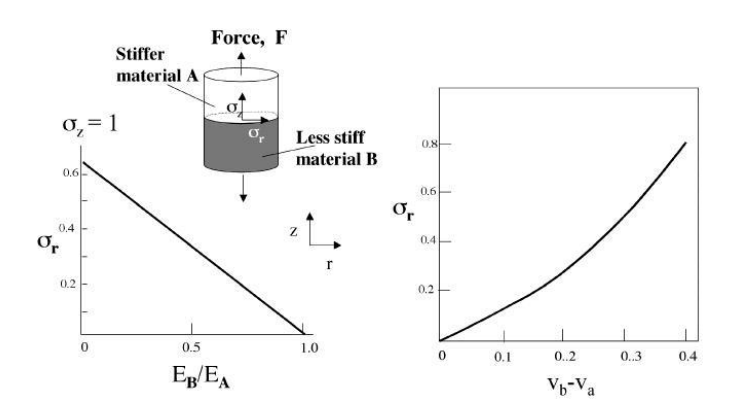


Figure 1.2 Mechanical behavior of two materials having different stiffness (Ei). First graph: radial stress, σ_r , in a butt joint increases as the stiffness of B decreases relative to A, while fixing the Poisson ratio of both at 0.4. Second graph: σ_r increases as the difference between Poisson ratios of vA and vB increases at a constant stiffness ratio of 1. Reprinted (adapted) with permission from 16 H. C., Stucky, G. D., & Hansma, P. (2004). Exploring molecular and mechanical gradients in structural bioscaffolds. Biochemistry, 43(24), 7653-7662. https://doi.org/10.1021/bi049380h. Copyright 2025. American Chemical Society. 16

Interfacial failure becomes particularly problematic at soft-hard interfaces. For example, when soft tissues having stiffness values ranging from 0.1 to 100 kPa interact with biomedical devices possessing stiffness values around 1-100 GPa ^{17, 18}. Consider a dental implant, which is usually composed of pure titanium (Ti) and its alloys having a stiffness of approximately 110 GPa and is inserted into the soft mucosal tissue and the bone to restore missing teeth. Mechanical stresses originating from activities such as chewing and parafunctions (like grinding and clenching) lead to strain in the tissue and in the implant ^{18, 19}. As a result, the entire structure moves and deforms due of the stiffness mismatch of the implant and tissue, leading to damage at the interface ¹⁸. As a solution, some studies have proposed the use of materials with lower stiffness, such as porous

Ti or fiber reinforced polyether-ether-ketone (PEEK) composites 18, 20, whereas others focused on designing implants with geometries such as tapered or conical shapes that mimic the natural tooth structure to distribute stresses more evenly (Fig.1.3A)²¹. Apart from dental implants, metallic skeletal hardware has been also used for surgery applications, such as bone fixation or bone replacement. Nevertheless, stress shielding (the reduction in bone density) and stress concentration are amongst the most common causes of failure of the device 20. At the interface, bones have an anisotropic structure, resulting in mechanical properties dependent on the direction in which they are measured 20 . An example of this can be a femoral cortical bone, whose elastic modulus measured along the longitudinal direction is often approximately 18 GPa, while along the transverse direction, it varies between 5 and 10 GPa ¹⁸. On the other hand, the elastic moduli of the metals employed for skeletal repair or replacement devices, such as titanium alloys, cobalt-chromium alloys, and stainless steel are approximately 200 GPa and basically isotropic (direction independent), which makes them ~10 times stiffer than the bone to which they are anchored ²⁰. As a result, delamination at the interface in the form of plate or rod cracking or screw pull-out may occur ²⁰. Several suggestions have been proposed by engineers to reduce such effects, such as the application of materials with modulus close to that of the bone, adaptation of geometry with predetermine mechanical properties, and surface modification that ensures proper integration load transfer to the bone²⁰.

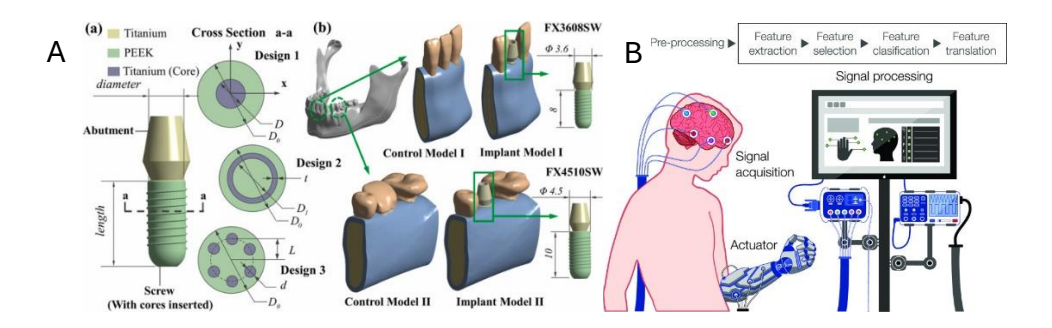


Figure 1.3. Interfaces in advanced biomedical devices. (A) Three designs of metal-polymer structures for dental implants and three-dimensional geometric model of mandible (B) A schematic depicting the main stages involved in EEG-based brain—computer interface operation (A) Reprinted from Composites Communications, Vol. 24, Liu, C., Lin, J., Tang, L., Liu, Z., Jiang, Z., Lian, K., "Design of metal-polymer structure for dental implants with stiffness adaptable to alveolar bone", pp. 100660, Copyright (2021), with permission from Elsevier ²⁰. (B) Copyright © 2021, Portillo-Lara, Roberto; Tahirbegi, Bogachan. This article is distributed under a Creative Commons Attribution (CC BY) license²².

Considering the recent advances of companies such as Neuralink, it is important to mention that brain-machine interfaces (BMI) presents a particularly challenging example for engineering hard-soft interfaces(Fig. 1.3B) ²². BMI are bioelectronic devices designed to stimulate groups of neurons or nerve fascicles while recording electrical signals in a targeted area²³. One of the primary purposes is to restore physiological neural activity and re-establish sensory-motor feedback using prosthetic devices ^{22, 23}. Yet, the mechanical and biological mismatches, along with weak physical adhesion that leads to shifts between rigid electronic devices and soft brain tissue often provoke local tissue damage and host immune response²³. This can impair signal recording and shorten the lifespan of BMIs in clinical settings²³.

Recently, researchers have developed low-modulus plastics and elastomers that enhance physical compliance and flexibility for neural probes, aiming to reduce negative interactions between the implanted device and surrounding tissue 24. Nonetheless, these enhanced properties still do not completely mimic those of soft brain tissue and might lead to inaccurate signals and chronic foreign body response during long-term BMI implantation ²⁴. Given such limitations, there is an increasing interest in investigating alternative electrode materials and designs that provide better mechanical flexibility and enhanced biocompatibility 24. Liquid metalbased electrodes are a promising option, which are made from Galinstan, a eutectic alloy of gallium, indium, and tin ²⁵. It stays in a liquid form at room temperature while forming a stable oxide layer on its surface that helps protect the underlying alloy from further oxidation²⁵. They have low toxicity, excellent electrical conductivity, and demonstrate remarkable mechanical flexibility²⁵. To fabricate the liquid metal-based electrodes, specialized techniques such as photolithography, thin-film deposition and direct writing and printing methods must be employed to enable the precise patterning and deposition of liquid metal alloys onto substrates ²⁵. Nonetheless, liquid-metal electrodes must be further developed since their flexible mechanical properties can lead to issues with long-term stability and durability under physiological conditions ²⁵.

While the various solutions mentioned have made initial progress in overcoming the inherent mechanical mismatch at the bioimplant and tissue interface, they do come with notable pitfalls. The manufacturing process often necessitates extensive preparation, which can increase both time and costs²⁶. Additionally, detailed simulations, such as finite element analysis (FEA), can be

computationally intensive, complicating the prediction of how designed geometries will function at implant boundaries²⁷. Yet, some of these very problems have already been solved in biological systems through evolution. In the next section we discuss some of the strategies used in nature, and how these might be applied to improve interface design in synthetic systems.

1.3. Bioinspiration in the development of functional interfaces

The field of bio-inspired materials suggests that humans can learn from nature how to make improved materials by studying structure-function relationships that define biological materials²⁸. Indeed, nature has already solved similar materials design challenges through evolution, which may offer innovative solutions to building functional interfaces²⁸. Amongst the countless species that inhabit Earth, each organism has evolved a structure, shape, and function that are adapted for survival under relevant environmental conditions ²⁹. Biological materials are typically structured in a hierarchical manner, with controlled structural organization ranging from the molecular level to nano, micro, and macroscale. As a result, their properties are adapted across many length scales, each contributing to their multifunctional capabilities ²⁹. By observing and understanding the multiscale design of these natural systems, scientists have gained inspiration for constructing synthetic systems²⁹. For instance, the 1891 flight of Otto Lilienthal, a German aviation pioneer, marks one of the earliest examples of biomimetics in aviation. Inspired by the way birds fly, Lilienthal designed gliders and wing-flapping aircraft that mimicked avian movement³⁰. More recently, researchers have examined nature with the goal of not only developing biomimetic materials but also replicating natural processes to create new materials and sustainable designs (Fig. 1.4) ^{29, 30}. This has led researchers to analyze bioinspired innovations

from various perspectives: how materials are formed in nature, how organisms perceive their environment (sensors), how they navigate their surroundings (biomechanics and kinetics), and how they behave and function ³¹. In this thesis, however, I will particularly focus on the first and the last aspects.

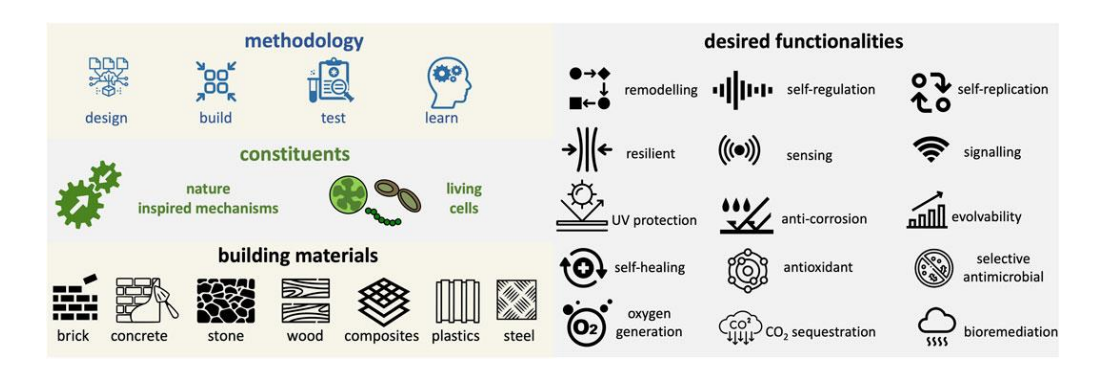


Figure 1.4. Engineered living materials encompasses the Design–Build–Test–Learn (DBTL) approach and benefits from the synergistic strength of living cells and bioinspired concepts for the development of living materials that are capable of interacting, adapting, and responding to environmental changes²⁹. Copyright © 2023, Sandak and Butina. This article is distributed under a Creative Commons Attribution (CC BY) license ²⁹.

To build materials, nature generally applies methods analogous to additive manufacturing such as 3D printing, as well as self-assembly processes reminiscent of 4D printing³². The fourth dimension represents 'time', meaning objects are designed to change shape or adapt over time in response to external stimuli such as heat, moisture, light, or pressure³². This allows for shaping the overall characteristics of materials at multiple length scales with various mechanical functions²⁸⁻³¹. Similarly, in biological systems, the fabrication of materials involves for instance cellular secretion of biomolecular precursors (e.g., proteins) that self-organize and cross-link

either within the living organism (e.g., tendon, muscle tissue) or outside the organism (e.g., spider silk, mussel byssus)³³. This self-assembly approach is employed in many living systems to produce, for example, a variety of biointerfaces which are not possible to achieve in human-designed materials using the current top-down processing approaches. However, mimicking the design of biological material interfaces has been of great interest in the field of engineering, and their properties have been classified into four categories, as illustrated in figure 1.5.a ²⁸:

a) Interfaces that enhance the fracture resistance of brittle materials. One prominent example of such an interfacial design exists in nacre²⁸, which is the name given to the iridescent layer on the inside of the shells of mollusks such as abalone and mussels. Nacre consists of calcium carbonate tablets that are approximately 500 nm thick and range from 5 to 15 µm in diameter, bonded by thin layers of soft proteins in a brick-and-mortar configuration ²⁸. Stresses concentrate at the soft-protein interfaces leading to localized failure; however, this "planned weakness" functions to hinder and deflect the crack propagation, increasing the overall toughness of the material ²⁸. In addition, there is a variety of other mechanisms at work at the interface which are thought to improve overall fracture resistance. The platelets feature uneven surfaces, allowing partial contact through mineral bridges and nano-asperities, which may facilitate stress transfer among them ²⁸. Inspired by such nacre interfacial design, researchers created dental materials through the freeze-casting of zirconia polycrystals doped with yttria (3Y-TZP) suspended in a solution, followed by densification with a methacrylate resin³⁴. This resulted in a composite featuring nacre-like lamellar and brick-and-mortar structures, which was subsequently tested to assess its fracture toughness³⁴. The mechanical plots showed stable crack propagation and enhanced

crack-growth resistance, compared to the instantaneous cracking observed in 3Y-TZP ceramics 34 . Additionally, the two composites had a fracture toughness values of approximately 1.2 and 1.7 kJ m $^{-2}$, which are around four and six times greater than those of 3Y-TZP ceramics 34 .

- b) Interfaces that facilitate deformation of materials. Interfaces in the sutures of a turtle shell have been shown to contribute to their flexibility. The complex bony sutures found in the ribs of the shell are highly convoluted and consists of interdigitating fingers of bone separated by a soft collagenous interface (Fig. 1.5b) ²⁸. The soft interface allows for minor bending deformations to enhance the shell's flexibility. With larger deformations, however, the fingers interlock, resulting in a significant increase in the stiffness of the interface ²⁸. In one study, designs inspired by sutures were fabricated using polylactic acid (PLA), a widely used thermoplastic in fused deposition modeling printing known for its biodegradability, and favorable strength and stiffness properties³⁵. Using three-point bending tests, the flexural behavior was analyzed and complemented by digital image correlation to gain deeper insights into the bending response of the suture structure³⁵.
- c) Interfaces that enable materials to function as actuators in response to external stimuli. Interfacial design in some biological material can lead to motion and the generation of forces, such as the movement of wheat awns in reaction to changes in humidity²⁸. The cross-section of an awn has two distinct types of tissue with varying cellulose arrangements²⁸. One type has cellulose fibrils are relatively randomly oriented, allowing for isotropic swelling, while the other type has cellulose fibrils aligned parallel to the awn, restricting swelling to an anisotropic

pattern²⁸. These structural differences enable the awns to perform a 'swimming movement', which pushes the seed along the ground. Ha et al , inspired by awn's mechanism, fabricated hygroresponsive actuators via the directional electrospinning process ³⁶. In brief, a strong electrical field is applied to a polymer solution drop hanging from a capillary needle which will be later deposited on a rotational collector and aligned into fibers of specific orientation ³⁶. This will result in two artificial bilayers, an active and inactive layer that exhibit the helical coiling just as the awns³⁶. The direct applications of the structure will enable a self-burrowing actuator, capable of propelling itself into soil similar to how Pelargonium seeds do in nature³⁶.

d) Interfaces that serve as joints between materials with significantly different properties ²⁸. As this is a major focus of this thesis, this topic will be examined in detail in the following sections.

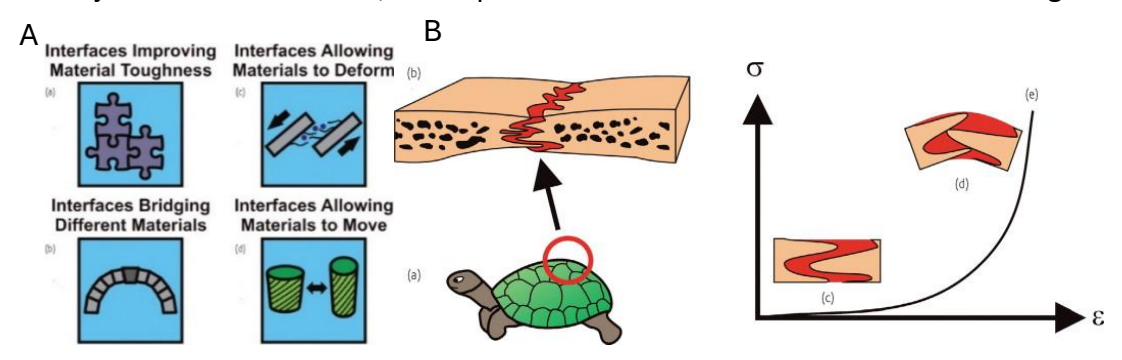


Figure 1.5.Interfaces in biological materials. The classes of various of biological tissues containing internal interfaces following the definitions given in the text. (B) The shell of the turtle is made up of ribs, with sutures formed by interdigitating protrusions of bone separated by a soft collagenous layer. Upon large deformations, the interdigitations of bone interlock resulting in a significant stiffening of the composite. (A-B) Reprinted from Materials Today, Vol. 14, Issue 3, Dunlop, J. W. C., Weinkamer, R., Fratzl, P., "Artful interfaces within biological materials", pp. 9, Copyright (2011), with permission from Elsevier²⁸.

1.4. Functional Gradients in Biomaterials

As described in *section 1.2*, there are significant challenges to joining two materials with very different stiffness and/or Poisson's ratio at a common interface. In many well-documented cases, nature has solved this problem by employing 'gradients' between joint materials³⁷. Gradients are characterized by the presence of site-specific properties within a material which may vary throughout the entire material volume, or within a restricted zone, such as near the interface between dissimilar materials, as illustrated in figure 1.6a and b, respectively ³⁷. For instance, in the latter case, the properties may change either gradually or in a discontinuous manner, as described by the stepwise mode (Fig. 1.6a)³⁷.

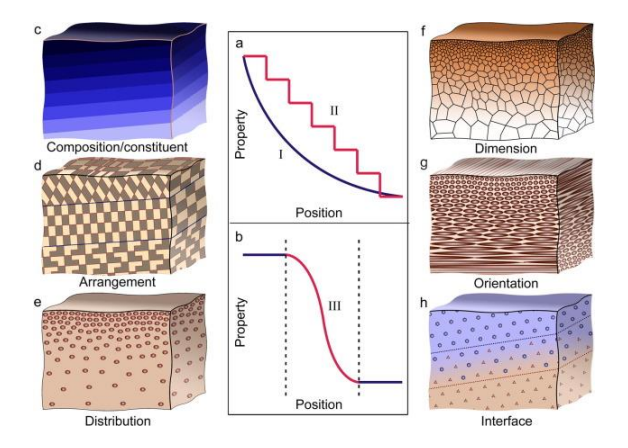


Figure 1.6. Types of gradients in nature. (a) (I)Gradual or (II) a stepwise manner change in local properties within the entire material volume; (b) continuous variation of local properties across the interface between dissimilar components; (c–g) the changes in chemical compositions/constituents which are commonly employed in biological materials are associated with (c) and structural characteristics, including the arrangement (d), distribution (e), dimensions (f), and orientations (g) of building units; (h) Gradient interface in biological materials. Reprinted from Progress in Materials Science, Vol. 88, Liu, Z., Meyers, M. A., Zhang, Z., Ritchie, R. O.,

"Functional gradients and heterogeneities in biological materials: Design principles, functions, and bioinspired applications", pp. 32, Copyright (2017), with permission from Elsevier ³⁷.

The gradation of properties arise from changes in two primary categories: 1) local chemical composition of the material and 2) local structural characteristics including arrangement, distribution, dimensions, and orientations of the structural building units³⁷. Most gradients in biological materials are associated with variations in local chemical composition, including the type and concentration of biominerals, inorganic ions, and biomolecules, along with hydration levels ³⁷. For instance, the biomineralization process, as seen chiton radular teeth, elasmoid fish scales, and crayfish mandibles, regulate the degree of mineralization by preferentially locating the hard and stiff bio-minerals at regions experiencing considerable mechanical stress and abrasion ³⁷. This becomes important for enhancing contact and wear resistance, where higher hardness and stiffness are required ³⁷. Besides the degree of mineralization, organisms are adept at adjusting the bonding states of their biopolymers, such as forming the metal coordinationbased cross-links between neighboring protein side chains, at the molecular level through the use of inorganic ions gradient³⁷. Spider fangs and worm jaws contain molecular coordination complexes between histidine amino acid residues in proteins and metal ions such as Zn and Cu, that are more concentrated in at locations near the tip and peripheral regions, yet scarce at the base and inside(Fig.1.7a) ³⁷. In these materials, the gradient of metal ions is controlled through a gradient of proteins enriched in histidine residues, which display a non-uniform spatial distribution of similar fashion ³⁷.

In other cases, however, the physical properties of biomaterials having essentially uniform chemical compositions are largely determined by how atoms and molecules are organized at the nano- or microscale — as markedly depicted for example by Hall—Petch relationship in physical metallurgy, which states that the yield strength correlates inversely with the square root of the grain size in crystalline materials ³⁷. In biological systems, structural diversity and hierarchy can get even more complex and be tuned using structural gradients that are mostly associated with four aspects of elementary characteristics, i.e., the arrangement, distribution, dimensions, and orientations of structural units ³⁷. For example, the shell of the bivalve *Saxidomus purpuratus* (Fig. 1.7b), exhibits a graded mechanical property resulting from the stacking aragonite units in a loosely packed porous form and the dense crossed-lamellar arrangement in the middle and inner layers, respectively ³⁷. The middle layer is weak and serves to dissipate energy and relieve stress concentrations, compared to the inner layer, which is strong and tough and serves to withstand damage owing to the effective crack deflection and twisting induced by the crossed-lamellar structure²⁷.

In addition to variation in arrangement, the dimensions of the constituents in biological materials can largely determine their function³⁷. This is commonly observed in materials with a laminated structure having tailored lamellar thickness, as seen in the twisted plywood layers of arthropods such as the *Homarus americanus* lobster, whose thickness increases from the exocuticle to endocuticle in the exoskeleton³⁷. Consequently, the tissue containing the exocuticle will be harder and stiffer than the endocuticle, similar to the Hall-Petch relationship, where finer structures result in increased hardness and stiffness³⁷. Additionally, in a wide range of impact-

resistant biological materials, such as in the defensive armors of pangolin and fish scales, and offensive weapons of the mantis shrimp appendage, graded orientations have been utilized³⁷. For instance, the keratin lamellae in the intermediate layer of pangolin scales are arranged nearly parallel to the surface at the interior, and get tilted by \sim 45° at the exterior in continuous manner (Fig.1.7c) ³⁷. Therefore, a synergistic combination of higher stiffness and strength will be manifested towards the surface with an increasing fracture resistance with depth due to the extrinsic toughening resulting from continuous crack deflection along the lamellar interface ³⁷. While the previously stated examples exhibit gradients throughout the volume of the same material, living organisms as well excel at creating transitions across interfaces between different components³⁷. Such gradients act to smooth out any abrupt changes in composition/structure or properties and are prominently founds in a variety of organs, such as in teeth and the tendon/ligament-to-bone interface ^{37, 38}. A tooth consists of two major parts, the outer enamel and the inner dentin, which perform distinctly different functions; the former is made from prisms of highly mineralized collagen fibers providing hardness and wear resistance to the tooth, while the latter is composed of less mineralized dentin tubules that is much tougher and is essential to preserve the integrity of tooth³⁵. Between these adjacent materials exist two interfaces known as the dentin-enamel junction (DEJ) and cementum-dentin junction (CDJ), which display graded properties to support the function of the tooth³⁵. In the DEJ, a gradual transition in the mineral concentration, collagen fibril orientation, and the size and morphology of hydroxyapatite crystals is present ³⁵. In the CDJ, on the other side, a gradient in chemical composition (hypo-mineralized collagen fibers and polyanionic molecules) and splitting of collagen fibers into individual fibrils that will further intermingle with the extracellular matrix of mantle dentin is observed ³⁵.

Similarly, the tendon-ligament to bone interface requires a seamless transition between soft and hard tissues, where the mechanical properties of tendons and ligaments—being more flexible and less stiff—gradually change into the stiffer, mineralized bone³⁹. Tendons attach muscles to bones, while ligaments link bones to other bones and the point of attachment is known as the enthesis³⁹. The enthesis is composed of continuous gradual transition of three different types of tissues: tendon/ligament, fibrocartilage, and bone³⁹. Tendons/ligament is mainly composed of collagen, including type I and III collagens, and decorin in small amounts³⁹. Fibrocartilage, being the meeting point of the soft tissue and hard bone, is the most critical region at the interface³⁹. It imparts flexibility to the interface due to its enrichment with proteoglycans such as aggrecan and decorin, and a combination of type II and type III collagen fibers³⁹. Additionally, fibrocartilage is organized into two distinct layers: mineralized and non-mineralized fibrocartilage³⁹. This layered structure further facilitates the attachment to bone by incorporating collagen type I, along with other proteins including mineralized components³⁹.

Akin to this design of functional gradients in living tissues, a principal strategy for synthetic biomaterials has been applied in tissue engineering³⁷. For instance, microporous scaffolds have been produced with similar gradients in pore size and porosity as in bones to allow both, a fast osteoconduction process for bone remodeling in the high-porose regions with larger pore size and a good mechanical rigidity in the denser regions³⁷. The gradient in porosity can be

additionally combined with a gradient in chemical compositions, particularly, mineralized collagen-glycosaminoglycan that would mimic the composition and structure of articular cartilage on one side and subchondral bone on the other³⁷. This will allow smooth load transfer and minimize stress concentration at interfaces, which ultimately lead to enhanced stability and strength³⁷.

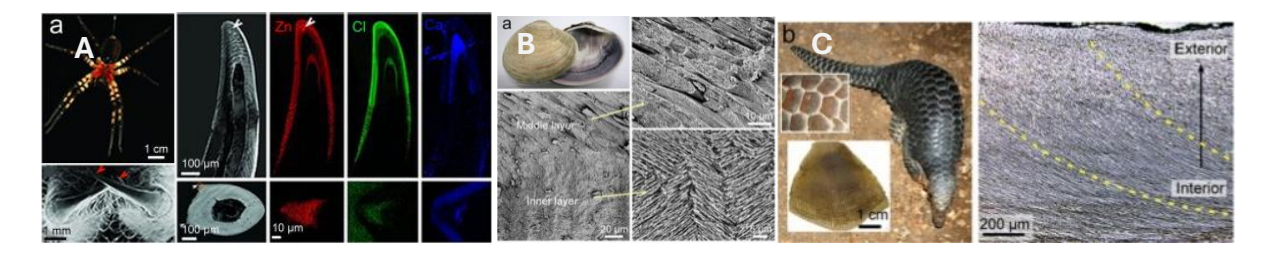


Figure 1.7. Chemical and structural gradients in biological systems. (A) In the spider fang and the jaws of bloodworm, inorganic ions participate in the formation of inter-molecular coordination complexes are more concentrated at the tip and peripheral regions, but scarce at the base and interior, respectively; (B) a bivalve Saxidomus purpuratus shell composed of aragonite elements that stack in a loosely packed porous form and a dense crossed-lamellar arrangement in the middle and inner layers, respectively; (C) pangolin scales are composed of lamellar keratin that gradually change the orientation from being nearly parallel to the surface at the base to approximately 45° tilted at the top in the intermediate layer. (A-C) Reprinted from Progress in Materials Science, Vol. 88, Liu, Z., Meyers, M. A., Zhang, Z., Ritchie, R. O., "Functional gradients and heterogeneities in biological materials: Design principles, functions, and bioinspired applications", pp. 32, Copyright (2017), with permission from Elsevier ³⁷.

While the primary focus in designing implants, as mentioned in previous sections, is often on achieving long-term stability at interfaces, a critical aspect that can be frequently overlooked is

the potential difficulty in removing these devices should complications or infections arise⁴⁰. In dentistry, for example, Adler et al. highlighted the long-term outcomes after implant therapy, yet, concluded that the prevalence of biological complications, such as bone loss, soft tissue recession or hypertrophy, occurs with a likelihood of 52% at the patient level⁴⁰. This necessitates the removal of the implant, and, with that, the soft tissue may start to collapse within minutes of the separation, and potentially become trapped between the implant platform and prosthetic component, causing swelling and inflammation of the surrounding tissue 41. A similar complication can occur with other bioimplants, creating a significant need for the development of devices that are both strong and easily removable One area of research has focused on eliminating the need for surgical removal by creating implants that can fully dissolve in the body⁴². Over time this implant has to be gradually broken down through absorption by the tissue and replaced by natural tissue⁴². However, it remains challenging to find the balance between gradual degradation and mechanical strength of the implant. To date, there have been no effective solutions or examples in nature to fully address these complexities. However, the Mytilus edulis mussel byssus serves as an excellent model for designing both, soft-hard and living/non-living interfaces. Its distinct interfaces, ranging from the stiff plaque to a soft stem, function synergistically under high loads from crashing waves present in the marine intertidal zone where it resides⁴³. In addition, mussels possess the remarkable ability to release the strongly anchored byssus on demand, allowing for flexibility while maintaining structural integrity⁴⁴⁻⁴⁶. This unique combination of properties makes the mussel byssus an invaluable resource for bio-inspiration and the development of advanced interfaces.

1.5. Interfaces in *Mytilus edulis* mussel byssus

Mytilus edulis is commonly known as the Blue Mussel, and belongs to the Mytilus species complex, which also encompasses M. galloprovincialis, M. trossulus, and potentially additional species^{47, 48}. It is naturally spread across the temperate regions of the Northern and Southern Hemispheres^{48, 49}. When mussels mature, they tend to cluster around other mussels and interconnect with one another using byssal threads.to form extensive beds on rocky surfaces characteristic of the shallow subtidal and intertidal zones⁵⁰. To achieve this, each mussel produces an average of 50 to 100 individual byssal threads which they use to attach onto hard surfaces including rocks and the shells of other mussels. One end of each thread attaches to the surface using the adhesive plaque (a strong, porous underwater glue), while the other end, known as the byssus stem root, is embedded in the mussel's soft living tissue ⁵¹. Between the plaque and stem root, there is the distal thread, followed by the proximal thread region, and then the stem (in order from surface to tissue) ⁵¹. Indeed, mechanical mismatch occurs across all the different regions of the mussel byssus: (i) at the substratum-plaque interface; (ii) plaque-distal connection; (iii) in the stiff distal to soft proximal thread transition; (iv) at the junction between the proximal thread and stem; (v) the transition from the stem to the stem root; and finally (vi) the attachment between the stem root and the soft living tissue, called the generator (Fig. 1.8)⁵². In this thesis, I will focus on the interfaces (iii) and (vi). Interface (iii) at the distal-proximal junction is a soft-hard interface, while interface (vi) at the junction of the stem and tissue is a non-living/living interface.

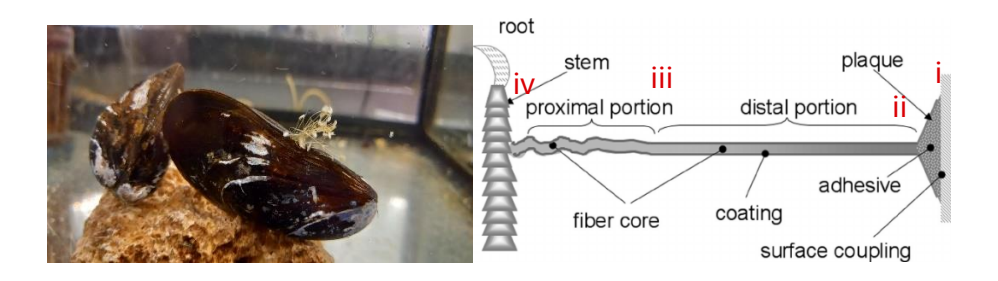


Figure 1.8. The Mytilus edulis mussel produces several byssal threads Each individual thread extends from the stem, embedded in the living tissue, to the distal adhesive plaque. Rights managed by Taylor & Francis⁵³.

1.5.1. Distal-Proximal Thread Interface

a. Composition of the byssus core

Each byssal thread comprises three distinct regions— plaque, cuticle, and core—which possess unique compositions, structural organization, and functions (Fig. 1.9A)⁵⁴. The plaque consists of numerous proteins rich in the unusual post-translationally modified amino acid 3,4-dihydroxyphenylalanine (DOPA) that are organized into an open-cell foam and serve as an underwater glue that stick to almost any surface chemistry ⁵⁴. The cuticle is a thin layer that coats the thread that combines high extensibility and high stiffness/hardness due to the presence of DOPA-metal coordination cross-links ^{54,55}. The core, which is one of the main focal points of this thesis, forms the innermost part of the thread and consists of a family of collagenous proteins called preCols that are organized into a semi-crystalline array⁵⁵. There are three variants of preCols (preCol-D, -P and -NG) and each possesses a central collagenous domain with a repetitive amino acid sequence motif Gly-Xaa-Yaa (where Xaa typically represents proline or glycine, and Yaa is hydroxyproline), variant-specific flanking domains on either side of the collagen domains,

and histidine-rich domains (HRDs) at the termini (Fig. 1.9B)⁵⁶. In addition, metal ions such as Zn and Cu were detected in byssus at up to 0.1% of dry weight, and were found to be coordinated by histidine residues in the preCols serving as dynamic cross-links ⁵⁷. Notably, the three preCols with distinct flanking domains exhibit different distributions in the thread ⁵⁶. PreCol-P is predominantly in the proximal thread, preCol-D is predominantly in the distal thread, and preCol-NG exhibits a uniform, non-graded distribution in the thread ⁵⁶. PreCol-P and preCol-D will be the primary focus of this thesis.

PreCol-D has a molecular mass of 97 kDa and, within the distal thread, it is organized into tightly packed and straightly aligned fibrils^{58,59}. PreCol-P has a molecular mass of 95 kDa and within the proximal thread, it is more loosely arranged and appears as spring-like waves ^{58,59}. While the distal region is almost entirely comprised of preCols, approximately 34 mol% of the proximal thread is comprised another protein called proximal thread matrix protein 1 (PTMP-1) ⁵⁶. Its structure consists of two von Willebrand factor type A (vWA) domains connected by a two-β-stranded linker, which in vitro, bind with high affinity to collagen fibrils and influence collagen assembly, morphology of the fibrils as well as mechanical properties of the byssus ⁵⁶. More importantly, while preCol-D and -P share homologous HRDs and collagenous domains, they possess very distinctive flanking domains⁵⁶. The flanking sequence of the preCols in the proximal region, known as preCol-P, resembles traits of elastic fibrous proteins like elastin and spider flagelliform silk dominated by Gly, Pro, and bulky hydrophobic residues^{56,60}, which are believed to contribute to the elastomeric behavior of the proximal thread⁶⁰. On the other hand, the flanking domain sequences of preCol-D, resemble those of spider dragline silk fibroins, containing

repeated polyalanine runs separated by GGX spacer sequences, which in spider silk are organized microcrystalline antiparallel β -sheets⁶¹. β -sheet structure was verified in the distal thread with X-ray diffraction and shown to contribute to its stiffness, toughness, reversible extensibility, and self-healing response⁶². The third variant, PreCol-NG, contains flanking domains resembling the glycine-rich proteins found in plant cell walls⁶³. These domains feature tandem XGly_n repeats, where X represents alanine, leucine, or asparagine, and are assumed to functions as mediator between preCol-D/-P molecules⁶³.

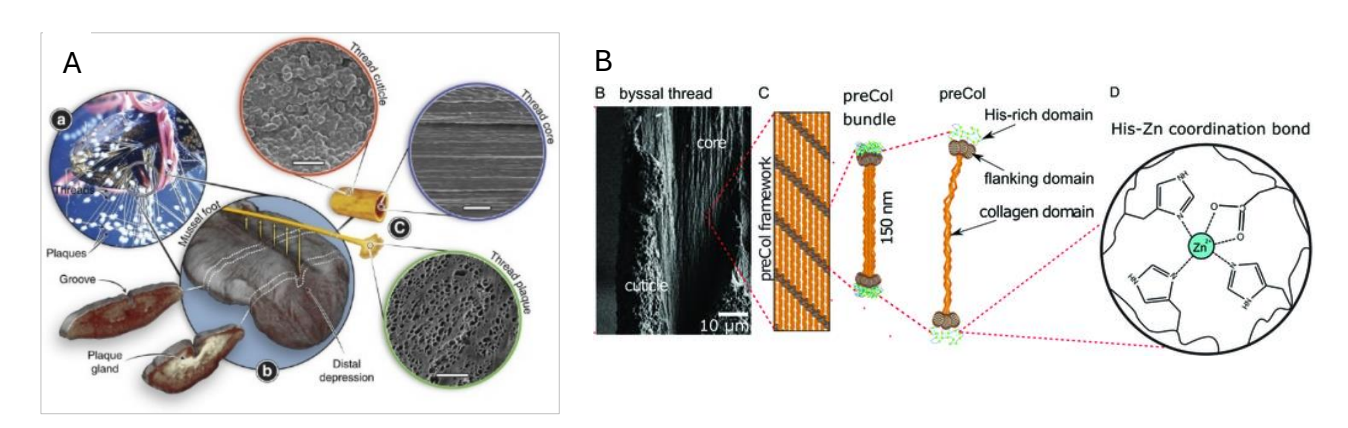


Figure 1.9.Mytilus edulis byssus hierarchical structure and composition. (A) An illustration of a mussel extruding threads , highlighting the complex micron-scale morphologies of the protective cuticle (scale bar, 3 μm), fibrous core (scale bar, 5 μm) and the adhesive plaque (scale bar, 50 μm); (B) SEM of byssal thread torn open showing core and cuticle. (C) Schematic of hierarchical organization of preCol proteins within the core^{54, 64}. (A) Copyright © 2017, Tobias Priemel, Elena Degtyar, Mason N. Dean & Matthew J. Harrington⁵⁴. (B) Used with permission of Canadian Science Publishing, from Following the thread: Mytilus mussel byssus as an inspired multifunctional biomaterial, by J. Herbert Waite and Matthew James Harrington, Canadian Journal of Chemistry, Volume 100, Issue 3, pages 197-211, published on January 1, 1951; permission conveyed through Copyright Clearance Center, Inc ⁶⁴.

b. Mechanical properties of the distal and proximal byssus

Such differences in the composition and structure between the variants play an important role in the mechanical function of the byssus⁵⁷. Mechanical testing of both the distal and proximal portions reveals that they have significantly different properties, such as stiffness (elastic modulus), toughness, and hysteresis⁵⁷. Stiffness represents material's ability to resist deformation under an applied stress⁶⁵, toughness refers to a material's capacity to dissipate energy and undergo plastic deformation before breaking⁶⁶, and hysteresis reflects a mechanical energy-damping capacity in cyclic loading⁵⁷. These terms can be calculated from the stress-strain curves obtained after subjecting the byssus to a pulling force (Fig. 1.10). For instance, stiffness (E) will be the initial slope of the stress–strain curve during loading and is calculated by dividing the stress applied to a material by the resulting strain⁶⁵. Here, tensile stress (σ) is defined as the applied force (E) normalized to the cross-sectional area (E) of the material (equation (E) have

$$\sigma = \frac{F}{A} (N/m^2) (4)$$

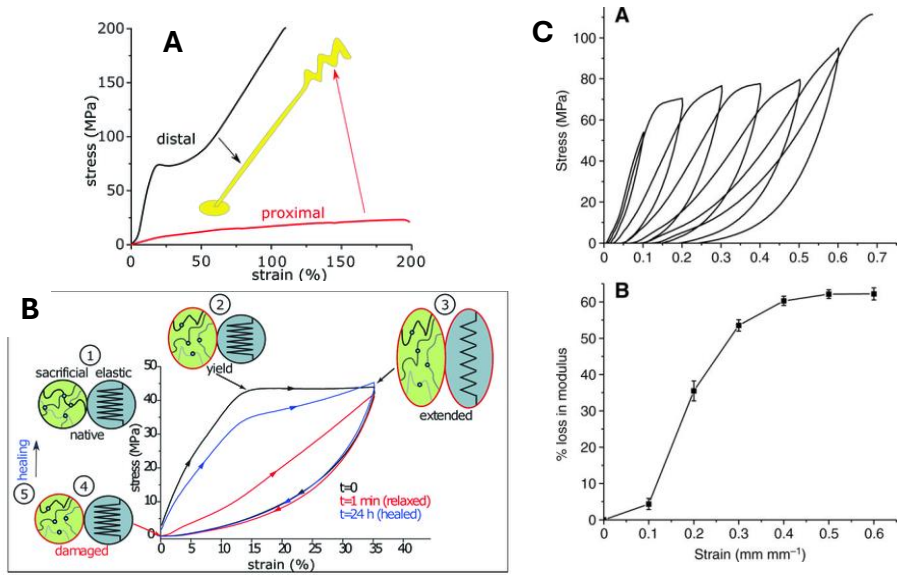
Strain, on the other hand, represents the material's deformation in response to the applied stress normalized to the starting length, as expressed respectively in the equations below (equation *(5)*)

65:

$$\varepsilon = \frac{\delta l}{L} \quad (5)$$

such that arepsilon is the strain, δl is the change in length and $\it L$ is the original length of the material 65 .

Applying these concepts to the byssus, the distal portion demonstrates an initial stiffness comparable to that of vertebrate tendon, which makes sense given their common collagenous



demonstrates significant hysteresis in the first cycle, damage in the second cycle, and a self-healing response in the third cycle. The illustrations depict a double network model, which includes sacrificial bonds (His–Zn cross-links) and an elastic network (cross-beta sheet flanking domains); (B) a)Stress–strain curve of a distal thread cycled with increasing strain values (10% to 70%),b) plot of percentage loss in modulus as a function of the strain that caused the loss; (C) Strain curves for the distal and proximal regions of byssal threads – pulled to break⁶⁴.(A-B) Used with permission of Canadian Science Publishing, from *Following the thread: Mytilus mussel byssus as an inspired multi-functional biomaterial*, by J. Herbert Waite and Matthew James Harrington, *Canadian Journal of Chemistry*, Volume 100, Issue 3, pages 197-211, published on January 1, 1951; permission conveyed through Copyright Clearance Center, Inc ⁶⁴. (C) Used with permission of The Company of Biologists, from *Holdfast heroics: comparing the molecular and mechanical properties of Mytilus californianus byssal threads*, by Matthew J. Harrington and J.

Herbert Waite, *Journal of Experimental Biology*, Volume 210, Issue Pt 24, pages 4307-4318, published on January 1, 1930; permission conveyed through Copyright Clearance Center, Inc⁶⁷.

composition. However, unlike tendon, the distal thread does not fail at 12% strain⁶². Rather it can extend over 100% strain before failure⁶². Additionally, the distal region shows behavior typical of a viscoelastic polymer, characterized by a linear response at low strain, followed by a discrete yield point indicating the transition from the linear elastic region to plastic deformation, a plateau, and final stiffening (Fig. 1.10A)⁶⁸. An additional observation in the distal thread was reported after the application cyclic loading⁶⁷. While yield and plastic deformation lead to permanent deformation in most thermoplastics, the byssus remarkably recovers back to its initial length almost instantly when load is removed⁶⁷. If the thread is cycled immediately after undergoing yield, it will exhibit a characteristic softening with an up to 60% loss in stiffness (Fig. 1.10B)⁶². However, the distal thread shows a distinctive ability to recover back to its initial properties over time in a highly unusual self-healing behavior not observed in standard thermoplastics. This has been attributed to the rupture and subsequent reformation of sacrificial histidine-Zn metal coordination bonds based on X-ray based investigations ⁶⁹.

The proximal region exhibits very different behavior than the distal region. For example, the proximal region has a more than 10-fold lower stiffness than the distal region, and it is much more elastomeric in its behavior, with approximately 200% extension at failure (Fig 1.10.C)⁵¹. Nevertheless, this material is still about an order of magnitude stiffer and stronger than the rubbery protein materials made from elastin and resilin⁵¹. In this context, strength refers to the

maximum stress that the material can sustain⁷⁰. While the distal and proximal regions of the thread have been tested separately and the mechanics of the whole thread has been measured, it has been experimentally challenging to observe the mechanical responses of the proximal and distal regions within the context of a whole thread test^{51, 71}. Hence, their potential contribution to the overall behavior of the thread structure remains uncertain, and more importantly within the scope of the current thesis, we have no concept of the mechanical response at the interface⁴⁹.

Notably, given the substantial difference in mechanical properties between the distal and proximal regions, the byssus rarely fails at the proximal/distal interface. It has been proposed that a graded distribution of preCols with different flanking regions is present along the axis of the thread to overcome the mismatch created by attaching the mussel's soft tissue (0.2 MPa) to a hard surface in the intertidal zone (25,000 MPa)^{59, 72}. Particularly, it is thought that preCol-D and -P are present in complementary gradients across the byssus, such that preCol-D being more abundant in the stiff distal region , the preCol-P more abundant in the elastic proximal region, while preCol-NG being evenly distributed ^{57, 70}. This was supported by the observation that the distal portion contains 79.2% preCol-D, 2% preCol-P, and 18.3% preCol-NG, while the proximal portion contains 44.3% preCol-D, 34% preCol-P, and 21.6% preCol-NG⁷⁰. However, the distribution of different preCols along the distal and proximal interface has not been characterized with high spatial resolution, nor the mechanism behind the gradient formation in native threads was clear at that stage⁷⁰. Better understanding of this gradient is a key focus of Chapter 4 of the thesis.

1.5.2. From the threads to the byssus stem

All the threads making up a single byssus converge at the stem, attached similar to tree branches stemming from a common trunk⁵². The stem is embedded within the soft living tissue of the mussel similar to the roots of a tree and extends outward from a cavity located at the proximal end of the ventral groove on the mussel's foot—the organ responsible for forming the byssus (Fig. 1.11A)^{52, 71}. Thus, there is a direct conduit from each plaque along the threads of a byssus into the living tissue of the mussel via the stem. To deepen the understanding of the molecular mechanism of load distribution and load transfer between the mechanically dissimilar stem and threads, researchers explored the chemical composition of the proteins in the foot and generator⁵². Their findings revealed that a protein gradient of a different preCol-P variants exists, with the highest concentrations found at the proximal end of the thread⁵². The preCol-P variants are assumed to impart extensibility and elastic recoil to the outer surface of the stem, known as the ring (Fig. 1.11B), and function as a 'dovetail' between the proximal thread and the byssal stem⁵². In addition, the amino acid composition of the stem differs significantly from that of the threads, with glycine and hydroxyproline levels reduced by more than 50% compared to the threads, suggesting a lower content of collagen (i.e., preCols)⁵². Furthermore, a study reported an ultimate strain of 0.9 (mm/mm) for the stem, which is less than half the strain of proximal threads⁵². Structurally, the byssal stem is complex ⁷³. In early studies from the 1950s, it was reported that the stem has a β -keratin-like structure using wide-angle X-ray diffractograms⁵². Later, it was described that the core of the stem consists of a materials exhibiting a laminated pattern that is sheathed with overlapping rings (Fig. 1.11A)⁷³. The proximal regions of the threads are fused to the rings, yet the extent to which the proximal thread fibers (preCol-P) extend into the ring has not been determined⁵². However, in the generator, the stem splits to form the root portion (stem root) that consists of parallel laminar sheets (lamellae) (Fig. 1.11B)⁷³. Initial investigations suggest that sheets concentrically mold to one another and extrude from the generator⁷³. Yet, little has been done to further characterize this crucial interface since the 1970s⁷³.

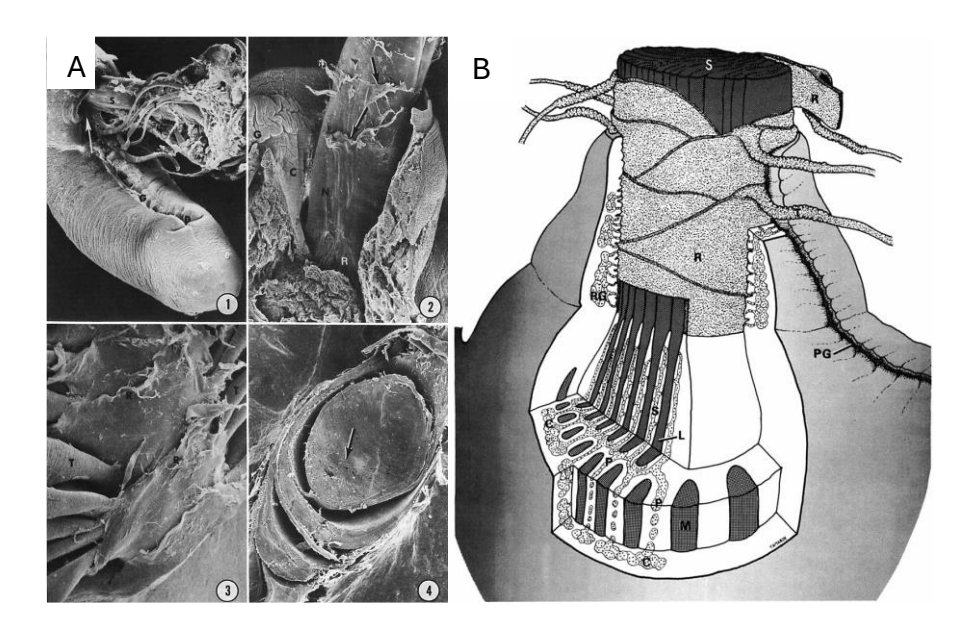


Figure 1.11. SEM images and illustration of the hierarchical structure of the stem and generator.

A) SEM images of 1)Mytilus foot- Stem (S), threads (T), ventral pedal groove (G), distal depression (D). Mag. approx. x 20. 2) tissue collar (C) cut away to show neck (N) of stem and continuation of the groove (G). Mag. approx. X 40. 3)surface of stem showing overlapping rings upon the proximal portion of the threads (T). Mag. approx. X 50. 4) cross section of stem showing laminations in the central core and concentric pattern due to the overlap of consecutive rings. Mag. approx. X 50⁷³. B) Model of the byssus stem generator structure, where (M) is the byssus retractor mussel: (C) secretory granules; (P) granule conducting process; (S) the septa; (L) lamellae; (RG) glands for thread attachment ring; (R)stem ring; (T) threads; and (S) stem core

⁷³. (A-B) Reprinted from Journal of Morphology, Vol. 145, Issue 2, Arnold Tamarin, "An ultrastructural study of byssus stem formation in Mytilus californianus," pp. 27, Copyright 2005, with permission from John Wiley and Sons ⁷³.

1.6. Dynamic living / non-living interface

Fabrication of the stem and byssus threads constitutes a significant metabolic cost for mussels 74. For example, in control groups with minimal thread production, the energetic cost of byssal thread production accounts for 2% to 8% of the total energy budget⁷⁴. However, in mussels induced to produce threads daily, this cost increases six to eleven times, reaching up to 47% 74. Despite the energy-demanding process, mussels sometimes 'choose' to jettison their entire byssus apparatus from the generator tissue through a poorly understood quick-release mechanism, enabling them to adjust their movement patterns, crawl across surfaces, and subsequently form a new byssus^{11, 75}. This is remarkable given that the byssus interface is extremely strong and able to resist a constant onslaught of crashing waves. This ability to suddenly release the entire byssus on demand may be triggered by environmental factors such as fluctuations in salinity, desiccation, temperature, and oxygen tension, as well as by the diverse foraging behaviors of predators ^{11, 75}. Nonetheless, this remains somewhat speculative and the biochemical mechanisms underlying release induced by these factors have not been studied in detail. The ability of mussels to reform an entire byssus within a few hours after its release, and the direct contact between the stem root and the cilia identified in previous ultrastructural investigations⁷³, points to the possibility of mussels being able to biologically regulate the release in a safe manner, despite its strong attachment to the tissue. Therefore, in Secions 3 and 4, I will focus on investigating the structural characteristics of this interface and elucidating the mechanisms underlying its release process.

1.6.1. Fabrication of the byssus and stem

While previous sections have focused on the remarkable hierarchical structure of the mussel byssus and the key interfaces present, here we focus on how the byssus with its distinct interfaces is fabricated by the mussel. Recent work highlights that the byssus is formed via secretion of fluid condensate protein precursors by the mussel foot that self-organize and assemble in just minutes ⁵⁴. Somehow, the spatial arrangement of precursor proteins in the byssus is dictated by their storage and organization within the secretory glands of the foot and the generator tissues ⁵⁴. In this section, I will discuss the foot and generator separately, as no relationship has yet been established between the two in terms of structure and little is known about the distribution of the various precursors across the entire generator-to- foot range.

a. Mussel Foot

The mussel foot contains three specialized glands that play a key role in the formation of the byssus plaque, cuticle, and core, respectively⁵⁴. Each gland produces and stockpiles secretory vesicles with distinctive sizes and morphologies (Fig. 1.12)⁵⁴. The vesicles in the cuticle and plaque gland are spherical and contain disordered non-collagenous proteins⁵⁴. The cuticle vesicles are confined to two narrow strips on each side of the ventral foot groove, while the plaque vesicles are observed near the end of the foot ⁵⁴. The core vesicles (containing the preCol proteins), on

the other hand, exhibit an ellipsoidal shape and are stored in an elongated gland running along the entire length of the foot and comprising the largest volume⁵⁴.

When secreted, the fluid condensate contents of the vesicles transform into a thread through a process similar to polymer injection molding in which proteins are released into the foot groove, coalesce, and spontaneously assembled into a complex-structured thread (Fig. 1.12c)⁷⁶. For example, the preCols within the core vesicles are initially well-aligned and stored as a smectic liquid crystalline (LC) phase, which is believed to be crucial for rapid self-assembly of the thread hierarchical structure⁵⁴. Particularly, the preCol precursors align both orientationally and positionally in a way that resembles the final fiber structure, ensuring close contact between the flanking domains and His-rich domains of adjacent preCol bundles⁷⁶. These domains are unfolded and partially extended in vesicles yet become highly folded within the thread 76. Some factors that might play a role in this behavior are the pH-switch from the slightly acidic vesicle conditions to seawater pH, oxidative cross-linking of the DOPA at high pH, and possibly the biologically regulated mechanical drawing by the foot⁷⁶. While such reactions occur in all preCols, it is unclear whether its variants (preCol-P/D/NG) are stored together or separately within the vesicles, nor how this organization impacts the assembly of the distal-proximal byssus interface. That aspect will be addressed in Chapter 4. Aside from core assembly, the proteins in the dense fluid phase of plaque vesicles attain a foam-like structure, in which the fibrous core would penetrate like roots⁵⁴. Similarly, the cuticle proteins coalesce and create a granular coating on the core⁵⁴. Nonetheless, this overall thread formation is only confined to the length of the pedal groove along the foot.

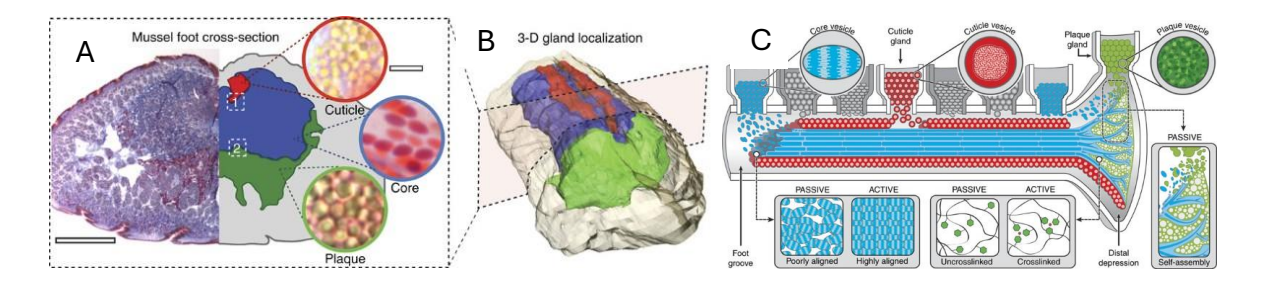


Figure 1.12.Schematics representing the storage of precursors in foot and the self assembly of byssal thread. Mussel foot cross-section stained with Trichrome (scale bar, 1 mm) (left), accompanying a colour-coded drawing of the localization the three secretory glands (right). Each gland consists of vesicles taken by a light microscope (scale bar, 3 μm for all three images); (B) 3D reconstruction of a mussel foot using the same colour scheme shown in a); (C) Model of the byssus assembly ⁵⁴. (A-B) Copyright © 2017, Tobias Priemel, Elena Degtyar, Mason N. Dean & Matthew J. Harrington⁵⁴.

b. Mussel generator tissue

Very little is currently known about the formation of the stem, mostly originating from a single study by Tamarin in 1975⁷³. At the proximal end of the mussel foot groove in which the thread is formed, it links to the cervical crevice around the neck of the stem, acting as a continuous mold which determines the shape of the thread and its attachment to the stem (Fig. 1.11B)⁷³. The protein precursors secreted into the cervical crevice is hypothesized to form the ring of the stem and is secreted from the glands situated peripheral to the muscles in the tissue collar surrounding the stem neck (Fig. 1.13)⁷³. In this region, the so-called 'type 1' cells are present, containing secretory granules that appear similar to preCol vesicles involved in thread formation in the foot ⁷³. The type 1 vesicles are transported through long extensions of cells, which terminate between

the ciliated cells at the crevicular surface ⁷³. Later, the vesicles are ejected via exocytosis (Fig. 13)⁷³. In addition, 'type 2' cells, which contain smaller, denser granules with a more cylindroid shape, were identified in the musculo-glandular zone that is proximal to the base of the septa⁷³.

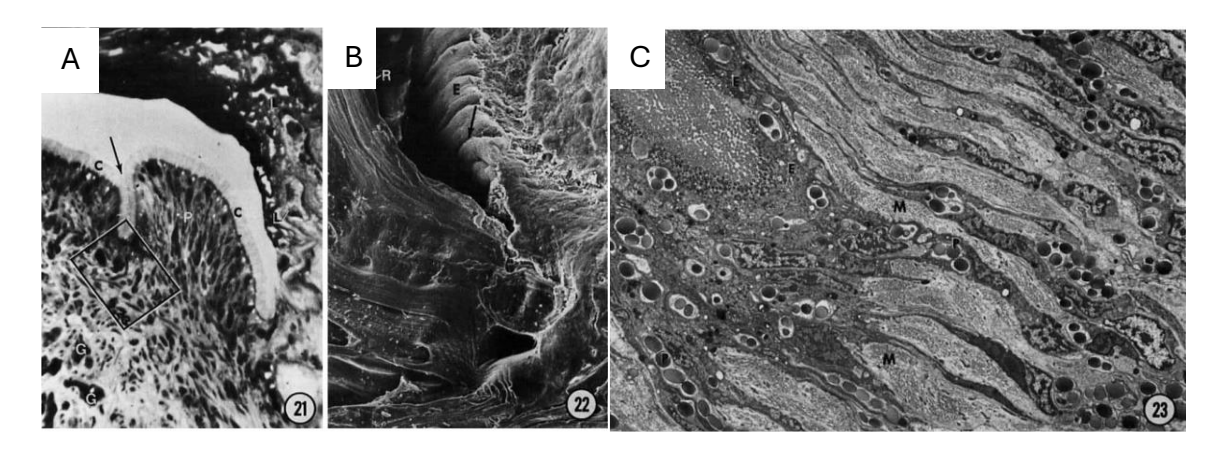


Figure 1.13.TEM images of the cervical crevice region. A) Ciliated epithelial surface 'C' displaying infolded pleats, gland lobules 'G', and granule-conducting processes 'P'. The rectangle indicates the area shown in figure (C). Magnification approximately X 500. SEM ⁷³. B) A Cut through the cervical crevice, showing epithelial surface of tissue collar 'E', stem 'S' covered by a thick layer of material secreted from the crevicular surface, i.e. the thread attachment ring 'R'. Mag. approx. X 300 ⁷³ C) Formation of ring in tissue collar (rectangle in figure (A)), where a Conducting type 1 granules 'P' transport between muscle bundles 'M' and terminate between ciliated epithelial cells 'E' at crevicular space 'C'. Mag. approx. X 3,400 ⁷³. (A-C) Reprinted from Journal of Morphology, Vol. 145, Issue 2, Arnold Tamarin, "An ultrastructural study of byssus stem formation in Mytilus californianus," pp. 27, Copyright 2005, with permission from John Wiley and Sons⁷³.

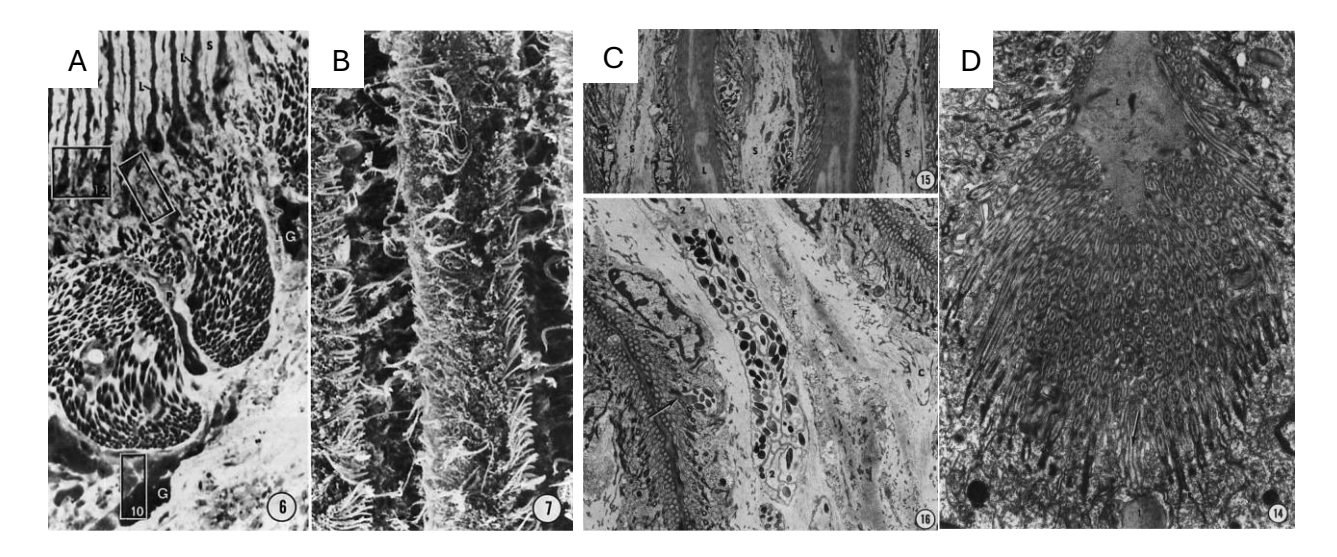


Figure 1.14.Microscopy images of the granules stored in the generator septa. Light microscope image of the musculo-glandular region and base of generator, where (M) is Muscle bundles; (G) is aggregation of secretory cell bodies; (P) is granule conducting processes; (S) is septa; (L)root lamellae within loculi. Mag. approx. X 300⁷³. B) SEM image of a cut surface showing the cilia in the generator septa extending into locular spares. Mag. approx. X 3,000. C) TEM images of i) generator septa and the biphasic lamellae bounded by ciliated epithelium and type 2 granule conducting processes. Mag. approx. X 6,400. ii) generator septum having long segments of type 2 cell processes Mag. approx. X 11,000⁷³. (D) TEM image of the base of loculus revealing arrangement of cilia and longitudinal aspect of type 1 cell. Mag. approx. x 15,000⁷³. (A-D) Reprinted from Journal of Morphology, Vol. 145, Issue 2, Arnold Tamarin, "An ultrastructural study of byssus stem formation in Mytilus californianus," pp. 27, Copyright 2005, with permission from John Wiley and Sons ⁷³

During the secretion process, it was proposed that the secretory vesicles will propel through the action of cilia and mix to finally form a homogeneous biphasic matrix of lamella between the

septa⁷³. However, experimental evidence for this process is lacking. It is important to emphasize here the proximity between the lamellae sheets and the cilia, as this relationship will serve as a fundamental concept in Chapter 2 and 3. Nevertheless, currently little is known about the temporal secretion of two variants and their transformation into the lamellae sheets and stem, comprising multiple interfaces, aside from a paper published in the 1975, which has been referenced in my previous descriptions of the byssal stem structure ⁷³.

Chapter 2

2. A strong quick-release biointerface in mussels mediated by serotonergic

cilia-based adhesion

Preface

A major theme of this thesis is how nature engineers biointerfaces and what humans can learn from extracted biological design principles. The juncture between soft living tissue and hard nonliving materials is one of the most complex interfaces for humans to engineer. Even more challenging is to make such an interface reversible and removable. Yet, successfully producing such strong and dynamic biointerfaces is critical in numerous biomedical applications. In this chapter, I describe work to understand the design of the mussel byssus stem biointerface by which mussels have evolved a strong, yet mechanically tunable bio-interface between soft extracellular matrix tissue and the stiff byssus biopolymer, which is capable of on-demand quick release by the organism. Employing a cross-disciplinary approach harnessing methods from biology, chemistry, and materials science, the mechanism of byssus strength and release was uncovered and shown to involve neurobiologically controlled activation of billions of motile cilia. Chapter 2 is reprinted with permission from Sivasundarampillai, J.; Youssef, L.; Priemel, T.; Mikulin, S.; Eren, E.D.; Zaslansky, P.; Jehle, F.; Harrington, M.J., A strong quick-release biointerface in mussels mediated by serotonergic cilia-based adhesion, Science 2023, 382(6672), 829–834. J.S. and L.Y. contributed equally to this work.

2.1. Abstract

The mussel byssus stem provides a strong and compact mechanically mismatched biointerface between living tissue and a nonliving biopolymer. Yet, in a poorly understood process, mussels can simply jettison their entire byssus, rebuilding a new one in just hours. We characterized the structure and composition of the byssus biointerface using histology, confocal Raman mapping, phase contrast—enhanced microcomputed tomography, and advanced electron microscopy, revealing a sophisticated junction consisting of abiotic biopolymer sheets interdigitated between living extracellular matrix. The sheet surfaces are in intimate adhesive contact with billions of motile epithelial cilia that control biointerface strength and stem release through their collective movement, which is regulated neurochemically. We posit that this may involve a complex sensory pathway by which sessile mussels respond to environmental stresses to release and relocate.

2.2. Introduction

Producing mechanically stable biointerfaces between living tissues and non-living materials is a challenge with relevance for applications in tissue engineering^(1, 2), wearable sensors⁽³⁾, neural implants ⁽⁴⁾, and advanced cellular diagnostics ⁽⁵⁾. In addition to concerns about biocompatibility and functionality, mechanical factors are central in designing effective biointerfaces ^(4, 6). For example, modulus mismatch occurs when stiffness and/or Poisson's ratios of materials in contact are significantly different, leading to localized stresses that can cause interfacial failure ^(7, 8). Designing effective interfaces for bionic implant materials is particularly tricky given the large disparity in mechanical properties between soft tissues (e.g., extracellular matrix (ECM), brain tissue) and typical implant materials (e.g., TiO₂, semiconductors) ⁽⁴⁾. Additionally, implant

exchange or device removal, when necessary, can also cause tissue damage ⁽⁹⁾. There is thus a need for biointerface designs that are mechanically stable, yet easily removed on demand. Nature provides valuable role models for bio-inspired design of biointerfaces between mechanically mismatched tissues (e.g., squid beak, marine worm jaws). In these examples, mechanical mismatch is mitigated through compositional, structural, and mechanical gradients ^(7,8). However, these solutions are not conducive to on-demand release of the interface. In contrast, we focus here on the biointerface between the mussel byssus stem root and the mussel foot (the byssus-producing organ), which provides a natural example of a strong, yet removable and rebuildable mechanical interface between a living tissue and a non-living biopolymeric material (Fig. 2.1A-B) ⁽¹⁰⁻¹²⁾.

The byssus comprises an array of proteinaceous attachment threads used by mussels to anchor in seashore habitats against forces from crashing waves and predators ⁽¹³⁾. For *Mytilus* mussels, each byssal thread is glued at its distal end to a hard surface using an adhesive plaque and is attached at its proximal end to the stem, like branches on a tree trunk (Fig. 2.1C). At its base, the cylindrical external stem transitions into the more flattened and tapered internal stem root ⁽¹⁴⁾. The stem root anchors the entire byssus into the living tissue at the base of the foot in a region known as the generator, which is also the secretory tissue responsible for forming the stem (Fig. 2.1A-C) ⁽¹²⁾. Given the forces exerted by crashing waves whose velocities can exceed 30 m/s(15), this necessitates a strong interface. However, *Mytilus* mussels are inexplicably able to jettison their entire byssus on demand and then fabricate a new one in hours ^(14, 16, 17). While the cues that induce this behavior are still unknown ⁽¹⁷⁾, byssus release enables sessile mussels to regain

mobility and crawl across substrates ⁽¹⁴⁾ and even to scale vertical surfaces (Fig. S 2.1). Such movements may allow mussels to relocate and escape unfavorable conditions (e.g., elevated temperature, predators, wave exposure, unsuitable substrates) ^(14, 18-21). Thus, while the interface between the stem biopolymer and the generator tissue must be very strong to resist wave forces, its strength must also be dynamically tunable to enable quick release. Recent investigations of a distantly related mussel, *Atrina Pinctada*, revealed a chemical interaction at the stem root-tissue interface mediated by metal coordination and sugar binding ^(10, 11). However, extremely little is understood about the byssus release mechanism of *Mytilidae* mussels and its relationship to stem root ultrastructure ^{12, 17}.

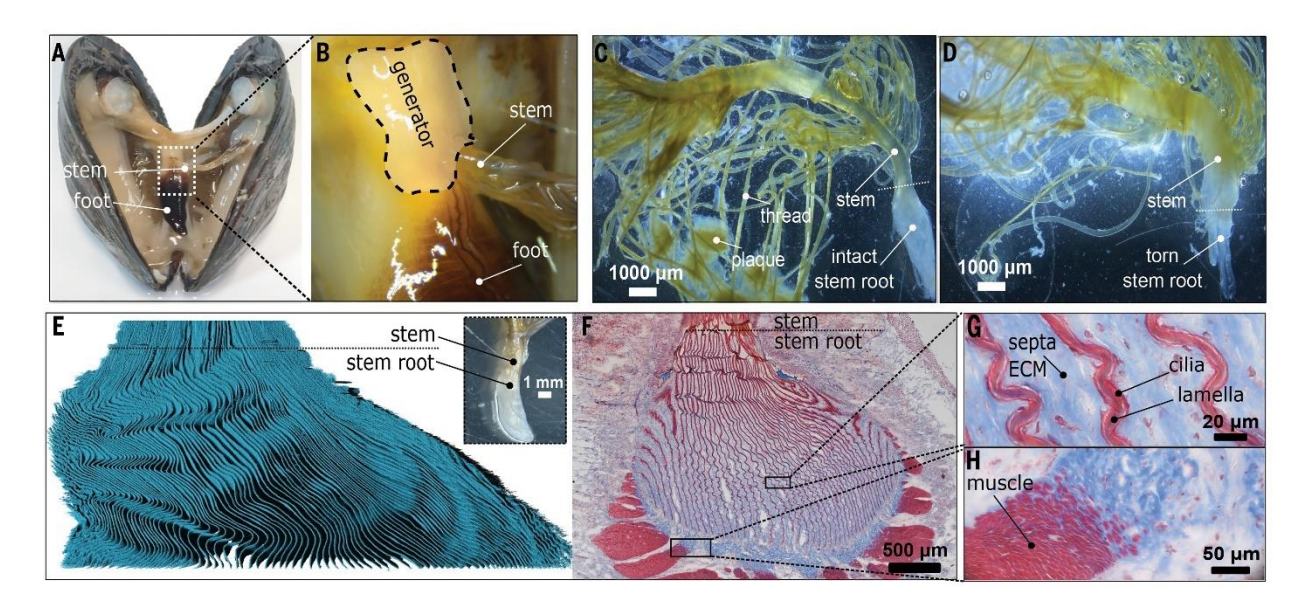


Figure 2.1 Mussel byssus stem root microscale hierarchical structure. Opened mussel with magnified area highlighting (B) the generator—the region of the foot that produces the stem and in which the stem root is embedded. (C) Image of cleanly released byssus highlighting the intact stem root—the region of the stem embedded in the generator. (D) Image of forcibly released byssus highlighting the damage to the stem root. White dashed lines in (C) and (D) indicate the

approximate boundary between stem and stem root. (E) Section through a false-color 3D reconstruction of a PCE-μCT dataset acquired from the generator region, showing the wavy lamellar sheets of the stem root (movie S2.1). The space between lamellae is where the ECM is located. Inset gives approximate orientation of the stem root in the μCT sample. (F) Trichrome-stained histological section from the generator region showing interdigitation of the wavy lamellar sheets that comprise the stem root. Black dashed lines in (E) and (F) indicate the approximate boundary between stem and stem root. (G and H) Zoomed-in images from (F) showing structural details of (G) the lamellae-cilia interface and (H) the generator-muscle interface.

2.3. Results and Discussion

Dynamic stem interface mechanics

To investigate the mechanical integrity of the stem root biointerface, we forcibly removed the byssus using a tensile tester and recorded maximum force values of 6.4±1.6 N (Fig. S 2.2 and S 2.3). Consistent with previous reports ⁽⁷⁴⁾, the tips of the majority of forcibly extracted stem roots appeared torn and frayed (Fig. 2.1D) indicating that part of the stem root broke off. However, mussels occasionally released the entire stem root, leaving a smooth and tapered appearance at the tips, similar to stem roots that are jettisoned by mussels spontaneously (Fig. 2.1C, Fig. S 2.1) ⁽⁷⁴⁾. To investigate this clean release phenomenon further, we manually applied a sustained subcritical force (i.e., below the breaking force) on the byssus, revealing that numerous mussels could be induced to release the byssus cleanly (Fig. S 2.4, Movies S2.2 and S2.3), leaving intact stem roots. While the conditions

that favor byssus release in nature remain unknown ⁽¹⁷⁾, these observations indicate the stem-tissue interface is capable of sustaining large forces before rupture; yet, under certain conditions the entire interface can be cleanly released under subcritical forces without obvious damage ⁽¹⁴⁾

Hierarchal structure and composition of the stem-generator biointerface

To better understand the paradoxical high strength and quick release of the stem root biointerface, we analyzed the hierarchical structure of the generator region of the foot – the soft tissue in which the stem root is formed and anchored (Fig. 2.1A-B). Phase contrast-enhanced micro-computed tomography (PCE-μCT) images of the generator region were computationally reconstructed and segmented to generate a 3D image of the stem-generator biointerface with micron resolution (Fig. 2.1E, Movie S2.1). The reconstructed image reveals that within the generator region, the stem root comprises more than 40 individual sheets, previously named lamellae (12), each of which possess a thickness of 2-3 μm and a characteristic wavy morphology (Fig. 2.1E). While the spaces between the lamellae observed in the PCE-μCT reconstruction are filled with the soft tissue of the generator, they become compressed together at the exit of the generator, forming the cylindrical external region of the stem (Fig. 2.1E). This highlights the continuity between the soft living generator tissue and stiff non-living byssus, indicating that forces transmitted through the threads to the stem will converge and concentrate in the generator at the interface between the lamellae and the soft tissue.

Histological cryosections cutting through the stem to the base of the generator reveal additional compositional and structural details (Fig. 2.1F-H). Staining with Masson's trichrome was used to localize collagenous (blue) and non-collagenous (red) protein components. The wavy morphology of the lamellar sheets interdigitated into the generator is evident in the histological sections, consistent with PCE-μCT and an earlier ultrastructural study (Fig. 2.1F) (12). At higher magnification (Fig. 2.1G), the lamellae possess a blue-staining core suggesting a primarily collagenous nature of the byssus stem tissue. The area between two lamellae, named the septa, also stains positive (blue) for collagen with purple-staining nuclei peppered throughout, indicating its extracellular matrix (ECM)-like nature. The lamellae and septa ECM are separated by a thin red-staining region with a feathery morphology (Fig. 2.1G), which is consistent with cilia, as previously indicated by Tamarin (12). The collagenous septa ECM is connected directly to red-staining byssus retractor muscles at the base of the generator, which can apply a tensile force to the entire byssus (Fig. 2.1F, H) (16), showing the continuity between the byssus and the musculature.

To observe the interface between the generator septa and the stem root lamellae at higher resolution, we utilized FIB-SEM, which enables 3D reconstruction of small tissue volumes with ~20 nm resolution. Figure 2.2A shows a single image from the FIB-SEM image stack, highlighting key features (i.e., septa, cilia, lamellae, and secretory vesicles) in false color, which were then reconstructed in 3D using the FIB-SEM image stack (Fig. 2.2B-C, Fig. S2.5, Movie S2.4). This highlights the direct and intimate interaction between the cilia and the lamellar material, with indentations apparent where the cilia contact the surface of the lamellae (Fig. S2.5). Previously

identified secretory vesicles containing protein precursors for building the stem ⁽¹²⁾ are seen lined up at the septa-lamellar interface (Fig. 2.2C, Fig. S2.5), with the cilia spreading apart, likely to enable vesicle secretion. It has been proposed that with each new byssal thread produced, the stem extends further out from the foot, suggesting an extrusion-like mechanism by which the stem grows ^(12, 22). The vesicles have a similar shape to the well-characterized secretory vesicles that contain liquid crystalline collagenous precursors that form the byssal threads⁽²³⁾.

Scanning transmission electron microscopy (STEM) imaging of the generator tissue provides additional details of the internal structure of the lamellae and the cilia-lamella interface (Fig.2. 2 D-G). While the lamellae appeared homogenous with FIB-SEM, the higher resolution of STEM reveals a heterogenous structure with a fibrous core and a more amorphous outer region that is in direct contact with cilia. The cilia can be assumed to be motile based on the characteristic organization of microtubules into a so-called 9+2 axoneme (24), in which 9 microtubule doublets surround two single microtubules in the center of the cilia. STEM images indicate that the cilia are tightly pressed into the outer layer of the lamellae, consistent with FIB-SEM imaging, suggesting that the lamella surface is relatively soft (Fig. 2.2E), while secretory vesicles can be seen pressed between cilia poised for secretion (Fig. 2.2F). The surrounding septa ECM exhibits randomly oriented thin fibrils with characteristic banding that we assume are collagenous based on histological staining (Fig. 2.2G).

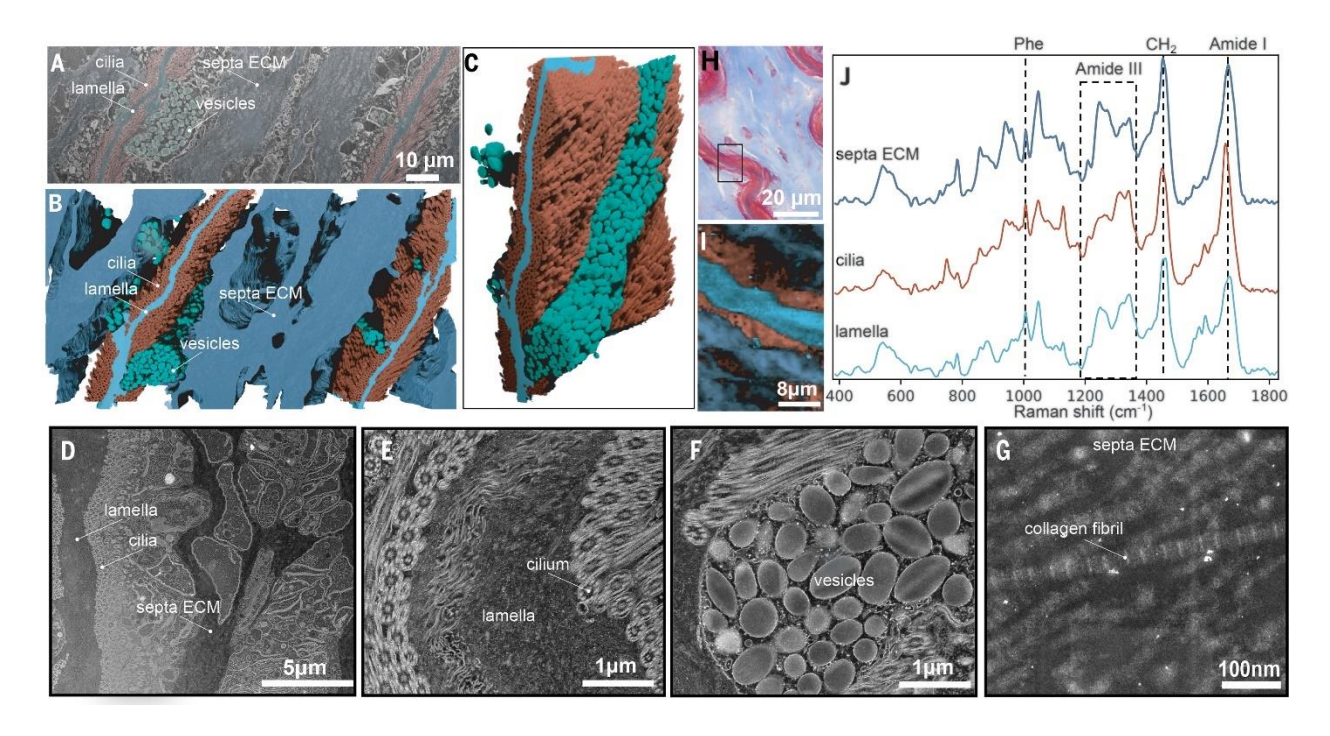


Figure 2.2. Structural and compositional analysis of the stem generator biointerface. (A) Single image from FIB-SEM image stack, showing key features with false color. (B) Reconstructed features in 3D from a FIB-SEM image stack. (C) Zoomed-in and slightly rotated image of the leftmost lamella from (B), highlighting cilia interaction with lamella. (D) Overview STEM image from the generator tissue. (E to G) Higher-magnification STEM images from lamella, vesicles, and septa, respectively. (H) Trichrome-stained generator section showing region similar to that in the confocal Raman image in (I). (J) Averaged Raman spectra acquired from regions of matching color in (I).

Confocal Raman spectroscopic imaging within the generator reveals further compositional details of the bio-interface between the septae and lamellae (Fig. 2.2H-J). Raman spectra acquired from the stem and lamellae resemble spectra acquired from the proximal byssal thread (25) confirming a primarily collagenous composition, while spectra acquired from the septa ECM

region are highly similar to spectra of type I collagen as seen by comparison with a mouse tail tendon control (Fig. S2.6). The region between the septa ECM and lamellae, where the cilia are observed with electron microscopy, is dominated by spectra consistent with alpha helical protein conformation based on the positions of the amide I and amide III bands, similar to previous Raman measurements of specialized cilia in the secretory ducts that form the byssus adhesive plaque ⁽²⁶⁾.

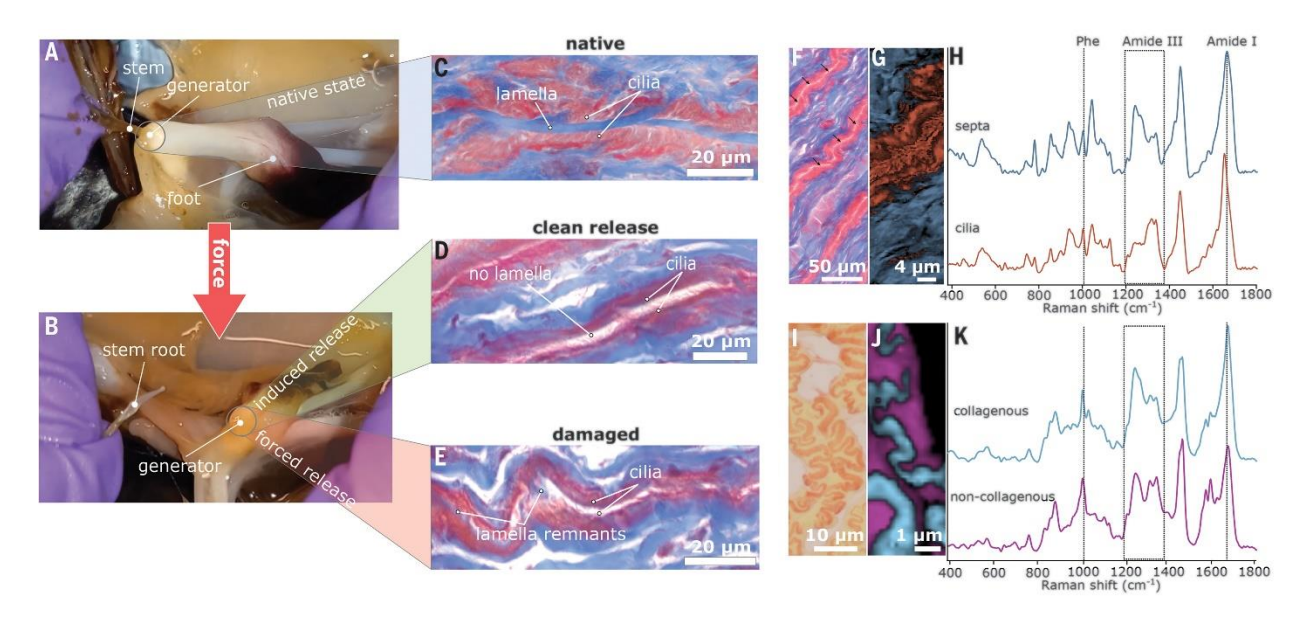


Figure 2.3.Histological and spectroscopic characterization of stem release. An opened mussel before (A) and after (B) removal of the byssus, highlighting the stem root. (C) Trichrome-stained section of the generator tissue with embedded stem root, highlighting complete lamella and surrounding cilia. (D) Trichrome-stained section of the generator tissue after induced stem root release, showing no signs of lamella between cilia. (E) Trichrome-stained section of the generator tissue after forced stem root release, showing remnants of lamella where the stem root broke off. (F) Trichrome-stained section of generator tissue after clean stem root release, showing empty space between cilia where lamella was (indicated by black arrows). (G and H) Raman image

and spectra, showing lack of lamella. (I) Sirius red-stained section of cleanly removed stem lamellae, showing biphasic composition of collagenous and noncollagenous components. (J and K) Raman image and spectra, highlighting biphasic composition of lamella.

Stem quick release response

Given the intimate interaction between the stem root lamellae with the cilia of the septa ECM, we investigated the tissue level effect of stem root release (Fig. 2.3). Byssus release was induced by applying a sustained subcritical force on the byssus as already described, showing no signs of damage to the stem root (Fig. 2.3A-B, Fig. S2.2, Movie S2.2). Histological analysis of the generator tissue immediately following induced stem release shows empty spaces between the cilia (Fig. 2.3D) where the lamellar sheets were observed in the native samples (Fig. 2.1G, 3C). Images indicate no damage to the red-staining cilia and no trace of the blue-staining lamellar material, supporting a clean release. Raman imaging of the generator tissue following induced stem root release further supports a clean, quick release with no associated tissue damage (Fig. 2.3F-H). Conversely, during forced removal where the stem root shows visible damage, we observe remnants of the broken lamellae in histological sections of the generator (Fig. 2.3E).

Cleanly released stem root lamellae were further analyzed by staining with Sirius red (Fig. 2.31), revealing intact undamaged sheets with no remnants of cilia or cellular debris attached. Consistent with STEM imaging, released lamellae show a red-staining squiggly fiber embedded in a non-staining material, confirming that lamellae are indeed biphasic with a fibrous collagen core component and a non-collagen component that is interacting directly with the cilia. Raman

spectroscopic imaging of the released lamellar material further supports a biphasic composition with the collagenous core spectra strongly resembling that of the proximal thread and the outer non-collagen component showing a more disordered secondary structure (Fig. 2.3J-K) (25).

Role of cilia motility and neurotransmitters in stem release

Based on the clean release of the stem lamellae, we make two hypotheses: 1) The interaction between the septa surface and lamellae is strong, yet reversible and non-covalent. 2) The release of the stem appears to be under biological control and likely involves the cilia, given their tight interaction with the lamellae. To test these hypotheses, we exploit the fact that beating of motile cilia in mussel gills and digestive system has been previously shown to be upregulated and downregulated in vitro by addition of serotonin and dopamine, respectively (27-30). To test if cilia beating movement might influence stem release, serotonin and dopamine were independently injected in a dose dependent manner into the open gap between stem and byssus without disturbing the tissue, and the maximum force to remove the stem was measured with mechanical testing (Fig. 2.4A, Fig. S2.2 and S2.3). Following injection of 200 µM serotonin, the byssus stem could be easily removed with such little force, that it was not possible to measure because the act of attaching the byssus to the tensile tester resulted in stem release (Fig. 2.4A, Movie S2.5). Serotonin showed a dose dependent effect with higher pullout force associated with lower serotonin concentration. In contrast, dopamine injection significantly increased the force to remove the stem to 20.1±5.9 N at 70 μM dopamine (compared to 6.7±1.7 N for controls in which only water was injected). Histological analysis of the generator at these high forces indicates remnants of ruptured lamellae in between septae (Fig. 2.3E). Dopamine also shows a clear dose dependence (Fig. 2.4A), but there was a large drop in the maximum force at 200 μM dopamine to 3.2±0.3 N. Further inspection reveals that in these samples, failure is not occurring because the stem is released, but rather because the entire generator ruptured and pulled away from the underlying musculature - although the stem-generator biointerface remains intact. This may suggest an important toughening role associated with partial cilia movement (Supporting text). These findings strongly implicate neurotransmitter regulated cilia movement in controlling the mechanical interaction between the living and non-living tissues, suggesting that the release process is serotonergic. To further explore this hypothesis, we dissected tissue from the generator and used light microscopy in differential interference contrast (DIC) mode to visualize and quantify the cilia beating velocity (Fig. 2.4B, Movie S2.5) (31). Freshly dissected tissue exhibited cilia movement for up to one hour following dissection, which is consistent with previous reports that dissection can lead to the activation of the serotonin pathways in mussels (32). Recording cilia maximum velocity using image tracking software (33, 34) (Fig. 2.4B-C, Fig. S2.7), we observed that addition of serotonin to the tissue in vitro resulted in a substantial increase of the number of beating cilia and an increased beating velocity, while addition of metergoline – a non-selective serotonin receptor antagonist (35) – resulted in a concomitant decrease both in the number of beating cilia detected and the beating velocity (Fig. 2.4C, Fig. S2.8, Movie S2.6). A subsequent second addition of serotonin again increased both the number of cilia beating and beating velocity, strongly supporting the role of the serotonin pathway in the stem release process.

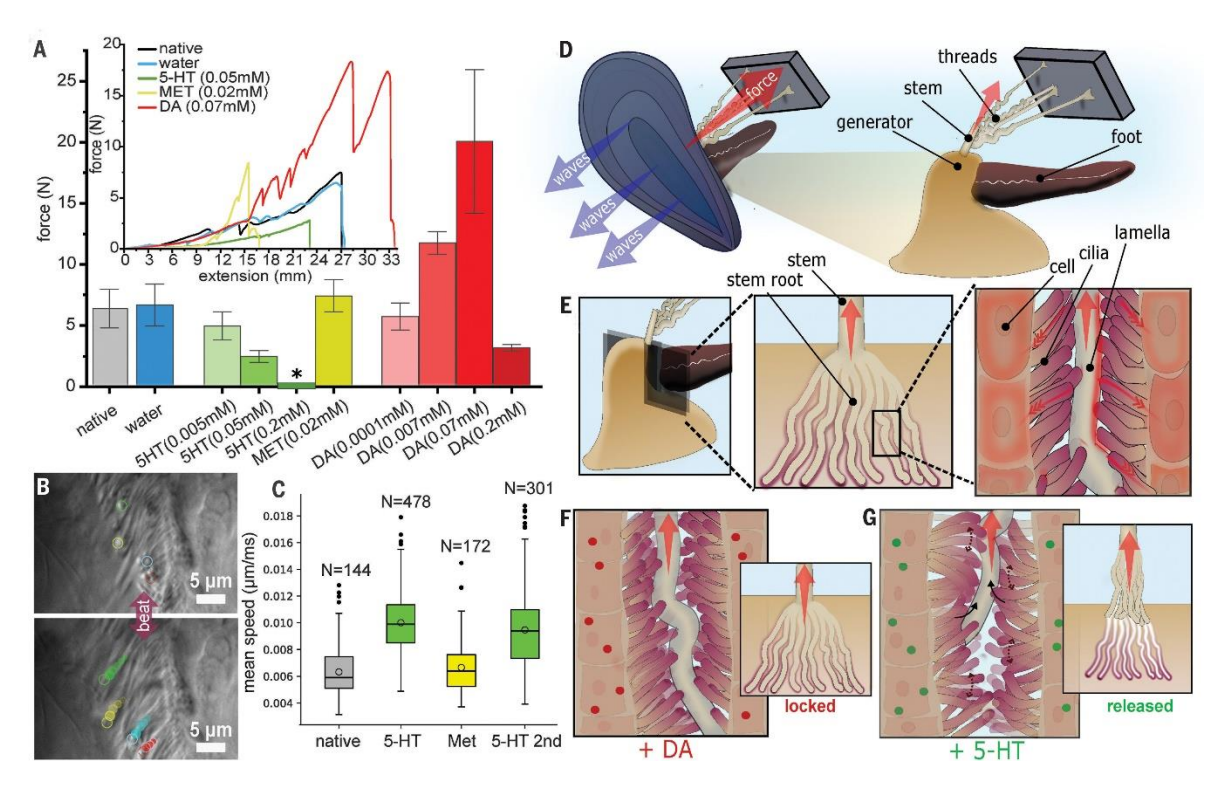


Figure 2.4.Role of cilia and neurotransmitters in stem release. Maximum stem root pullout force measured with a tensile tester under various treatments (5-HT, serotonin; MET, metergoline; DA, dopamine). The asterisk (*) for the 0.2 mM 5-HT treatment indicates that in all cases, the byssus came out during sample loading on the tensile tester, indicating very low pullout forces. Data are mean \pm SD with N \geq 5 specimens for each treatment. Inset show example force-extension curves. (B) DIC light microscopy still images from cilia video, showing tracking of cilia beating in dissected sections of generator tissue. Movement of four specific cilia is illustrated with colored circles. (C) Mean beating speed of cilia after consecutive treatments of the same region of tissue. Number (N) of cilia detected and tracked in each treatment is indicated on the plot. (D) Schematic showing how wave forces acting on the mussel are transmitted through the byssus into the stem and generator. (E) Schematic showing intimate interaction of lamellae with cilia on generator

epithelial cells. (F and G) Schematic representations of the effects of (F) dopamine and (G) serotonin on biointerface strength mediated by cilia beating.

The generator is a strong and serotonergic quick release biointerface

Mytilus mussels have evolved a remarkable solution for fabricating a strong, quick release biointerface by interdigitating stiff, wavy biopolymer sheets with living tissue and carpeting the surfaces with soft motile cilia. Yet, it is highly unusual for cilia to be employed for such a mechanically demanding task. ECM tissue is typically quite soft and viscoelastic $^{(36)}$ and the flexural stiffness of cilia is predicted to be extremely low $^{(37)}$. In contrast, given the similarity of lamella Raman spectra to byssal thread collagen proteins, we predict a high lamella stiffness of 50 - 500 MPa $^{(13)}$. How can we then reconcile the ability of this mechanically mismatched, submillimeter-scale biointerface to sustain repeated loadings of up to 20 N?

Using extracted values from light microscopy images, we can roughly estimate a value of 4.1 cm² for the interfacial area between the stem lamellae and the cilia based on their tight interdigitation (supplemental text). Given this surface area, a force of 20 N translates to a stress of only ~50 kPa distributed over the interface. For comparison, this same force would translate to a stress of 1.1 GPa in a single byssal thread, which is about 50× the proximal thread strength for *M. edulis* ⁽³⁸⁾ (incidentally, there are normally at least 50 threads in a mature byssus and failure most commonly occurs at the substrate⁽³⁹⁾). We estimate that there are approximately 5.7 billion cilia in contact with the lamellar surface (supplemental text). Therefore, if an applied force of 20 N is evenly distributed, each cilium would experience a force of approximately 3.5 nN. Similarly,

reversible adhesion by gecko toe pads is dependent on billions of densely packed tiny hairs called spatulae (similar to cilia in terms of size, aspect ratio and lateral packing density), each of which achieves adhesive forces of 2-16 nN primarily through van der Waals and other weak interactions (40-42). The collective action of many billions of such interactions on gecko toe pads enables large frictional forces when loaded in parallel (40). Similarly, the cilia-lamellar interface in the generator will be loaded parallel to the stem axis when a force acts on the byssus (Fig. 2.4D-E), enhancing the number of interactions and thus, force capacity. Furthermore, the interdigitation of multiple lamellae and septae is superficially analogous to the interleaving of pages from two phone books. In this popularized feat, shockingly large forces are required to pull apart the two books due to amplification of friction between the individual sheets enhanced by their bending angle (43). Similarly, the bending and interleaving of many lamellar sheets in the spaces between septae may further increase the pullout forces that can be sustained before failure.

Thus, the key question is not why the stem root biointerface is so strong, but rather how it is able to be released on demand without failure. To disengage from surfaces, geckos change the angle of applied force by rolling back their toe pads, which focuses stress on fewer individual bonds, precipitating quick release ⁽⁴⁰⁾. Perhaps analogous to gecko toe rolling ⁽⁴⁰⁾, we have observed that the motile cilia at the stem root biointerface can actively move relative to the lamellar surface under an appropriate neurochemical trigger (Fig. 2.4F-G). This oscillating motion apparently disrupts the adhesive interaction between the cilia and lamellae surface, enabling the release of the entire stem root under subcritical forces (Fig. 2.4G). Presumably, the number of cilia moving and/or the velocity at which they are beating can modulate the overall force required to remove

the byssus, enabling the observed serotonin and dopamine dose-dependency of pullout force (Fig. 2.4A, F-G) and enabling mussels to jettison their byssus without damaging the tissue within (Fig. S2.1) (30).

Consistent with this hypothesis, it has been shown that cilia on the epithelial lining of Mytilus edulis foot and gill tissue are regulated by dopaminergic and serotonergic nerves, with serotonin having an excitatory effect and dopamine having an inhibitory effect on ciliary beating (28, 29). Thus, it is reasonable to posit that serotonergic and dopaminergic nerve fibers in the generator comprise a complex feedback system for regulating biointerface strength and release. As support, induced pullout experiments (Fig. S2.4, Movies S2.2 and S2.3) may indicate the presence of a mechanosensory pathway, while it was previously shown that heat stress treatments increased serotonin levels in the M. edulis central nervous system (44) and that gill cilia beating rate increases with increasing temperature (45). This is in line with suggestions that mussels in high temperature tide pools will release their byssus in order to relocate (18). We thus hypothesize that mussels may convert sensory information about their environment into a neurochemical signal that is translated into increased cilia beating enabling byssus release and increased mobility, which could enhance mussel survival under unfavorable conditions. Coupled to increased cilia beating, a force applied by the byssus retractor muscles may be sufficient for inducing spontaneous release (14, 16). Without a byssus attachment, mussels can freely pull themselves around by their foot to find a suitable location before putting down a new byssus (14). Indeed, increased mussel mobility has been reported in response to many different environmental factors including high temperature (18), chemical cues from predators (21), wave exposure ⁽¹⁹⁾, and even substrate chemistry ⁽²⁰⁾. This implies a complex sensory system that can translate physical, chemical, and mechanical stimuli into specific neurochemical signals in the generator. While the cellular mechanism by which this is mediated is still being elucidated, we demonstrate here that the Mytilid byssus stem root provides an example of an effective quick-release mechanism for interfacing living tissues with non-living materials that is not found in human technology.

2.4. Acknowledgements

We thank the staff at FEMR (McGill) for their support in imaging, the staff at Helmotz Zentrum Berlin including H. Markötter at the BAM beamline for support with PCE-mCT, and T. van de Ven for use of the tensile tester. We thank H. F. Hollinger and J. H. Waite for helpful discussion. Funding: Natural Sciences and Engineering Research Council of Canada, NSERC Discovery Grant RGPIN-2018-05243 (M.J.H.), Canada Research Chair award, CRC Tier 2 950- 231953 (M.J.H.), Max Planck Society (F.J.), FQRNT Quebec Merit Fellowship for Foreign Students (L.Y., T.P.). Author contributions: Conceptualization: J.S., L.Y., T.P., M.J.H. Methodology: J.S., L.Y., T.P., P.Z., F.J. Investigation: J.S., L.Y., T.P., S.M., D.E., P.Z., F.J. Visualization: J.S., L.Y., T.P., P.Z., F.J. Funding acquisition: L.Y., T.P., M.J.H. Project administration: M.J.H. Supervision: M.J.H. Writing – original draft: J.S., L.Y., M.J.H. Writing – review and editing: All authors Competing interests: The authors declare that they have no competing interests. Data and materials availability: All data are available in the main text or the supplementary materials.

2.5. References and Notes

- 1. Y. Fang *et al.*, Dissecting biological and synthetic soft–hard interfaces for tissue-like systems. *Chem. Rev.* 122, 5233-5276 (2022).
- 2. L.-L. Li, G.-B. Qi, F. Yu, S.-J. Liu, H. Wang, An adaptive biointerface from self-assembled functional peptides for tissue engineering. *Adv. Mater.* 27, 3181-3188 (2015).
- 3. Y. Luo et al., Technology roadmap for flexible sensors. ACS Nano 17, 5211-5295 (2023).
- 4. S. M. Wellman *et al.*, A materials roadmap to functional neural interface design. *Adv. Func. Mater.* 28, 1701269 (2018).
- 5. R. Elnathan *et al.*, Biointerface design for vertical nanoprobes. *Nat. Rev. Mater.* 7, 953-973 (2022).
- 6. M. W. Tibbitt, C. B. Rodell, J. A. Burdick, K. S. Anseth, Progress in material design for biomedical applications. *Proc. Nat. Acad. Sci. U.S.A.* 112, 14444-14451 (2015).
- 7. Z. Liu, M. A. Meyers, Z. Zhang, R. O. Ritchie, Functional gradients and heterogeneities in biological materials: Design principles, functions, and bioinspired applications. *Prog. Mater. Sci.* 88, 467-498 (2017).
- 8. J. H. Waite, H. C. Lichtenegger, G. D. Stucky, P. Hansma, Exploring molecular and mechanical gradients in structural bioscaffolds. *Biochemistry* 43, 7653-7662 (2004).
- 9. T. R. Dunson, R. N. Amatya, S. L. Krueger, Complications and risk factors associated with the removal of norplant implants. *Obstet. Gynecol.* 85, 543-548 (1995).
- 10. H. Y. Yoo *et al.*, Sugary interfaces mitigate contact damage where stiff meets soft. *Nat. Commun.* 7, 11923 (2016).

- 11. J. Choi, E. Hennebert, P. Flammang, D. S. Hwang, A sugar–lectin rich interface between soft tissue and the stiff byssus of atrina pectinata. *Biomater. Sci.* 8, 3751-3759 (2020).
- 12. A. Tamarin, An ultrastructural study of byssus stem formation in mytilus californianus. *J. Morphol.* 145, 151-177 (1975).
- 13. J. H. Waite, M. J. Harrington, Following the thread: Mytilus mussel byssus as an inspired multi-functional biomaterial. *Can. J. Chem.* 100, 197-211 (2021).
- 14. H. A. Price, Structure and formation of the byssus complex in mytilus (mollusca, bivalvia).

 J. Mollusc. Stud. 49, 9-17 (1983).
- 15. M. W. Denny, B. Gaylord, Marine ecomechanics. *Annu. Rev. Mar. Sci.* 2, 89-114 (2010).
- 16. E. Carrington, J. H. Waite, G. Sara, K. P. Sebens, Mussels as a model system for integrative ecomechanics. *Annu. Rev. Mar. Sci.* 7, 443-469 (2015).
- 17. J. H. Waite, C. C. Broomell, Changing environments and structure—property relationships in marine biomaterials. *J. Exp. Biol.* 215, 873-883 (2012).
- 18. E. A. Roberts *et al.*, Resource allocation to a structural biomaterial: Induced production of byssal threads decreases growth of a marine mussel. *Func. Ecol.* 35, 1222-1239 (2021).
- 19. H. L. Hunt, R. E. Scheibling, Movement and wave dislodgment of mussels on a wave-exposed rocky shore. *Veliger* 45, 273-277 (2002).
- 20. J. Choi, S. Lee, K. Ohkawa, D. S. Hwang, Counterplotting the mechanosensing-based fouling mechanism of mussels against fouling. *ACS Nano* 15, 18566-18579 (2021).
- 21. I. M. Côté, E. Jelnikar, Predator-induced clumping behaviour in mussels (mytilus edulis linnaeus). *J. Exp. Mar. Biol. Ecol.* 235, 201-211 (1999).

- 22. J. H. Waite, The formation of mussel byssus: Anatomy of a natural manufacturing process. in *Structure, cellular synthesis and assembly of biopolymers,* S. T. Case, Ed. (Springer, Berlin, Heidelberg, 1992), pp. 27-54.
- 23. F. Jehle *et al.*, Collagen pentablock copolymers form smectic liquid crystals as precursors for mussel byssus fabrication. *ACS Nano* 15, 6829-6838 (2021).
- 24. T. Ishikawa, Axoneme structure from motile cilia. *Cold Spring. Harb. Perspect. Biol.* 9, a028076 (2017).
- 25. L. Youssef, M. Renner-Rao, E. D. Eren, F. Jehle, M. J. Harrington, Fabrication of tunable mechanical gradients by mussels via bottom-up self-assembly of collagenous precursors. *ACS Nano* 17, 2294-2305 (2023).
- 26. T. Priemel *et al.*, Microfluidic-like fabrication of a metal ion-cured bioadhesive by mussels. *Science* 374, 206-211 (2021).
- 27. R. Beiras, J. Widdows, Effect of the neurotransmitters dopamine, serotonin and norepinephrine on the ciliary activity of mussel (mytilus edulis) larvae. *Mar. Biol.* 122, 597-603 (1995).
- 28. G. B. Stefano, E. Aiello, Histofluorescent localization of serotonin and dopamine in the nervous system of *mytilus edulis* (bivalvia). *Biol Bull* 148, 141-156 (1975).
- 29. L. Vitellaro-Zuccarello, S. De Biasi, A. Amadeo, Immunocytochemical demonstration of neurotransmitters in the nerve plexuses of the foot and the anterior byssus retractor muscle of the mussel, mytilus galloprovincialis. *Cell Tiss. Res.* 261, 467-476 (1990).
- 30. S. L. Schor, Serotonin and adenosine triphosphate: Synergistic effect on the beat frequency of cilia of mussel gills. *Science* 148, 500-501 (1965).

- 31. R. Francis, C. Lo, Ex vivo method for high resolution imaging of cilia motility in rodent airway epithelia. *JoVE*, e50343 (2013).
- 32. E. L. Aiello, Factors affecting ciliary activity on the gill of the mussel mytilus edulis. *Physiol. Zool*, 33, 120-135 (1960).
- 33. D. Ershov *et al.*, Trackmate 7: Integrating state-of-the-art segmentation algorithms into tracking pipelines. *Nat. Methods* 19, 829-832 (2022).
- 34. K. Jaqaman *et al.*, Robust single-particle tracking in live-cell time-lapse sequences. *Nat. Methods* 5, 695-702 (2008).
- 35. M. Lima-Maximino *et al.*, Phasic and tonic serotonin modulate alarm reactions and post-exposure behavior in zebrafish. *J. Neurochem.* 153, 495-509 (2020).
- 36. J. R. Staunton, W. Y. So, C. D. Paul, K. Tanner, High-frequency microrheology in 3d reveals mismatch between cytoskeletal and extracellular matrix mechanics. *Proc. Nat. Acad. Sci. U.S.A.* 116, 14448-14455 (2019).
- 37. D. A. Hoey, M. E. Downs, C. R. Jacobs, The mechanics of the primary cilium: An intricate structure with complex function. *J. Biomech.* 45, 17-26 (2012).
- 38. E. Bell, J. Gosline, Mechanical design of mussel byssus: Material yield enhances attachment strength. *J. Exp. Biol.* 199, 1005-1017 (1996).
- 39. E. C. Bell, J. M. Gosline, Strategies for life in flow: Tenacity, morphometry, and probability of dislodgment of two mytilus species. *Mar. Ecol. Prog. Ser.* 159, 197-208 (1997).
- 40. Y. Tian *et al.*, Adhesion and friction in gecko toe attachment and detachment. *Proc. Nat. Acad. Sci. U.S.A.* 103, 19320-19325 (2006).

- 41. S. Singla *et al.*, Direct evidence of acid-base interactions in gecko adhesion. *Sci. Advances* 7, eabd9410 (2021).
- 42. G. Huber *et al.*, Evidence for capillarity contributions to gecko adhesion from single spatula nanomechanical measurements. *Proc. Nat. Acad. Sci. U.S.A.* 102, 16293-16296 (2005).
- 43. H. Alarcón *et al.*, Self-amplification of solid friction in interleaved assemblies. *Phys. Rev. Lett.* 116, 015502 (2016).
- 44. G. B. Stefano, L. Hiripi, E. J. Catapane, The effects of short and long term temperature stress on serotonin, dopamine and norepinephrine concentrations in molluscan ganglia. *J. Therm. Biol.* 3, 79-83 (1978).
- 45. G. B. Stefano, E. J. Catapane, J. M. Stefano, Temperature dependent ciliary rhythmicity in mytilus edulis and the effects of monoaminergic agents on its manifestation. *Biol Bull* 153, 618-629 (1977).

2.6. **Supplementary Material**

Materials and Methods

Materials

Blue mussels (*Mytilus edulis*) were purchased and maintained at approximately 14 °C in an aquarium with artificial seawater (Fluval Sea, USA; containing Ca, K, Mg, and Sr) adjusted to 3%. Investigations were performed on the foot organ and byssus of adult mussels (shell size 5-7 cm). We have complied with all relevant ethical regulations for testing and research of *Mytilus edulis* in Canada.

Mechanical Testing

Mussels of 5-7 cm in length were opened after cutting the posterior and anterior adductor muscles with a scalpel in order to tie a nylon line around the base of the stem where it is embedded in the tissue. Next, the mussel was wrapped with a sheet of flexible plastic with a hole at the top to allow the nylon line to pass through (Fig. S2.2). Using an Instron mechanical tester (model number MN44- Standard), the two ends of the plastic sheet surrounding the mussels were gripped by the bottom clamp, and the nylon line was gripped by the upper clamp. For testing, the nylon line was pulled by the upper clamp at a rate of 5 mm/min until the force dropped to zero, indicating byssus pullout. From these tests, force (N) versus displacement (mm) values were acquired by the Bluehill 2 software (version 2.18) and plotted. Mechanical tests under each different treatment condition described below were repeated on at least 5 individual mussels.

Mechanical testing, as described above, was performed on native mussels acclimated in our tanks at ~14°C. Additionally, to examine the effect of neurotransmitters on stem release, the maximum force was recorded under each of the following conditions: 1) water injection control; 2) serotonin (serotonin hydrochloride, Sigma-Aldrich) with increasing concentrations (0.005 mM, 0.05 mM, 0.2 mM); 3) metergoline, a 5-HT receptor antagonist (Abcam Inc) 0.02 mM; and 4) dopamine (dopamine hydrochloride, Sigma-Aldrich) with increasing concentrations (0.0001 mM, 0.007 mM, 0.07 mM, 0.2 mM). In each case, injection of 0.5 ml of the relevant solution was performed using a syringe with a fine needle, which was used to inject the solution into the gap between the stem and the generator tissue, careful not to damage the tissue. The needle was only inserted one millimeter deep into the gap. In some samples, stem root damage following byssus removal was further analyzed by dissecting the generator following mechanical testing,

freezing it immediately at -80 °C, and cryotoming it into 5 μ m sections using a cryostat (Leica CM1520) at -23 °C before performing histological staining (following the protocol described below).

In a separate set of mechanical pulling experiments following a protocol recommended by Prof. J.H. Waite (University of California, Santa Barbara), we manually induced the clean release of intact, undamaged stem roots through the application of a sustained subcritical force below the breaking force of the stem. In these experiments (examples of which appear in Movies S2.2 and S3), native mussels with a byssus were removed from the aquarium, and the threads were twisted together into a bundle that would be easy to grip. Using a pair of needle-nosed pliers, the thread bundle was gripped right where they emerge from the shell. The pliers were then turned, wrapping the threads around the tip, generating a force on the byssus that could be gradually increased by further turning the pliers. We observed that different mussels required different critical forces to induce clean byssus release. Thus, an example experiment involved slightly turning the pliers to increase the force and then waiting for approximately 10-20 seconds, and if the byssus was not released in that period, turning the pliers a bit more and again waiting. Eventually, in numerous mussels, a force was reached under which the stem root would slide out undamaged (Fig. S2.4, Movie S2.2 and S2.3). We observed that stem root failure occurred if the interval of plier turning was too large or too rapid – thus, it was important to increase the applied force only gradually in a stepwise fashion.

Phase-contrast Enhanced Microcomputed Tomography (PCE-µCT):

The 3D structure of the byssus stem was imaged using phase contrast-enhanced micro-CT (PCE- μ CT). The byssus stem and the associated generator tissue were dissected away, fixed in 4% PFA

overnight, stained in Lugol's solution, and stored in 70% ethanol until imaging (N=2 specimens). The samples were mounted upright, and scans were collected on the BAMline imaging beamline of the Berlin electron storage ring company synchrotron facility (BESSY II, HZB Helmholtz Center Berlin for Materials and Energy, Berlin, Germany). The samples were scanned in a phase-contrast imaging mode with a sample-detector distance of 100 mm using the double multilayer monochromator centered at 25 keV. Tomographic datasets with a pixel resolution of 1.45 µm were obtained by rotating the samples by 180° and obtaining 3500 radiographs with 100 ms exposures. Following normalization, the datasets were reconstructed using a filter-back projection algorithm, cropped, and converted to 8-bit for further processing as follows. 3D visualization of the generator was obtained by segmentation and deep learning algorithms in DragonFly 2022.2.0.1399. A few images were selected throughout the stack for the deep learning algorithm to identify the lamellae of the generator by highlighting this region using the painter tool. These selected images were inserted into the semantic segmentation model with a class count of 2 and an input count of 1. The model was re-trained multiple times until it recognized the lamellae accurately. The trained model was applied to the whole stack, highlighting all the lamellae in the images. The movie was created using the DragonFly moviemaker tool.

Histological Analysis

For histological analysis, byssus and generator tissue were dissected from the mussel and frozen using liquid nitrogen in a mold containing a frozen section medium (Neg 50). In some cases, the region of the byssus outside the foot was cut away from the generator tissue prior to dissection. The frozen block was sectioned into 5 μ m sections using a cryostat (Leica CM1520). For Masson's Trichrome staining, sections were stained following the manufacturer's protocol (Thermo Fisher

Scientific). Cryotomed sections were first fixed in Bouin's solution overnight and then washed using distilled water for 5 minutes. The fixed sections were stained using Weigert's Iron Hematoxylin solution for 10 minutes and washed again in distilled water. Afterwards, the sections were submerged for 5 minutes in a solution of phosphomolybdic-phosphotungstic acid. Immediately after, these sections were stained with aniline blue solution for 5 minutes and washed using 1% acetic acid for 2 minutes. For Sirius red staining, 5 µm thick cryo-sections were fixed overnight in Bouin's solution, washed with distilled water for 5 minutes, and subsequently stained using a 0.1% picosirius Red solution in saturated Picric acid for 1 hour and washed twice in 1% acetic acid. Stained samples were imaged with a light microscope (Axio Scope.A1, Zeiss) equipped with a 6-megapixel CCD camera (Axiocam 505 color, Zeiss). More than 100 histological images were collected from more than 5 different mussel specimens.

Chemical Fixation and Embedding for Electron Microscopy

Following an existing protocol ⁽²³⁾, the generator tissue was dissected from the mussel, and excess water was removed by dabbing with Kimwipes. The sample was prefixed for 30 minutes at 4°C in a solution of 3% glutaraldehyde, 1.5% paraformaldehyde, and 0.1 M cacodylate pH 7.2 buffer. After pre-fixation, the generator was cut into thin slices using a scalpel and fixed again in the solution described above for 2 hours at 4°C. The fixed sections were rinsed 5 times using the cacodylate buffer at 4°C and then stained using 1% OsO4 for 1 hour at 4°C. Afterwards, the stained sections were rinsed again 3 times for 5 minutes each using the same solution as before and then were dehydrated stepwise in different concentrations of acetone (50%, 70%, 90%, and 3×100%) for a total of 1 hour. The dehydrated samples were then embedded in Epoxy (Epon 812 substitute Sigma-Aldrich, no. 45359) and polymerized at 70°C for approximately 2 days. Ultrathin

sections of 100 nm were prepared for TEM investigations using an ultramicrotome and mounted on carbon-coated Cu grids (200 mesh).

FIB-SEM Measurements and Data Processing

Following an existing protocol (23), the blocks containing generator samples (N = 2) were first polished to expose the tissue at the block surface. These polished blocks were transferred to the Zeiss Crossbeam 540 (Carl Zeiss Microscopy GmbH, Germany), where a trench was milled into the sample surface using a current of 30 nA FIB at 30 kV acceleration voltage (for SEM imaging) and then polished using the 700 pA FIB probe at 30 kV. A FIB milling of 1.5 nA and 30 kV was used to remove thin slices of samples in a serial manner with a slice thickness of 20 nm. After each milling step, the sample was imaged by SEM using the secondary and backscattered electron detector. The image resolution was 2048 x 1536 pixels with a lateral image pixel size of 20.61 nm. The images in the FIB-SEM dataset were processed with the Dragonfly 4.1 software. Images were first aligned using SSD (sum of square differences), and the alignment was corrected manually afterward. The images in the stack were then filtered with the convolution operation in 3D (size 3), and finally, the contrast was enhanced using the contrast-limited adaptive histogram equalization (CLAHE) operation with a kernel size of 100 and 256 bins. 3D visualization of the generator was obtained by segmentation and deep learning algorithms in the Dragonfly 4.1 software. We collected 5 different FIB-SEM datasets from the generator tissue acquired from 2 mussel specimens.

Scanning Transmission Electron Microscopy

To determine the structural motifs of generator tissue at the nanoscale, scanning transmission electron microscopy (STEM) measurements were performed on ultrathin (100 nm) sections of

tissue samples using a Thermo Scientific Talos F200X G2 S/TEM equipped with a Ceta 16 M CMOS Camera, operated at 200 kV acceleration voltage. STEM mode was used for high-angle annular dark-field imaging at magnifications of 16500×, 46000×, 66000×, 130000×, and 185000×. More than 100 images were acquired from generator tissues, with many different TEM sections acquired from two different mussel specimens.

Confocal Raman Spectroscopy

For Raman spectroscopy, generator samples were cryo-sectioned into 5 µm-thick sections and mounted on glass slides. Raman spectra were collected using a confocal Raman microscope (Alpha 4 300R, WITec, Germany) equipped with a green laser (532 nm). The laser power (5 mW) was focused using a 100x objective (Zeiss, numerical aperture [NA] = 0.9), and the scattered light was collected with a thermoelectrically cooled CCD detector behind a 600-g/mm grating. To obtain large-area scans, the TrueSurface mode of the instrument was used with an integration time of 5 s per pixel. WITec's ControlFIVE was used for data collection, and the ProjectFIVE software processed the Raman spectra. We acquired more than 10 different Raman images from generator tissue from 5 different mussel specimens.

Regulation of Ciliary Activity

To investigate the dependence of cilia movement in the generator on treatment with serotonin, the mussel generator tissue was dissected into thin slices of approximately ~0.1mm using a fresh scalpel. Slices from different areas of the generator, starting from the stem base until the region where the generator is connected to the byssus retractor muscles, were mounted on a cell culture plate and then visualized under an inverted microscope (Axio Observer, Zeiss) equipped with a high-speed camera (Axiocam 705 mono, Zeiss) in the differential image contrast (DIC)

mode using a 100x-oil objective. After moving in the axial plane to search for the wavy features associated with the lamellar region, the focal plane was adjusted until beating cilia, which had their tips facing toward the objective, were detected. However, after each solution treatment, the focus had to be re-adjusted since the addition of small amounts of liquid would distort the focus of the image.

Video Acquisition and Ciliary Movement Analysis

Four videos (N = 3 samples from 3 specimens) were acquired sequentially from the same region from each sample: 1) in the native state; 2) after the addition of 0.2 mM serotonin; 3) after the addition of 0.02 mM of metergoline; and 4) after a second addition of 0.2 mM serotonin. In treatments 2 - 4, approximately 100 μ l of the respective solution was added directly to the tissue section. Changes in ciliary movement were observed and recorded in the same region after ~1-2 minutes from the addition of the solution.

In order to determine the velocity of the cilia movement, the TrackMate plugin in FIJI was used $^{(33,\ 34)}$ (Fig. S2.7). The bright circular cilia tips were detected by the LoG detector of TrackMate with parameters for the blob diameter of 1 μ m and a threshold of 0.2. Afterwards, the Simple LAP tracker was used with a linking max distance, gap-closing max distance, and max frame gap of 0.2 μ m, 0.2 μ m, and 2, respectively. Tracks with a displacement of at least 1.5 μ m were used for speed analysis of TrackMate, and the mean speed distribution in μ m/ms was plotted in the form of boxplots, where the box represents the first and third quartiles and the whiskers the minimum and maximum of the data (Fig. 2.4C, Fig. S2.8). The median and mean are represented by the line and point within the box, respectively. Outliers are plotted as individual points. LoG is the Laplacian of Gaussian particle detection, which is the best detector for Gaussian-like particles

in the presence of noise. LAP is the Linear Assignment Problem tracker, which in TrackMate is implemented following a stripped-down version of the method developed by Jaqaman and colleagues ⁽³⁴⁾. For each movie, we detected and tracked between 16 and 570 cilia.

Supplementary Text

Estimation of Forces at the Lamella-Cilia Interface

To estimate the magnitude of the forces present at the interface between the cilia on the septa epithelial surface and the stem lamella, we first estimated the total surface area of the lamellar surface based on our PCE-µCT and histological analyses. We observed that the cylindrical external stem divides into approximately 45 individual lamellar sheets that are interdigitated with the septae as it enters the generator region of the foot. The surface area of a single side of a lamellar sheet was estimated using ImageJ to be approximately 0.045 cm². Considering that there are two sides to each lamella and approximately 45 lamellae per generator, we estimate a total interfacial area of 4.1 cm², which is quite large considering that the volume of the generator is on the scale of 0.008 cm³. This is a slight overestimate because the sheets near the edges are somewhat smaller than those in the center. Nonetheless, this large interfacial area (relatively speaking) arises from branching and interdigitation of the stem and is also slightly underestimated given the wavy structure of the lamellar sheet that can be observed in both PCE-µCT and histological sectioning (perhaps helping balance the overestimation of average sheet area). Given a maximum force to failure of the interface of approximately 20 N observed in the present study (under the effect of dopamine injection), we can convert this to an ultimate stress of approximately 50 kPa based on the estimated interfacial area between lamellae and cilia. This is a comparatively low stress considering that the stress on the proximal regions of a single byssal

thread (the weak point of the thread) under a force of 20 N would be approximately 700 MPa (based on the average measured cross-sectional area measured at 30,000 μ m²), which is considerably higher than the strength of the proximal thread measured previously at ~30 MPa (38). A single byssus will typically have at least 50 threads attached to the stem, so these stresses might, under normal circumstances, balance out. Notably, previous studies, in which two species of Mytilid mussels were experimentally dislodged, indicated that failure of the byssus most commonly occurs at the substrate (~60%), but can also occur less commonly in threads and at the root – the likelihood of which depends on whether the mussel was part of a mussel bed or was a solitary mussel (39). This might make sense evolutionarily considering that if failure occurs at the substrate, a mussel can just make a new byssus, but if failure occurs within the living generator tissue, this would likely be catastrophic for the survival of the mussel. However, it is important to note that byssus production is an extremely energy-intensive undertaking that can divert resources from other important life functions (18). Thus, mussels would benefit from retaining their byssus for as long as possible.

In addition to considering the total stress on the lamellar-cilia interface, we can also consider the forces that a single cilium at the surface might experience assuming an even distribution of forces over the entire interfacial area, considering that stem loading (e.g., from a crashing wave) is approximately parallel to the interface. Based on STEM imaging, we determined a diameter of a single cilium of approximately 0.3 μ m (consistent with literature reports of motile cilia (24)). If we assume that the entire surface area of all lamellae comprising the stem root is carpeted with cilia, then it would mean that there are approximately 5.7 billion motile cilia in contact over the entire generator-stem biointerface. If we assume that the maximal applied force of 20 N is spread

evenly over these billions of cilia, then each cilium would only experience a force of approximately 3.5 nN. This force is in the same range as the maximal frictional adhesive forces achieved by single toe pad hairs (spatula) during gecko adhesion (2 – 15 nN). Notably, each hair has a width at the tip that is extremely similar to that of a single cilium (\sim 0.2 – 0.3 μ m) (40). Considering that gecko adhesion is primarily mediated through van der Waals interactions applied frictionally between the spatula tips and surfaces, we posit that the interaction between cilia and lamella surfaces is based on a similar mechanism of many weak interactions loaded together.

Low Force Failure with High Dopamine

Injection of the neurotransmitters serotonin and dopamine showed a clear dose-dependent effect that decreased or increased the maximum pull-out force, respectively (Fig. 2.4A, Fig. S2.3). This was attributed to the influence of serotonin to increase and dopamine to decrease cilia movement. However, at very high concentrations of dopamine, we observed an unexpected and dramatic decrease in pullout forces by an order of magnitude. On closer examination, we observed that the failure was not due to pulling out of the lamellae, but rather to failure and tearing of the entire generator, likely at the interface between the generator and the byssus retractor muscles.

We hypothesize that failure at this interface under conditions when cilia are completely immobilized through the addition of high dopamine concentrations indicates that the ability of cilia to move under normal conditions might constitute a toughening mechanism that dissipates mechanical energy. We propose that under normal conditions, higher forces can be achieved because the forces are not transmitted deeper into the tissue to this presumably weak interface

because ciliary movement contains the stress field within the generator region. In other words, a small amount of cilia movement may be advantageous for dissipating some of the mechanical work applied, preventing forces from reaching the weak interface at the base of the generator. However, when the cilia are completely immobilized, forces are more easily transmitted deeper into the tissue and able to concentrate at this weak interface, leading to fracture and failure at lower applied force. Thus, this toughening mechanism might function to protect the weak interface between the generator and the underlying musculature. However, further investigations are required to assess this possibility.

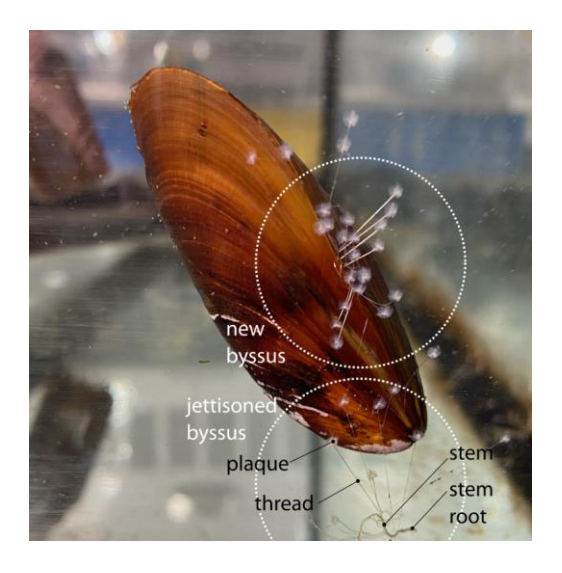


Figure S 2-1. Anatomy of a jettisoned byssus. It is well documented that mussels can jettison their entire byssus on demand. In this photograph, a mussel (Mytilus edulis) "climbed" a vertical surface in the aquarium by releasing its old byssus and fabricating a new one. To jettison a byssus, the mussel releases the entire stem (which is attached to the surface via the threads and plaque) by disengaging the soft tissue in the generator region of the foot from the stem root.

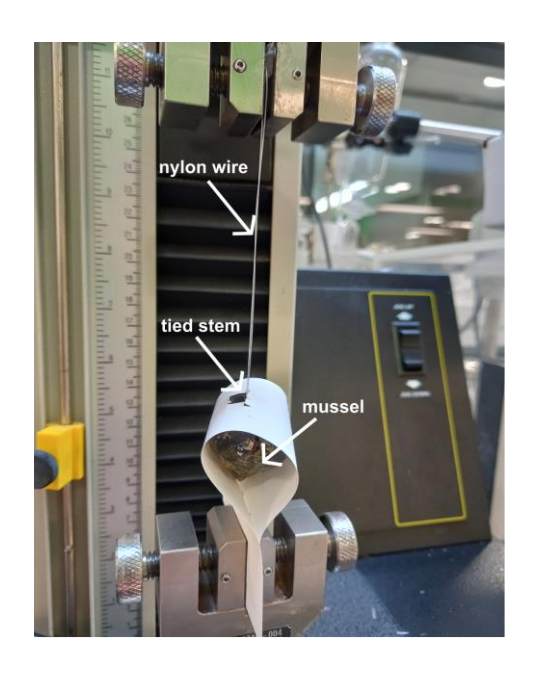


Figure S 2-2. Mechanical testing setup for forced byssus pullout studies To record maximum pullout force of the stem root, the mussel was opened, and a nylon fishing line was tied tightly around the base of the stem. The mussels were then enclosed within a folded plastic sheet held firmly in the grips of a tensile tester with a hole cut in the sheet to allow the nylon line through, which was then fixed in the upper grip.

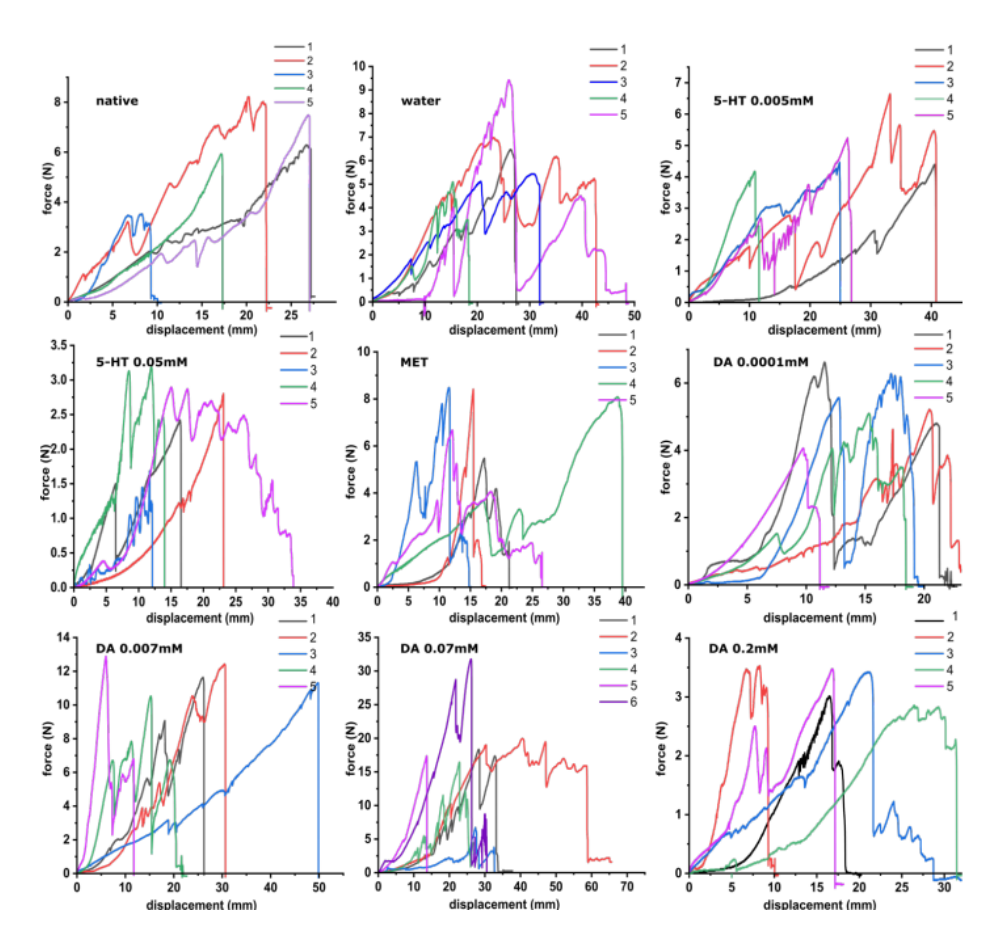


Figure S 2-3. Mechanical testing plots of forced stem release under different conditions Mussels were tested in their native state and after the injection of water, different concentrations of the neurotransmitters serotonin (5-HT) and dopamine (DA), as well as Metergoline (MET), a nonspecific serotonin receptor antagonist. For each treatment, we calculated the mean and standard deviation of the maximum force extracted from each sample and then plotted these data in the bar graph in Fig. 2.4A.

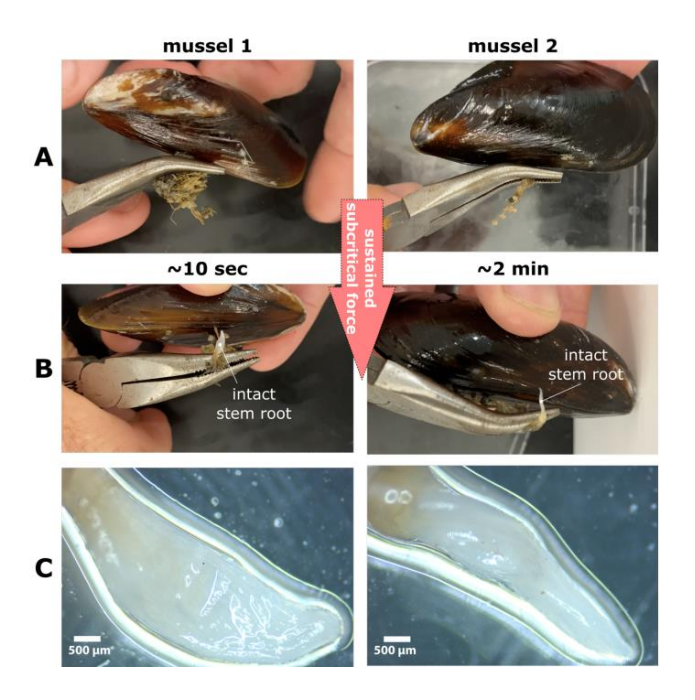


Figure S 2-4.Mechanically induced byssus release. Examples of two mussels that exhibited mechanically induced byssus release. A) Mechanically induced byssus release was achieved by gripping byssal threads with needle-nosed pliers and gradually turning the pliers stepwise to wrap the threads around the tips of the pliers. This creates a sustained force acting on the byssus that could be increased slowly over time. B) In numerous mussels, a force was reached, below the breaking force of the stem root, at which the mussel would release the intact stem root without obvious signs of damage. Interestingly, some mussels released their byssus following application of low force for a short duration (< 30 s; Video S2), while others required higher relative forces for longer duration (2 min or more; Video S3), suggesting that individual mussels may have different thresholds before release. C) Higher magnification image of the cleanly released stem

roots from mussels 1 and 2 from row (B) made with a dissecting microscope showing intact smooth structure.

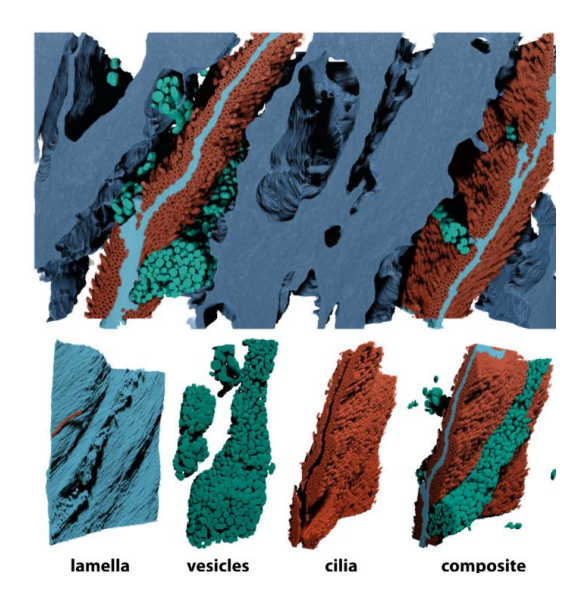


Figure S 2-5.FIB-SEM reconstruction of the generator-stem biointerface. 3D reconstructed FIB-SEM images stack from Fig. 2.2B showing the detailed structure of the lamella, vesicles, and cilia. A single cilium is included in the lamella image to demonstrate the intimate contact and also to highlight that the grooved structure of the lamellar surface arises from indentions from the cilia pressing into the surface, suggesting that the outer layer of the lamellae is relatively soft. The vesicles are lined up ready to create new lamellar material as needed.

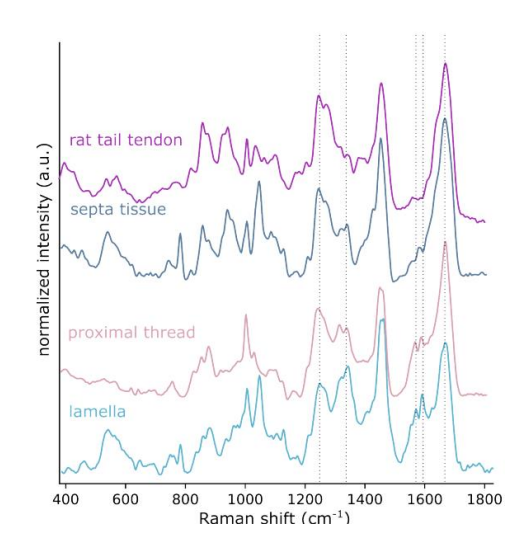


Figure S 2-6.Comparative Raman spectra from stem and generator compared to the proximal byssal thread and tendon. Raman spectral comparison suggests compositional and conformational similarities between the lamella and the proximal thread and between the septa ECM and rat tail tendon (RTT; type I collagen), respectively. In particular, peaks at ~1600 and 1580 cm⁻¹ in the lamella and proximal threads are distinctive suggesting a common, noncollagenous and aromatic-rich component. However, lamella appear to show more unstructured protein conformation based on differences in the amide III band (1200 – 1380 cm⁻¹). In contrast, both RTT and the septa ECM spectra show a high degree of triple helical order based on strong peak at ~1250 cm⁻¹ in the amide III band, suggesting a high content of type I collagen.

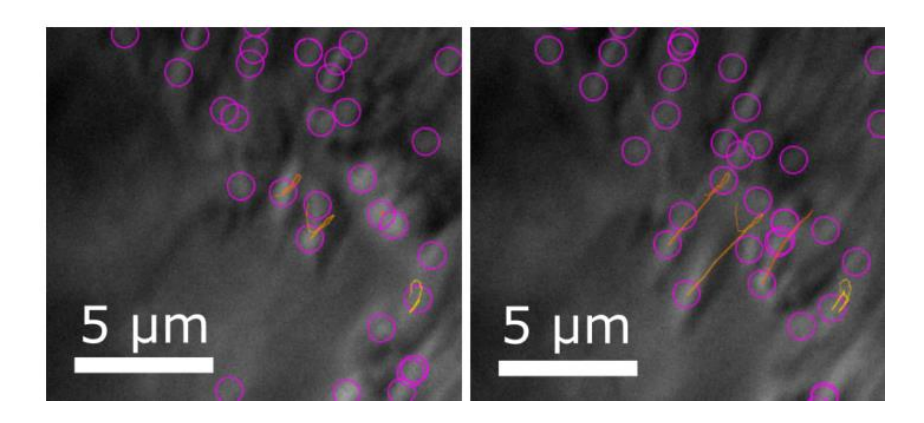


Figure S 2-7 .Tracking cilia movements. Subsequent still images from a video of generator cilia beating taken with an inverted light microscope in DIC imaging mode. Using ImageJ, cilia ends were detected by the LoG detector (pink circles), and their movement was followed with Simple LAP Tracker (orange lines). From these analyses, mean cilia speeds were determined.

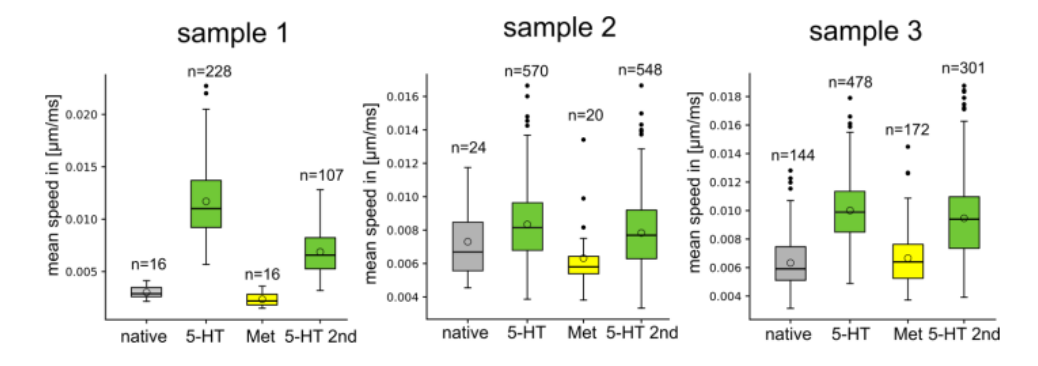


Figure S 2-8. Generator cilia beating speed as a function of consecutive treatment with serotonin and metergoline. Mean cilia beating speed measured from generator tissue dissected from three different individual mussels when freshly dissected (native), following addition of serotonin (5-HT), following subsequent addition of metergoline (MET – a serotonin receptor antagonist), and following a subsequent second addition of serotonin (5-HT 2nd). Tissue sections were imaged with an inverted light microscope in DIC mode. Cilia movements were detected and tracked using imageJ with LoG and simple LAP Tracker plugins as described in Supporting Figure S2.7. Number (N) of cilia detected and tracked in each treatment is indicated on the plot. Data show two trends

very clearly in all three samples. 1) The number of tracked cilia detected by the software is substantially higher following both the first and second serotonin treatments. This is highly relevant considering that the same general region of tissue was imaged in each treatment. Thus, this indicates that more cilia are beating in the tissues following the serotonin treatments. 2) The mean beating speeds of the cilia are increased following the serotonin treatments in all three samples. Taken together, we interpret these observations to indicate that cilia beating in the generator is under neurochemical control with serotonin promoting increased cilia beating. This is consistent with our finding that serotonin injection into the generator lowers the force required to release the stem root.

Movie S2.1. 3D reconstruction of PCE-μCT dataset. This movie was generated from reconstruction of PCE-μCT dataset acquired from a fixed mussel generator and stem root stained with Lugol's solution. Initially, the generator and septa tissues are visualized in grayscale, while the stem root lamellae are visualized in light blue. Moving from the external stem region into the stem root, one can see the complex interdigitation of the septae and lamellae. Later in the movie, the generator tissue is removed from the model in order to more clearly visualize the complex structure of the wavy lamellar sheets.

Movie S2.2. Induced removal of the stem – short force application. This movie shows the case in which the mussel is mechanically induced to cleanly release its byssus through application of a sustained subcritical force applied by twisting the byssus around a pair of needle-nosed pliers. In this case, the mussel released the intact stem root after only ~10 seconds of force application.

Movie S2.3. Induced removal of the stem – long force application. This movie shows the case in

which the mussel is mechanically induced to cleanly release its byssus through application of a

sustained subcritical force applied by twisting the byssus around a pair of needle-nosed pliers. In this case, the mussel released the intact stem root after around 2 minutes of force application.

Movie S2.4. 3D reconstruction of FIB-SEM dataset. This movie was generated from reconstruction of FIB-SEM images acquired from a fixed, osmium-stained generator with stem root embedded. Relevant structures such as the lamellae (light blue), cilia (red), vesicles (teal) and septae (blue) were reconstructed, segmented, and rendered into 3D objects. Initially, the movie shows the colorized image stack from the FIB-SEM, and then later visualizes the reconstruction zooming in on specific features visualizing the interdigitation of the lamellae and the septae, showing the intimate contact of the lamellar surface with the motile cilia.

Movie S2.5. Manual removal of the stem following injection of serotonin. This movie shows the case in which the stem root is released with almost no resistance following injection of serotonin into the gap where the stem enters the generator tissue. In this case, the mussel was opened, injected with serotonin, and a force was applied by hand. The stem root slips out easily and cleanly revealing an undamaged, smooth, and tapered morphology.

Movie S2.6. In situ response of cilia in the generator to serotonin. This movie shows that the beating speed of cilia in dissected generator tissue can be modulated through addition of serotonin and metergoline. The beating was imaged on an inverted microscope in DIC mode. The addition of serotonin to the generator (in the native state) increases ciliary beating speed. After the addition of metergoline, the cilia activity decreases, but it was again increased following the second addition of serotonin.

Chapter 3

3. A dynamic bio-interface in mussels mediated by a mechanoresponsive intermediate filament-based biopolymer

Preface

In the previous chapter, I explored the underlying mechanism behind the release of the byssus stem at the living/non-living bio-interface in the mussel. Our findings highlighted that the neuroregulated beating of cilia, controlled by neurotransmitters such as serotonin and dopamine, plays a critical role in modulating the mechanical strength at these bio-interfaces. However, it remains unclear how the initial activation of this response occurs. Given the direct and intimate contact between the lamella and cilia, I focused this chapter on further investigating the structure and composition of the lamellae surface to gain a deeper understanding of its functional role at the bio-interface. As shown in the previous chapter, the lamellae are biphasic with an unknown noncollagenous component comprising the outer layer in contact with the cilia. Preliminary findings from the MSc thesis work of a previous student in the Harrington research group (J. Sivasundarampillai) showed evidence of an extractable protein from the lamellae predicted to have alpha helical structure, but it was unclear whether this putative protein was actually present in the lamellar material, and if so what function it might serve. Inspired by this initial finding, my work in this chapter aimed at further investigating this putative protein, its structure, and its potential role at the byssus stem biointerface. Utilizing a combination of histological and immunohistological imaging, spectroscopic mapping, X-ray diffraction and electron microscopy, I was able to confirm the presence of this putative protein as a key structural component of the

outer lamellar layer of the byssus stem root, naming it mussel stem protein-1 (MSP-1). Moreover, I identified that MSP-1 is stored and fabricated as an alpha helical coiled coil resembling an intermediate filament, but that it can be mechanically converted into a beta sheet structure, which may play a mechanosensory role. The results presented in this chapter complement the findings of Chapter 2, offering a more comprehensive overview of how both the living (generator) and non-living (stem root) components of the bio-interface act as responsive elements to mechanical forces. The interplay between these two components suggests the existence of that are yet to be fully understood. This lays the foundation for further investigation into the potential signaling pathways and interactions between the mechanical and biochemical responses for adhesion and byssus formation. This chapter is a manuscript in preparation to be submitted shortly.

3.1. Abstract

Mussels fabricate a distinctive biointerface that bridges their non-living biopolymeric byssus (used for anchoring in seashore habitats) with their soft-living tissue. Occurring in a region known as the byssus stem root, this biointerface is at once strong, yet also capable of on-demand release under apparent neurobiological control by the mussel, but this is not well understood. Here, we have identified and sequenced a previously unknown intermediate filament protein (MSP-1) that, based on immunohistochemical staining and spectroscopic mapping, comprises the surface of the stem root in direct contact with billions of motile cilia emerging from the living tissue. Further structural analysis indicates that MSP-1 is secreted as an α -helical coiled coil but is subsequently mechanically converted to a β -sheet conformation. We posit that this mechanoresponsive

conversion has a mechanical function in toughening and strengthening the interface, but possibly also as a mechanosensory mechanism given its intimate contact cilia in the living tissue.

3.2. Introduction

Recent advances in bioimplants, including applications such as brain machine interfaces, joint prostheses, and spinal fixations, aim to seamlessly integrate hard devices with soft biological tissues. [1, 5] This integration is crucial for achieving both biocompatibility and functionality. [1, 6] However, a significant challenge arises from the mismatch between these mechanically distinct materials.^[7] At their interface, stresses concentrate, leading to structural failure that often takes the form of delamination in the contact zone, i.e. detachment of implants from the soft tissues. [7] Further complications may arise when these devices need to be removed or replaced once past their useful lifetime. [8] For instance, if dental implants need to be removed due to complications, such as bone loss and soft tissue recession, [8] the process can trigger soft tissue collapse and lead to swelling and inflammation in the surrounding area. [9] Therefore, future bioimplant designs must consider both biointerface strength as well as the ability to detach safely and effectively without the need for complicated surgeries. Nature offers valuable insights that could guide the development of such advanced biointerfaces.^[7] One prominent design paradigm that has received much attention is the use of functional gradients, which enable stable integration between distinct materials by avoiding stress concentrations through avoiding sharp interfaces. [7] Observed in the mantis shrimp dactyl club, [10] squid beaks, [11] tendon/ligament-to-bone connections^[12] and marine mussel byssus,^[13] these systems avoid stress concentration through

smooth transition in composition and/or structural hierarchy between mechanically distinct regions.

While effective at strengthening potentially weak interfaces, functional gradients do not solve the problem of on-demand release of the interface. In contrast, it was recently discovered that marine mussels (*Mytilus edulis*) have evolved a strong biointerface between living extracellular matrix comprising the soft tissue of the organism and a stiff non-living biopolymeric holdfast known as the byssus, which can be released on-demand by the mussel (Figure 1).^[14] Mussels fabricate their protein-based byssus as a means of securely anchoring to hard substrates in waveswept seashore habitats.^[15] The byssus is comprised of numerous tough and adhesive fibers that converge at the byssus stem like branches attached to a tree trunk (Figure 1).^[15, 16] The stem is anchored securely into the living tissue at its base (the stem root).^[16, 17] Remarkably, however, despite the very strong connection between the stem root and soft tissue, mussels can inexplicably jettison their entire byssus on demand in order to relocate or escape threats (Figure 1a).^[14, 17] This makes the mussel an ideal model system for studying a quick-release living/non-living bio-interface, which offers an exciting model system for inspiring design of easily removable bioimplants. Yet, the mechanism of release is poorly understood.

The stem root consists of over 40 individual sheets, known as lamellae, each with a thickness of 2 to 3 mm and a distinct wavy morphology (Figure 1b).^[16, 17] The lamellae are interdigitated with the living tissue creating a massive interfacial surface area in direct contact with nearly six billion cilia (Figure 1c). Cilia movement, which is regulated neurobiologically with serotonin and

dopamine, was shown to regulate the mechanical strength between the non-living and living tissue, thereby enabling byssus release on demand.^[17] It is hypothesized that stem root release can be activated by a range of environmental factors, including physical, chemical, and mechanical stimuli,^[17] which points to the existence of a sophisticated sensory system that remains poorly understood.

Beyond the cellular pathways in the tissue, the role of the biopolymeric lamellar material of the stem root is also potentially critical, given its location at the juncture of the living and non-living. Notably, it was shown previously^[17, 18] that the lamella is biphasic in composition, consisting of a collagenous inner lamellar layer (ILL), staining positively for Sirius Red, and a non-collagenous outer lamellar layer (OLL), that does not, and which is in direct contact with the cilia (Figure 1c-d).^[18] While the ILL is comprised of byssal collagens similar to those that comprise the core of the byssal threads, the composition of the OLL remains unknown. This poses important questions regarding its potential role, particularly given its position surrounding the collagenous ILL, which is already highly effective at mitigating mechanical stress based on its similarity to the byssal thread collagenous core. Here, we investigated the OLL composition, structure, and function employing a cross-disciplinary approach bridging cell biology, biochemistry, and materials science.

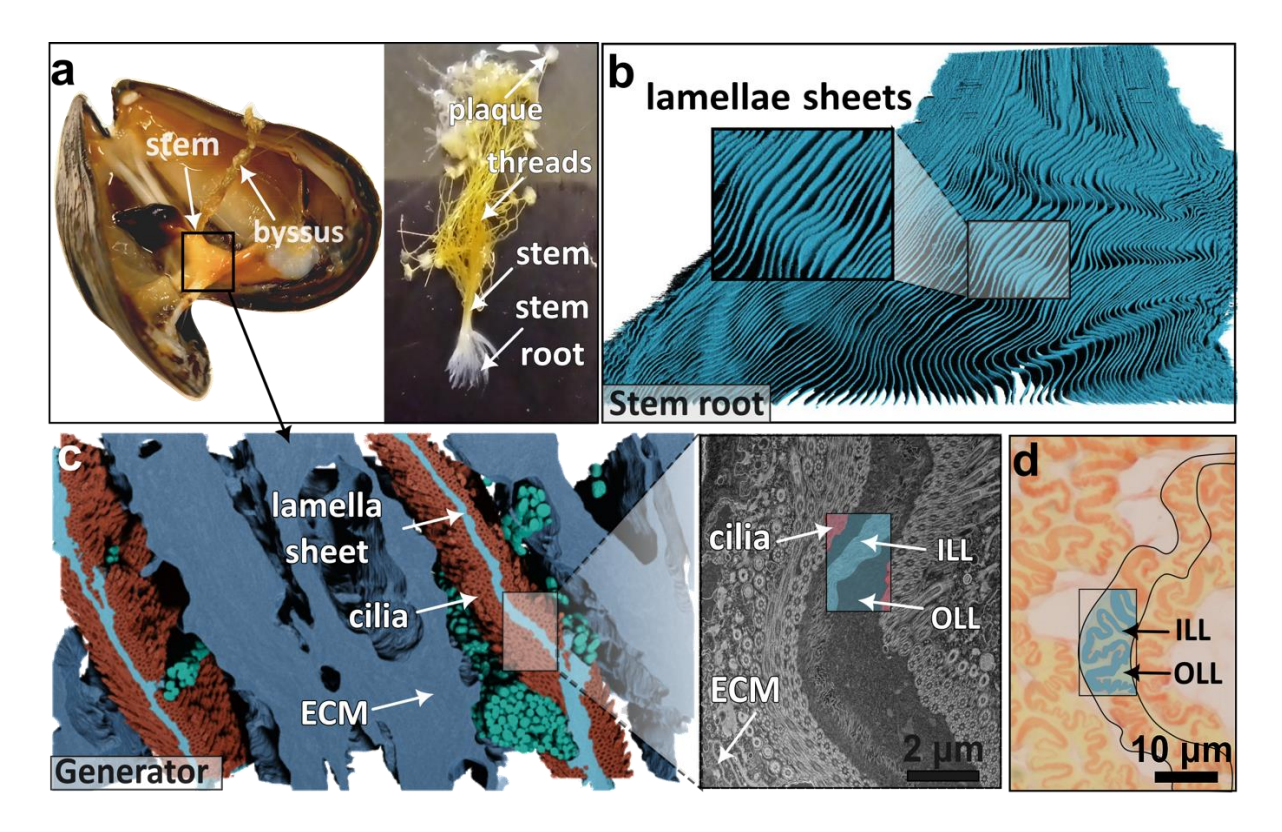


Figure 3.1. Overview of mussel byssus stem root biointerface. (a) An opened mussel with the stem pulled out (right), exposing the stem root that was embedded in the generator tissue. (b) False-colored 3D reconstruction of the PCE-μCT dataset of the lamellae in the generator, showing a zoomed-in image of the lamellar sheets. (c) A reconstructed 3D FIB-SEM image stack shows the structural features present in the generator tissue, highlighted in (a). The image on the right shows a high-magnification STEM image of the biphasic lamella in contact with the cilia, corresponding to the highlighted area in (c). (d) A section of the released stem stained with Sirius red, showing the biphasic composition of collagenous (ILL) and non-collagenous components (OLL) of the lamellae. Panels B-D reproduced with permission from.^[17] Copyright © 2023, American Association for the Advancement of Science (AAAS).

3.3. Results

Protein extraction and analysis

Previous investigations of the byssus stem biointerface from distantly related mussels from the *Atrina* species indicated the presence of a protein bridge between the tissue and byssus based on sugar and metal-binding.^[18] Thus, to better understand the stem biointerface in *Mytilus edulis*, we performed a protein extraction to determine if there might be an analogous interfacial protein (Figure 2). Proteins were extracted from a cleanly released byssus stem root lamellae using 5% acetic acid containing 4 M urea and 2 M thiourea using a tissue grinder resulting in the release of very small quantities of protein requiring silver staining to observe with SDS-PAGE (Figure 2a). Nonetheless, every extract consistently showed the presence of a prominent band running slightly below the 70 kDa MW standard.

To identify the protein, tandem mass spectrometric (MS/MS) proteomic analysis of the extract following digestion with trypsin was blasted against a gland-specific transcriptome from *Mytilus edulis*. The top hit was a 66.9 kDa transcript, which showed 45% coverage by 23 individual tryptic peptides. Importantly, the transcript appears to be almost exclusively expressed in the stem generator gland of the mussel foot and was not prominent in any of the other secretory gland transcriptomes. The complete sequence, which was verified with 3' and 5' rapid amplification of cDNA ends (RACE), is provided in Figure 2e. The protein consists of 584 amino acids, with an elevated molar concentration of serine (10.1 mol%), and combined asparagine and glutamine concentration of 11 mol%, with a notable presence of glutamine doublets.

Although this protein was extracted from the stem material, we could not detect a canonical signal peptide in our 5' RACE data. To further verify that the protein sequence acquired corresponds to the protein extracted from the stem root material, we raised an antibody against two synthetic peptides selected from the protein sequence and performed a Western blot on the extracted protein (Figure 2b). Both antibodies clearly react with the same ~70 kDa band observed with silver staining. This suggests this protein is secreted via a non-canonical pathway. In support of this, 2 paralogs of this protein-coding gene present in the *M. edulis* genome and an ortholog from *M. trossulus* also all lack signal peptides (Figure S1 and S2). Given that the protein was extracted from the stem root, we name it mussel stem protein 1 (MSP-1).

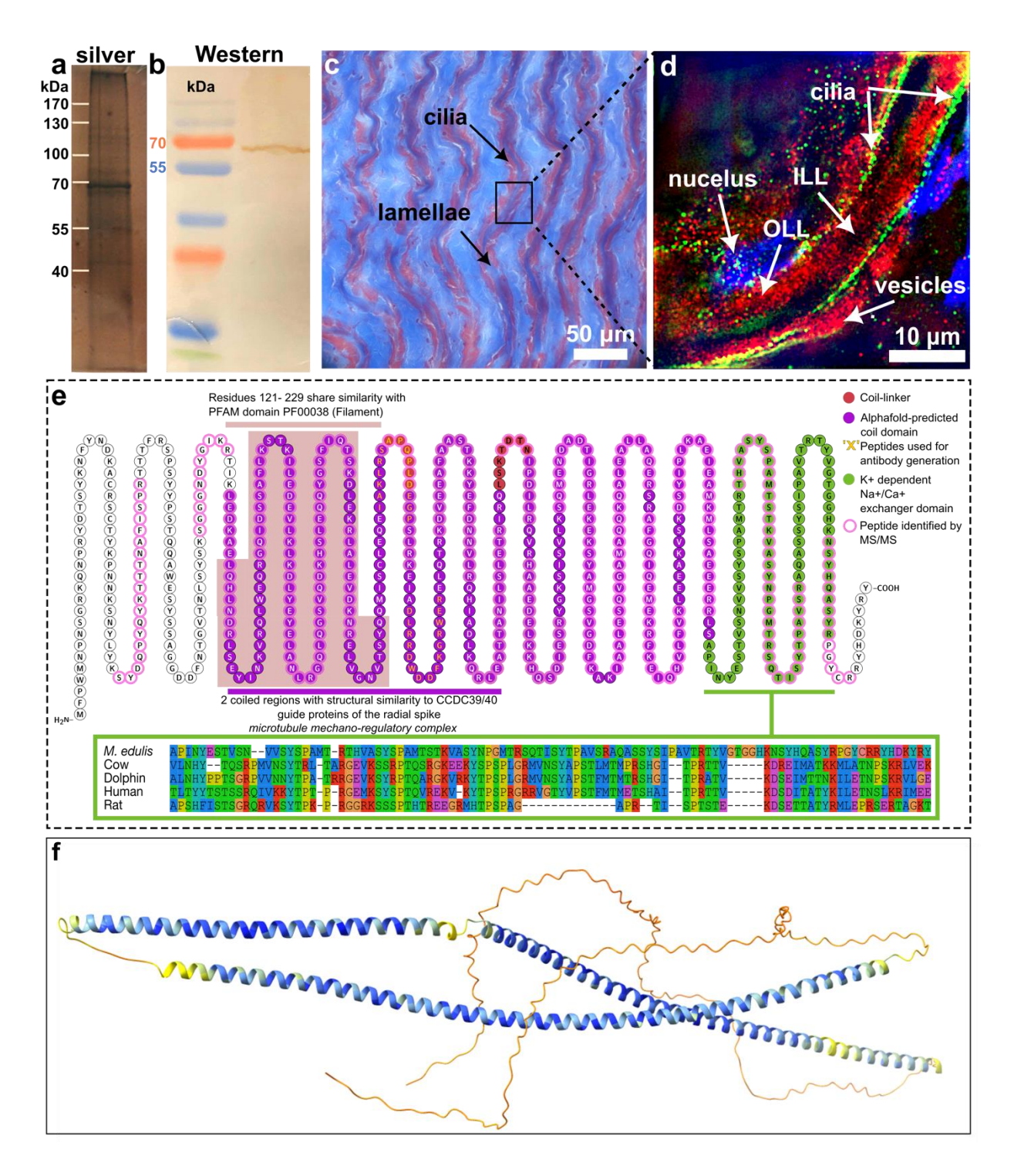


Figure 3.2. Extraction, sequence and localization of mussel stem protein-1 (MSP-1). (a) Silver staining of an SDS-polyacrylamide gel displays the band representing the protein extracted from the stem root lamellae. (b) Western blot of the extracted protein stained in (a) using an antibody

raised against MSP-1 peptide. (c) Trichrome-stained section of the generator in which an unstretched stem root is embedded (blue: collagenous, red: non-collagenous components). (d) Immunostaining fluorescence image collected with SIM of a single stem root lamellar sheet and surrounding tissue; blue: nuclei, green: cilia, red: MSP-1. (e) A schematic of the protein sequence with annotations describing the characteristic features of MSP-1. (f) AlphaFold-predicted conformational structure of MSP-1.

Blasting the MSP-1 sequence against the protein database indicates a very strong similarity to numerous putative proteins with unknown function from a broad range of fresh and saltwater bivalves including other Mytilid mussel species, as well as various scallops and oyster species – suggesting a strong evolutionary conservation (Figure S1 and S2). While there is only weak sequence homology to other proteins with known function, it is worth noting that the C-terminal region shows some similarity to sodium-calcium exchanger (NCX) domains – a transmembrane protein that functions to exchange sodium (Na+) for calcium ions (Ca2+) across the plasma membrane^[19]. Furthermore, a region closer to the N-terminus shows sequence similarity to domain IPR03900 in the InterPro database, an intermediate filament (IF) protein family^[20] – a class of structural coiled-coil (CC) proteins that includes keratins, vimentin, and lamin – a mechanosensory nuclear envelope protein.

In support of this finding, a structural analysis using AlphaFold3 predicts that the protein possesses three alpha helical regions with two small non-helical linker regions between them and longer non-helical domains at both the N- and C-termini, which was further supported by

dedicated bioinformatic coiled-coil (CC) prediction algorithms (Waggawagga)^[21-23]. All algorithms used further predict that MSP-1 will form homodimeric alpha helical CC structure in the central region of the protein (Figure 2f). Notably, these structural features (i.e., three helical CCs divided by non-helical linkers with unstructured termini) are highly characteristic of IF proteins.^[21, 22] Importantly, across this broad class of IF proteins there is relatively low sequence similarity despite the conserved structure. However, searching the AlphaFold3-predicted structure against the VAST protein structural database revealed similarity with certain IF proteins, in particular CCDC39/40 which binds to microtubules in cilia.^[22, 26] This suggests that MSP-1 is an IF-like protein with a homodimeric CC conformation.

Immunochemical localization

Given the proximity of cilia to the stem root lamellae and the finding of structural homology to CCDC39/40, it was essential to verify that MSP-1 was not an extraction artifact from the cilia. To confirm the localization of MSP-1, we used immunohistochemical labelling with structurally illuminated microscopy (SIM) employing an antibody raised against the alpha helical region of MSP-1. Cryo-sections of the native generator tissue were co-stained with the MSP-1 antibody, as well as antibodies for α -tubulin (for staining cilia) and DAPI (for staining cell nuclei) (Figure 2d). Structured illumination microscopy (SIM) of stained generator tissue containing the lamella shows a strong staining of the lamella with the MSP-1 antibody, which is clearly distinct from the surrounding cilia, with nuclei clearly visible on the other side of the cilia (i.e., within the living tissue). Notably, the MSP-1 antibody is largely absent from the central region of the lamellar sheet, which is consistent with the collagenous composition of the stem root ILL determined with

other methods. In addition, positive staining with the MSP-1 antibody is observed in the living septa tissue directly surrounding the lamella, consistent with the previously observed location of the secretory vesicles that are used to make the stem (Figure 1c). Based on these data, we propose that MSP-1 is indeed the precursor that comprises the non-collagenous OLL of the byssus stem root lamellae.

EM characterization of the outer phase and the associated secretory vesicles

To further investigate the non-collagenous OLL and the associated secretory vesicles at higher resolution, we utilized various modes of electron microscopy. Using scanning transmission electron microscopy (STEM), we observed that the outer phase of lamellae exhibits a woven texture of thin fibrils, while the core consists of thicker fibrils that are presumably collagenous in nature based on histological staining and Raman spectroscopy (Figure 3a). [17] The thin fibrils of the OLL are in direct contact with the cilia, molding their structure to the surface, and in many cases appearing to direct their end to be in contact with the cilia (Figure 3b). While it is difficult to make out individual fibrils in the STEM images due to their highly packed organization, the shortest length fibrils at the edges are more than 100 nm, while the diameters appear uniform and in line with other intermediate filament fibers (~10 nm). Overall, the filaments are aligned along the axis of the stem lamellae. STEM imaging also reveals the presence of numerous secretory vesicles located at the periphery of the lamellae (Figure 3c-d). While some vesicles have the rugby ball-like structure of the core vesicles, we observed numerous vesicles with a pill-like structure of the type II vesicles previously identified in the stem generator tissue^[16] showing evidence of fibrillar contents, consistent with the OLL ultrastructure.

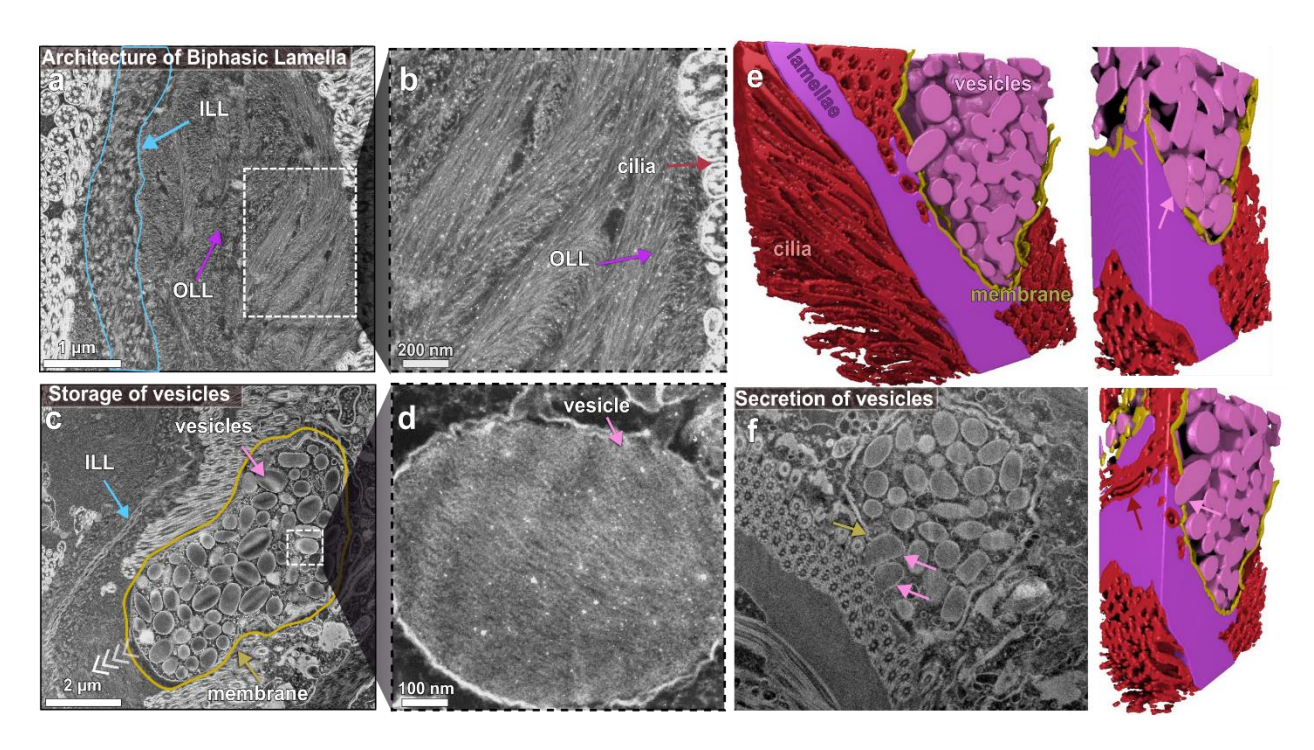


Figure 3.3.Electron microscopic characterization of stem root biointerface (a) STEM image indicating the biphasic nature of the lamella in contact with the cilia. (b) Zoomed-in image of the region highlighted in (a), showing the OLL fibrils reorienting almost parallel to the cilia surface. (c) STEM image showing the concentration of vesicles at the interfaces prior to release. (d) Zoomed-in image from (c) of a single vesicle consisting of IF fibrils. (e) False-colored 3D model reconstructed from FIB-SEM image stack acquired from the generator. The colored arrows indicate the individual components in the 3D model. (f) Image from the FIB-SEM stack showing the fusion of the vesicles (pink arrow) with the membrane (yellow arrow). Focused ion beam scanning electron microscopy (FIB-SEM) is a powerful imaging modality that produces image stacks through micron-scale sample volumes with nanoscale resolution, which can yield 3-dimensional models through segmentation and reconstruction of principal features in the images. FIB-SEM reconstruction of the stem root biointerface also shows the pill-like morphology of the vesicles in 3D (Figure 3e). Moreover, FIB-SEM reconstructions clearly show some vesicles whose

contents are merging with the OLL between the cilia and sometimes, even entrapping the cilia within the newly formed OLL (Figure 3, Movie S1). These data suggest that the MSP-1 secretion process is likely merocrine in nature, in which the vesicles fuse to the membrane and are secreted into the lumen (Figure 3e-f), which is further supported by STEM images (Figure 3c). This is also consistent with images from immunostained samples in which the vesicle contents appear to be secreted between the cilia. Interestingly, several STEM images show locally aligned fibrillar domains within the OLL that are on the same scale as the vesicles (Figure 3d) (1-2 µm), supporting this assembly mechanism. Given this clear evidence that MSP-1 is secreted, the lack of signal peptide on the protein is unusual and suggests an unconventional protein secretion (UPS) pathway that does not involve the traditional transit from the endoplasmic reticulum through the Golgi apparatus. [27] Indeed, several other UPS pathways have been identified previously and consistent with our EM analysis, the IF protein vimentin has been shown in some cases to be secreted extracellularly via Type III UPS through the fusion of vesicles with the plasma membrane to release the protein cargo. [27,28]

Protein conformation in the outer lamellar layer

Our findings suggest that the OLL consists of MSP-1 proteins arranged into fibrils similar in morphology to IFs, which would be expected to have an alpha-helical CC conformation. To further investigate this hypothesis, we characterized protein conformation within the stem lamellae. Wide angle X-ray diffraction (WAXD) of cleanly released stem lamella reveals the presence of several distinct peaks superimposed onto a broad amorphous background peak (Figure 4 a-b). Of particular relevance, we observe a prominent peak at $q = 11.7 \text{ nm}^{-1}$ (d spacing = 0.53 nm) which

corresponds to the pitch of alpha helical secondary structure.^[29] Notably, it is preferentially oriented along the long axis of the stem lamella, consistent with the STEM images that show the filaments in the OLL oriented along the long lamellar axis (Figure 4c). Peaks appearing at lower q values in the direction orthogonal to the stem root axis are consistent with lateral packing of the fibril, ^[30] but given the presence of collagen fibrils, it is not possible to assign these peaks confidently.^[31]

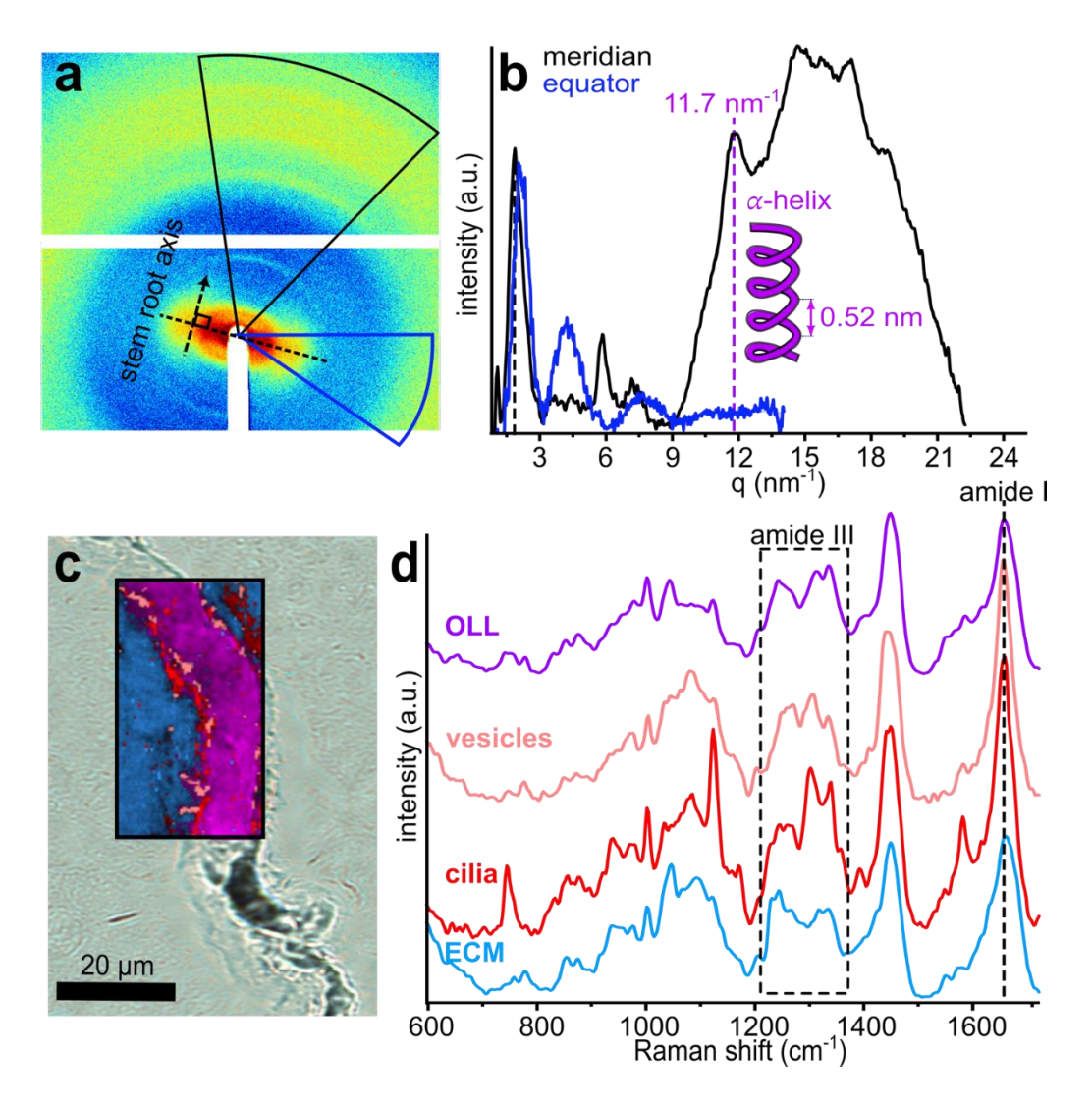


Figure 3.4. Conformational characterization of mussel byssus stem root outer lamellar layer (OLL).

(a) WAXD diffractogram of the stem root. (b) Radial intensity profiles of (a) as a function of the

scattering vector q from the meridional (black) and equatorial (blue) axes with respect to the stem root axis. The illustration shows the alpha helical pitch corresponding to the peak at $q = 11.7 \text{ nm}^{-1}$ (d = 0.53 nm). (c) Raman image map of an unstretched stem root, showing the composition of the identified components in (d).

Confocal Raman spectroscopic mapping investigation of the stem root biointerface shows that the lamella, as well as the secretory vesicles show spectra that are consistent with an alpha helical conformation based on the presence of amide I peak maxima centered around 1655 cm⁻¹ and amide III peak which is higher at 1320 than at 1230 cm⁻¹ (Fig 4c-d). [32, 33] Given the resolution of this method, these spectra likely contain contributions from both the OLL and the ILL, so the fact that the alpha helical features are still evident is compelling. To complement the Raman-based measurements, ATR-FTIR were collected from a stem root that was gently extracted from the generator through serotonin-induced release, which was necessary as the resolution of FTIR microscopy would be insufficient to focus only on the lamella. ATR-FTIR spectra were collected using an evanescent polychromatic IR beam passed through a diamond crystalline probe pressed onto the sample. The acquired spectra will therefore be dominated by what is on the surface of the stem root (penetration depth of several microns), which should largely comprise the OLL. ATR-FTIR spectra show evidence for alpha helical structure based on presence of a component in the negative second derivative spectra at 1652 cm⁻¹ – however, the spectra are largely dominated by an intense peak at 1626 cm⁻¹ distinctive for the presence of beta sheet structure (plotting negative second derivative is a well-established analysis approach for identifying components in complex spectral bands in IR and Raman, such as the amide I) (Figure 5a-b). [33, 34]

It is important to mention here that to acquire a suitable signal with the ATR crystal, it was necessary to apply significant pressure onto the sample to establish tight contact. This leads to the generation of mechanical forces that, based on previous studies, [33, 35] are likely sufficient to convert the alpha helical structure of the OLL to a beta sheet conformation. This seems highly plausible given that mechanically activated alpha-to-beta conformational transitions have been reported in numerous materials based on IF CC proteins including wool, vimentin filaments, whelk egg capsules, hagfish slime fibers and, relevantly, freshwater mussel byssal threads from *Dreissenid* mussels. [33, 37-39] In further support of this hypothesis, we observed an increasing beta sheet content relative to the alpha helical content with increasing applied pressure indicated by the fact that the ratio of the negative second derivative peaks at 1626 cm⁻¹ (beta) to 1653 cm⁻¹ (alpha) increases by a factor of ~1.5. Considering that a significant force is already required to acquire the first measurement, we are likely already converting a large portion of the alpha helical structure by that point.

To further test this hypothesis, we measured Raman spectra from lamellae that experienced high mechanical forces through application of a sustained tensile stress to the byssus prior to measurement (Figure 5 c-d). Measurements clearly indicate that the spectrum changed compared to the unstretched samples, showing peaks consistent with an extended conformation (e.g., beta sheet) based on the shift of the amide I band to higher wavenumbers (from 1653 to 1665 cm⁻¹), the dominance of the 1230 cm⁻¹ peak in the amide III band, and the appearance of a small peak at ~1400 cm⁻¹ indicative of stretching of the alpha carbon bond in the protein backbone (Figure 5e). [32] In further support of the hypothesized alpha to beta transition, the MSP-

1 antibody stops staining the lamella after mechanical forces have been applied to the stem although the secretory vesicles, which are enriched along the cilia-lamellar border, are still detectable in the surrounding tissue (Figure 5f). This suggests that the mechanical transformation from alpha helical to beta sheet structure renders MSP-1 unrecognizable to the antibody, perhaps through formation of beta crystallites that sterically prevent access to the epitope. [40] This hypothesis is strengthened by the fact that the MSP-1 proteins within the secretory vesicles still stains strongly in these images – providing an effective internal positive control. Together, these findings strongly suggest that the alpha helical MSP-1 proteins within the OLL undergo a mechanically activated and lasting change into extended beta sheet structure. This seems biologically relevant given that the mussels experience constant mechanical loading at the seashore under the force of relentless crashing waves.

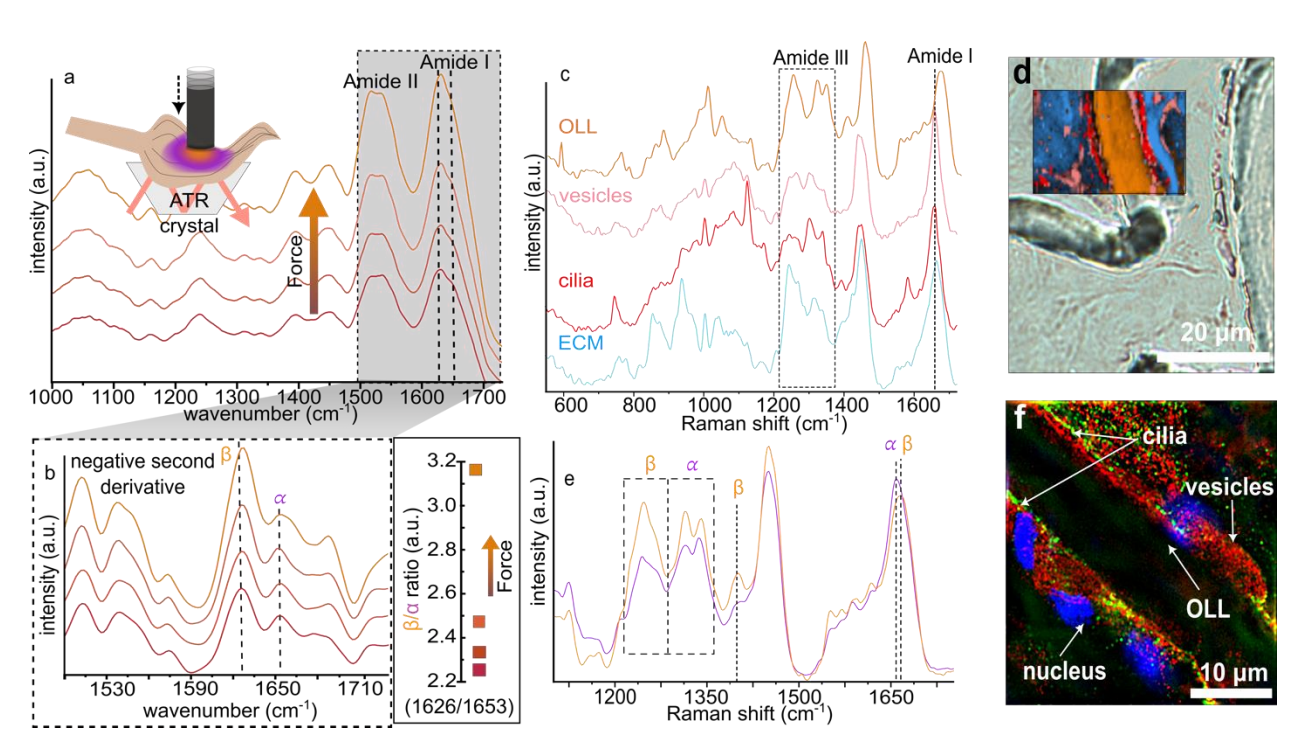


Figure 3.5. Mechanically induced alpha to beta conformational transition in the stem root OLL. (a)

ATR-FTIR spectra acquired from the stem root as a function of the force applied by the ATR crystal.

(b) Negative second derivative spectrum of the amide I band highlighted in (a), indicating the peaks corresponding to the beta sheet and alpha helix. The inset to the left shows the change in intensity of the ratio 1626 to 1653 cm⁻¹ as a function of applied force. (c) Raman spectra of a stretched stem root, with the localization of the components in the Raman map shown in (d). (e) Comparison between the Raman spectra acquired from a stretched (orange) versus unstretched root: shift in the Amide I peak, increase in the intensity of the ~1400 cm⁻¹ peak, and dominance of the beta sheet relative to the alpha helical conformation in the Amide III region after stretching. (f) Immunostained section of a generator after the application of force to the stem root; blue: nuclei, green: cilia, red: MSP-1.

3.4. Discussion

This investigation has revealed the presence of an evolutionarily conserved protein – MSP-1 – that comprises the outer layer of lamellae in the stem root of Mytilus mussels, and likely other bivalves from the oyster and scallop families based on conserved sequence homology. MSP-1 possesses prominent conformational features characteristic of the biologically important IF class of proteins. Yet, the lack of strong sequence level similarity with any of the currently identified classes (e.g., keratins, vimentins etc.), places it among the class VI orphan Ifs. [20] As predicted by AlphaFold3, it possesses three dimeric CC regions linked by short non-helical sequences, as well as non-helical terminal domains – characteristic features of all IF proteins. Thus, this appears to be a unique IF protein evolved by bivalves for a novel application – coating the surface of a functionally distinctive bio-interface unlike anything else reported in biology. [17] But what is the

function of this protein since the collagenous core likely provides sufficient mechanical stability based on its spectroscopic similarity to the proximal byssus? [17]

The conversion of MSP-1 from alpha to extended beta-like structure might be an important aspect of understanding the role and function of this protein coating. From one perspective, the alpha to beta conversion will dissipate significant mechanical energy – computational modeling of deformation of the lamin-network predicts a toughness that exceeds that of Kevlar. [38] This could be relevant given the role of the stem in dissipating energy from crashing waves – indeed every single byssus thread connects the stem root to the living tissue, an interface that is crucial for the survival of the mussel. However, as mentioned, the byssal collagen core, is already incredibly tough (as tough as Kevlar) and extensible. [38,39] Furthermore, the alpha to beta transition, and thus the toughening effect, appears to be "single-use" given that once it is converted it does not revert back to the alpha helical conformation. Thus, it seems excessive to add another protein layer if it only serves an identical purpose to the collagenous core, but less effectively. So, what might an alternative role be?

Given the previous studies of this dynamic quick release biointerface, it is interesting to consider that there might be a mechanosensory role of this alpha to beta conversion. MSP-1 is localized on the surface of the stem root lamellae coating the collagen core and is situated directly at the living/non-living biointerface with the cilia. Furthermore, it is known that mussels are able to sense their mechanical environment and respond by either producing more threads or even by jettisoning their entire byssus and moving. [14, 40-43] This sensing ability is biologically crucial considering the high amount of energy invested in producing the byssus, which can reach up to

47% of the total metabolic budget in mussels which produce threads daily.^[44] Thus, the ability to "know" when to release and when to build more threads is crucial to mussel survival and evolutionary fitness. Yet the mechanisms by which mussels make this decision are currently unknown. Perhaps the mechanoresponsive nature of the OLL plays a role. Indeed, precedence for IF CC proteins playing mechanosensory roles in cellular environments can be found in the lamins.^[45, 46]

Lamins are type V IFs found in the nuclear envelope where they function in mechanosensing and can impact gene expression. $^{[20,\,41,42]}$ The lamin meshwork is protected against mechanical forces through mechanisms integrated at every level of its hierarchical structure. $^{[38,\,41]}$ Under low mechanical loading forces, the reversible unfolding or sliding of the lamin CC domains helps absorb mechanical shocks and maintain the structural integrity of both the lamina and the nuclear contents. $^{[38,\,41]}$ When subjected to higher forces, however, an irreversible strain-induced stiffening occurs, enhancing filament stiffness, through an α -helix to β -sheet transition, further reinforcing the meshwork's resistance to failure. $^{[38,\,41]}$ This conversion is mechanically sensed through physical perturbations of cells and nuclei, facilitating the transmission of forces from the extracellular environment to the nucleus, which regulates chromatin organization, gene expression, and cell migration in both normal contexts, such as development and wound healing, and pathological contexts, such as cancer metastasis. $^{[45,47]}$

The parallels between lamin and MSP-1 are interesting considering the role of mechanosensing in stem release and byssus production. It is intriguing to consider that sustained mechanical load

placed on the byssus could mechanically convert MSP-1 from an alpha to beta conformation at the interface, which might be sensed by the mussel and provide essential information on how soundly the mussel is fastened to the surface, and whether new threads need to be laid down or whether the byssus needs to be released^[17]. Given the intimate connection between the cilia and the OLL of the stem, and the well-established role of certain cilia in mechanosensing (e.g., in hearing, in kidney cells, in embryogenesis), [48,49] this is not entirely implausible. In this model, the mechanoresponsive conversion of MSP-1 is sensed resulting in the release of neurotransmitters (e.g. serotonin) that initiate the beating of cilia and a quick release of the stem. [17] Alternatively, if the cells can sense that MSP-1 is no longer being converted, it might signal that there is no longer a need to make more byssal threads, which are highly energy intensive to fabricate. [44] This is relevant considering that mussels typically live in large sprawling clusters known as beds in which mussels experience much larger forces on the surface of the bed, than they do when protected on the inside of the cluster. [43] In principle, this could be a way for inner-cluster mussels to sense that they can stop making threads, thereby conserving resources. Numerous studies indicate that mussels regulate thread production based on mechanical factors, [14] but the mechanism by which this is achieved remains unknown. While speculative, our discovery of MSP-1 offers an intriguing avenue for future transdisciplinary studies bridging cell biology, neurobiology, biochemistry, and materials science.

3.5. Conclusion

Interfacing living and non-living materials presents a significant engineering challenge due to the mechanical stresses generated at the interface and the complications arising during device

removal. Mussels, however, have evolved a strong and easily releasable interface comprising cilia that intimately interacts with the non-living byssus stem root lamellae. In this study, we identified a novel protein, MSP-1, that comprises the outer lamellar surface, which exhibits structural similarities to intermediate filaments known for mechanically stabilizing intra- and extracellular structures^[20]. MSP-1 undergoes a structural transition from an alpha helical coiled-coil to a beta-sheet conformation – a change that provides mechanical toughness to the interface, but that might also enable mechanosensing pathways at the interface, given the intimate connection to billions of motile cilia. While the biochemical pathways underlying this putative mechanosensory process remain to be elucidated, this complex mechanical response provides valuable insights into designing multifunctional biointerfaces (e.g., implants, bioadhesives) capable of responding to external stimuli and on-demand release. Such systems could have broad implications for engineering adaptive and reversible interfaces in biomedical and industrial applications.

3.6. Materials and Methods

Materials

Mussels sourced from Prince Edward Island were purchased from the market and maintained in a tank at 12–15 °C with artificial seawater (Fluval Sea, USA), enriched with calcium, potassium, magnesium, and strontium. They were fastened to plexiglass using fishing lines and rubber bands, triggering them to produce fresh byssal threads within a few hours.

Histological imaging

For foot tissue analysis, samples were dissected, embedded in optimal cutting temperature medium (O.C.T) within a mold, and rapidly frozen in liquid nitrogen-cooled isopentane. The

frozen samples were cut into 5 μm sections with a CM1520 Leica cryostat at -20 °C. For staining with Sirius red, the sections were immersed in Bouin's solution for fixation overnight, followed by staining with 0.1% Sirius Red solution prepared in saturated Picric acid for 1 hour. Subsequently, sections were rinsed twice with 1% acetic acid. Masson's trichrome staining was performed following the manufacturer's protocol (Thermo Fisher Scientific): initially, the sections were fixed in Bouin's solution overnight and rinsed with running tap water for 5 minutes. The fixed sections were then stained with Weigert's Iron Hematoxylin solution for 10 minutes, followed by another rinse in tap water. Afterwards, the sections were immersed in a phosphomolybdic-phosphotungstic acid solution for 10 minutes to exchange dye anions. Finally, the sections were stained with aniline blue solution for 5 minutes and rinsed with 1% acetic acid for a few minutes. Sections were images using a light microscope (Axio Scope.A1, Zeiss) equipped with a 6 megapixel CCD camera (Axiocam 505 color, Zeiss).

Stem root protein extraction and characterization

To identify the protein composition in the stem root, the byssus stem was removed from the generator, and the lamellae roots were dissected away and ground up in a solution of 4 M urea and 2 M thiourea using a tissue grinder (10 roots in 150 microliter solution). The sample was centrifuged at 21,130 rcf at 4°C for 10 minutes using a Centrifuge 5424 (Eppendorf). Afterward, the supernatant was separated and mixed with 1X loading buffer. To denature the proteins, the resulting mixture was heated in boiling water for 5 minutes. The solubilized proteins (5µl) were then run on a 10% SDS-PAGE gel at 250 Amp/ 30Vs for approximately 40 min at room temperature against the Spectra Multicolour High Range Protein Ladder (Thermo Scientific).

Different gels of the same protein were stained with Silver Staining Plus Kit (Bio-Rad protocol) and subjected to western blotting using the generated antibodies against the stem root protein of weight 70 kDa.

Differential gene expression analysis was conducted with CLC Genomic Workbench (version 20.0.3). Single-end reads from each tissue and its biological replicate were mapped to the pooled transcriptome using the 'RNA-seq analysis' tool with default settings. To identify differentially expressed transcripts between tissues, p-values were adjusted for False Discovery Rates (FDR).

Mass Spectrometry proteomics

To identify the protein components of the tryptic digest from the 70 kDa protein excised from the silver-stained SDS-gel, liquid chromatography coupled with tandem mass spectrometry was employed. The lyophilized tryptic digest (80-540 ng) was reconstituted in 100 μ L of 0.1% formic acid in water. A 20 μ L aliquot of this solution was injected onto a Waters C18 BEH UPLC column (1.7 μ m, 1 x 100 mm) and fractionated at a flow rate of 50 μ L/min using a water/acetonitrile/formic acid solvent system. The gradient began with 97% solvent A (0.1% formic acid in water) and 3% solvent B (0.1% formic acid in acetonitrile), with solvent B increasing to 100% over 10 minutes. The column effluent was directed to the electrospray ionization (ESI) source of a Waters Synapt G2-Si ion mobility mass spectrometer, where data were acquired in positive ion and resolution modes. Source settings included a capillary voltage of 3.0 kV, cone voltage of 40 V, source offset of 80 V, and desolvation temperature of 250°C. Gas flow rates in the TriWave mass analyzer were: trap gas (Ar) at 2.20 mL/min, helium cell at 180 mL/min, and IMS gas flow (nitrogen) at 90 mL/min. Ion mobility separation was achieved with a travelling wave

velocity of 1000 m/s and a wave height of 40 V at a nitrogen pressure of 3.2 mbar. Peptide ions underwent alternating cycles of low and high collision energy (0.4 s duration) in the TriWave's transfer region, for MSe data acquisition. During the low energy cycle, the transfer collision energy was fixed at 5 V, while for the high energy cycle, it ramped from 25–55 V to induce collision-induced dissociation of precursor ions. Argon was used as the collision gas at a pressure of 0.03 mbar. The MSe mode acquired precursor ion m/z values (MS spectra at low collision energy) alongside their fragment ion spectra (MSMS spectra at high collision energy). A Glu-1-fibrinopeptide B external lockmass standard was used to correct the acquired m/z values. Raw data were analyzed with Protein Lynx Global Server (PLGS, Waters Inc.) by matching spectra against the *M. edulis* transcriptome. The spectral search applied a false discovery rate of 4% and thresholds of 135 low energy and 30 high energy ion counts for detecting precursor and fragment ions, respectively. This analysis identified 73 high-confidence tryptic peptides corresponding to 5 different proteins from *M. edulis*.

Mussel Foot Gland Transcriptome Assembly

Six regions of the mussel foot tissue (core gland, cuticle gland, plaque gland, stem gland, mantle, and whole foot) were dissected from four individuals, preserved in RNA later, and shipped frozen to the University of Göttingen, Germany. Upon arrival, the samples were thawed and immediately placed in Qiazol (Qiagen #79306) for total RNA extraction, following the manufacturer's protocol. RNA quality was initially assessed by standard agarose gel electrophoresis and quantified using a Nanodrop. From the 53 highest-quality samples obtained from three individuals (representing three biological replicates), the best were selected and sent

to the NIG sequencing center at the University of Göttingen for additional quality checks and library preparation. TruSeq mRNA libraries were constructed for both 50 bp single-end (SE) and 250 bp paired-end (PE) sequencing on the Illumina HiSeq2000 platform. The SE data were used to evaluate gene expression levels across all six tissues from the three biological replicates, while PE sequencing was carried out on pooled tissue types from the three individuals to assist with *de novo* transcriptome assembly (e.g., core gland samples from all three individuals were pooled and sequenced).

Before assembly, both SE and PE reads underwent multiple filtering steps. Initially, raw data files were processed using the command-line version of FastQC v.0.11.9 to assess overall data quality. Adapter sequences were removed using BBDuk from the BBTools package, with the default Illumina adapter file, a kmer of 25, and a minimum kmer length of 8. Reads were then quality-trimmed with Trimmomatic (version 0.36) before being error-corrected using Tadpole from the BBTools package with a kmer size of 50 bp. Potential rRNA contamination was removed using BBDuk and a ribo-kmer library derived from the Silva database. Finally, reads were filtered by length. After filtering, the data were processed again using FastQC v.0.11.9 to evaluate the impact of the filtering steps. Data was assembled using TransAbyss v2.0.1. Gene-specific primers were used to amplify overlapping 5' and 3' fragments of MSP-1 from RACE libraries which were subsequently cloned into pGEM-T (Promega) using standard TA-cloning methods. These cloned fragments were sequenced by standard Sanger chemistry. The protein sequence presented in Figure 2e was generated using Protter^[41] and the alignment using SeaView. [42]

FIB-SEM

This approach was adapted from a previous study on mussel foot tissue FIB-SEM analysis. [43] The generator samples (n = 2) were initially polished to expose the tissue at the block surface. These polished blocks were then transferred to the Zeiss Crossbeam 540 (Carl Zeiss Microscopy GmbH, Germany), where a trench was milled into the surface using a 30 nA FIB current at a 30 kV acceleration voltage for SEM imaging. The sample was then polished using a 700 pA FIB probe at 30 kV. To remove thin slices of the sample serially, a 1.5 nA FIB current at 30 kV was used, with each slice measuring 20 nm in thickness. After each milling step, the sample was imaged using SEM, employing both secondary and backscattered electron detectors. The resulting images had a resolution of 2048 x 1536 pixels and a lateral pixel size of 20.61 nm.

FIB-SEM Data Processing

The FIB-SEM dataset images were processed using Dragonfly software. Initially, the images were aligned using the sum of squared differences (SSD) method, followed by manual correction of the alignment. A 3D convolution filter (size 3) was then applied to the image stack, and contrast enhancement was performed using the contrast-limited adaptive histogram equalization (CLAHE) operation, with a kernel size of 100 and 256 bins. For 3D visualization of the generator, segmentation and a deep learning algorithm were utilized in Dragonfly 4.1.

STEM

To examine the generator tissue at the nanoscale, transmission electron microscopy (TEM) and scanning transmission electron microscopy (STEM) were conducted with a Thermo Scientific

Talos F200X G2 S/TEM, equipped with a Ceta 16 M CMOS Camera, operated at a 200 kV acceleration voltage. High-angle annular dark-field imaging was performed in STEM mode at magnifications of 16,500×, 46,000×, 66,000×, 130,000×, and 185,000×

Immunostaining and Structured Illumination Microscopy (SIM)

Polyclonal antibodies were produced commercially by Genscript (Piscataway, New Jersey, USA) from rabbits using two selected peptides from the MSP-1 sequence as antigens (peptide 1: CAKLRSAPQPLDEGP and peptide 2: CLRRDREDFKGRWER). For immunostaining experiments, the antibody raised against peptide 1 was used since it produced a stronger signal.

Two conditions were tested for immunostaining experiments: with and without a force applied on the stem. In both conditions, the mussels were minimally cut open. In the former case, the stem was later pulled, yet not released, while in the latter it was left intact. Directly after, the whole mussel was put in a beaker containing 4% PFA (in 1X PBS buffer) at 4 Celsius, overnight. Later, the generator tissue was dissected from the mussel and frozen in a mold containing an OCT medium (Neg 50). The frozen block was sectioned into 5 µm sections using a cryostat (Leica CM1520) and mounted on cover slips. The cover slips were functionalized with silica by immersing them in a solution of APTES/acetone (1:2 ratio) for 1 minute, followed by a 1-minute rinse in water.

In a petri dish, the coverslips, having the sections facing upwards, were covered with permeabilization buffer (1% Triton-X-100 in PBS) and incubated for 1 hr on an orbital shaker at 60-80 rpm. In a new petri dish, enough blocking buffer (2% bovine serum albumin in PBS) was

added to cover the sections and then incubated for 1 hr on an orbital shaker at 60-80 rpm. Meanwhile, a humid chamber was prepared by taping a large piece of parafilm on top of an empty 1 mL tip box that contains water at the bottom. Once the blocking step is finished, $100 \, \mu L$ droplets of a solution containing the diluted primary antibody (MSP-1 synthesized antibody raised in rabbit, GenScript) and α -tubulin T9026 to mark cilia, raised in mouse, Millipore Sigma (1:400 in PBS)) were pipetted per coverslip onto the parafilm and the coverslips were flipped face down onto the droplets using tweezers. The samples were incubated overnight at 4° C.

Afterwards, the humid chamber was removed from the fridge and the coverslips were flipped faced up into a dish containing enough blocking buffer to cover the surface. The sections were incubated on an orbital shaker at 60-80 rpm for 5 minutes. The rinsing with the blocking buffer was repeated twice, where between each step the liquid was decanted from the dish into the sink. During the last wash step, a solution containing the diluted secondary Alexa 647 (Thermo Fisher) anti-rabbit and Alexa 488 anti-mouse (Thermo Fisher) (both 1:400 in PBS). 100 μL droplets of the prepared solution were pipetted per coverslip onto a new parafilm in the humid chamber and using tweezers the coverslips were flipped face down onto the droplets. The chamber was covered with an aluminum foil to protect the sample from light and left at room temperature for 1-2 hours.

After the secondary antibody incubation, a new dish with PBS was prepared and the samples were washed 3 times with blocking buffer as previously done after the primary antibody incubation. Each dish was protected from light using aluminum foil. Next, 100 µL of 1µg/mL DAPI

in PBS were pipetted per coverslip onto a new parafilm in the humid chamber and using tweezers the coverslips were flipped face down onto the droplets. The chamber was covered with an aluminum foil to protect the sample from light and left at room temperature for 20 mins. Finally, the coverslips were put in a petri dish and washed with PBS.

To image the samples, the coverslips were mounted upside down on a microscope slide and sealed with grease to ensure the section stay hydrated after adding ~20 μ L of PBS into the slides. A 100x oil objective with an immersion oil of having a refractive index of 1.56 was used to acquire images with the different excitation wavelengths (435, 528, and 683 nm) using the DeltaVision OMX Structured Illumination Microscope (SIM). The imaging was performed in sequential mode using a structural illumination light path. The optical section spacing was 0.125 μ m within a sample thickness of 4 μ m. The images were reconstructed in SoftWorks using the 3D beam reconstruction. SIMcheck^[44] was used to determine the Weiner filter settings (Figure 2f: 0.0187 (blue), 0.0197 (green), 0.203 (red); Figure 5f: 0.0173 (blue), 0.203 (green), 0.020 (red)).

Confocal Raman Spectroscopy

Raman spectra were acquired from 5 μ m sections of the generator tissue, mounted on a microscope slide, using a linearly polarized laser (λ =532 nm) operating around 7 mW with a confocal Raman microscope (Alpha 300R, WITec). The spectra were collected with a 100× objective (NA = 0.9) and an integration time of 4 sec. The Raman scattered light was detected by a thermoelectrically cooled CCD detector behind a 600 g/mm grating. During the large area scan, a continuous scanning mode was used in True Surface mode to dynamically adjust autofocus in

real-time, following the topography of the sample. The compositional maps were analyzed through projectFive WiTec software. The spectra were initially corrected by cosmic ray removal (CRR) and background subtraction. Later, principal component analysis (PCA) was applied to identify the different components.

FTIR Spectroscopy

ATR-FTIR studies were conducted on a FTIR Vertex 70 (Bruker), equipped with an ATR objective and a single bounce diamond crystal. Each spectra were acquired from over 100 scans using a HeNe laser, after running a background measurement. The absorbed IR light was measured using a DLaTGS detector at a spectral resolution of 4cm⁻¹, covering a total range 4000 to 400 cm⁻¹. To conduct force-dependent measurement on the stem roots, a dried stem root was placed on the crystal at room temperature, and first spectra were acquired once the ATR crystal was pressed into the root until a recognizable signal appeared. The pressure was gradually increased by further tightening the screw, with additional spectra collected at each step. Data were collected using Bruker OPUS software, and the negative second derivative of the spectra was obtained using the Savitzky-Golay method with a polynomial order of 2 and a window size of 15 points. The resulting spectra were then plotted using OriginPro software.

Wide angle X-ray diffraction

WAXD studies were conducted using an Anton Paar SAXSpoint 2.0 instrument. The radiation source is a $CuK\alpha$ (wavelength, $\lambda = 1.5406$ Å), with a 2D detector (Eiger R 1 M (Horizontal)). A

slightly hydrated stem root was placed vertically (with respect to stem axes) in an enclosed tissue chamber to prevent dehydration and structural collapse under high operating vacuum conditions. The sample-to-detector distance for WAXD was 117 mm. X-ray exposure time for each sample was 30 minutes per frame for a total of 2 frames. Analysis of diffractions data was done on SAXSanalysis software (Anton Paar).

3.7. Acknowledgements

We acknowledge use of the Facility for Electron Microscopy Research (FEMR) at McGill, support for X-ray diffraction studies from H. Titi at the McGill Chemistry Characterization (MC²) Facility, and support for MS/MS proteomics from L. Taylor at the MUHC Proteomics and Molecular Analysis platform at McGill. We acknowledge Dr. G. Salinas-Riester and the team at the NIG in Göttingen for NGS sequencing and thank J. Stix for use of the ATR-FTIR microscope. MJH was funded by Natural Sciences and Engineering Research Council of Canada (NSERC Discovery Grant RGPIN-2024-04221) and Canada Research Chair awards (CRC Tier 2 950-231953). DJJ was supported by a grant from the Deutsche Forschungsgemeinschaft (JA 2108/8-1 Project number 528314512). AGH is supported by CIHR (PJT-185997) and NSERC (RGPIN/04608). FJ was supported by the Max Planck Society. LY was supported by an FRQNT Québec Merit fellowship. Conflicts of interest: The authors declare that they have no competing interests.

Data and materials availability: All data generated or analyzed during this study are included in this published article (and its supplementary information files) besides transcriptomic data, which are available on the NIH BioSample Database with project number PRJNA1225934 and X files that have been uploaded onto X server.

3.8. References

- 1. S. M. Wellman *et al.*, A materials roadmap to functional neural interface design. *Advanced Functional Materials* **28**, 1701269 (2018).
- 2. R. Elnathan *et al.*, Biointerface design for vertical nanoprobes. *Nat. Rev. Mater.* **7**, 953-973 (2022).
- 3. Y. Fang *et al.*, Dissecting biological and synthetic soft–hard interfaces for tissue-like systems. *Chemical Reviews* **122**, 5233-5276 (2022).
- 4. Y. Luo et al., Technology roadmap for flexible sensors. ACS Nano 17, 5211-5295 (2023).
- 5. M. W. Tibbitt, C. B. Rodell, J. A. Burdick, K. S. Anseth, Progress in material design for biomedical applications. *Proc. Nat. Acad. Sci. USA* **112**, 14444-14451 (2015).
- 6. X. Wang *et al.*, Bioadhesive and conductive hydrogel-integrated brain-machine interfaces for conformal and immune-evasive contact with brain tissue. *Matter* **5**, 1204-1223 (2022).
- 7. Z. Liu, M. A. Meyers, Z. Zhang, R. O. Ritchie, Functional gradients and heterogeneities in biological materials: Design principles, functions, and bioinspired applications. *Progress in Materials Science* **88**, 467-498 (2017).
- 8. L. Adler, K. Buhlin, L. Jansson, Survival and complications: A 9- to 15-year retrospective followup of dental implant therapy. *J Oral Rehabil* **47**, 67-77 (2020).
- 9. T. Berglundh, L. Persson, B. Klinge, A systematic review of the incidence of biological and technical complications in implant dentistry reported in prospective longitudinal studies of at least 5 years. *Journal of Clinical Periodontology* **29**, 197-212 (2002).
- 10. S. Amini *et al.*, A diecast mineralization process forms the tough mantis shrimp dactyl club. *Proceedings of the National Academy of Sciences* **116**, 8685-8692 (2019).

- 11. A. Miserez, T. Schneberk, C. Sun, F. W. Zok, J. H. Waite, The transition from stiff to compliant materials in squid beaks. *Science* **319**, 1816-1819 (2008).
- 12. L. Rossetti *et al.*, The microstructure and micromechanics of the tendon–bone insertion.

 Nature Materials **16**, 664-670 (2017).
- 13. L. Youssef, M. Renner-Rao, E. D. Eren, F. Jehle, M. J. Harrington, Fabrication of tunable mechanical gradients by mussels via bottom-up self-assembly of collagenous precursors. *ACS Nano* **17**, 2294-2305 (2023).
- 14. E. Carrington, J. H. Waite, G. Sara, K. P. Sebens, Mussels as a model system for integrative ecomechanics. *Annu. Rev. Mar. Sci.* **7**, 443-469 (2015).
- 15. J. H. Waite, M. J. Harrington, Following the thread: Mytilus mussel byssus as an inspired multifunctional biomaterial. *Canadian Journal of Chemistry* **100**, 197-211 (2021).
- 16. A. Tamarin, An ultrastructural study of byssus stem formation in mytilus californianus. *Journal of Morphology* **145**, 151-177 (1975).
- 17. J. Sivasundarampillai *et al.*, A strong quick-release biointerface in mussels mediated by serotonergic cilia-based adhesion. *Science* **382**, 829-834 (2023).
- 18. H. Y. Yoo *et al.*, Sugary interfaces mitigate contact damage where stiff meets soft. *Nature Communications* **7**, 11923 (2016).
- 19. J. Xue *et al.*, Structural mechanisms of the human cardiac sodium-calcium exchanger ncx1.

 Nature Communications 14, 6181 (2023).
- 20. G. Dutour-Provenzano, S. Etienne-Manneville, Intermediate filaments. *Current Biology* **31**, R522-R529 (2021).

- 21. J. Jumper *et al.*, Highly accurate protein structure prediction with alphafold. *Nature* **596**, 583-589 (2021).2
- 22. Abramson, J.; Adler, J.; Dunger, J.; et al. Accurate Structure Prediction of Biomolecular Interactions with AlphaFold 3. Nature 630, 493–500 (2024).
- 23. Simm, D.; Hatje, K.; Kollmar, M. Waggawagga: Comparative Visualization of Coiled-Coil Predictions and Detection of Stable Single α -Helices (SAH Domains). Bioinformatics 31, 767–769 (2015).
- 24. Strelkov, S. V.; Herrmann, H.; Aebi, U. Molecular Architecture of Intermediate Filaments. BioEssays 25, 243–251 (2003).
- 25. Chernyatina, A. A.; Nicolet, S.; Aebi, U.; Herrmann, H.; Strelkov, S. V. Atomic Structure of the Vimentin Central α -Helical Domain and Its Implications for Intermediate Filament Assembly. Proceedings of the National Academy of Sciences 109, 13620–13625 (2012).
- 26. Merveille, A. C.; et al. CCDC39 is Required for Assembly of Inner Dynein Arms and the Dynein Regulatory Complex and for Normal Ciliary Motility in Humans and Dogs. Nat. Genet. 43, 72–78 (2011).
- 27. Rabouille, C. Pathways of Unconventional Protein Secretion. Trends in Cell Biology 27, 230–240 (2017).
- 28. Parvanian, S.; Coelho-Rato, L. S.; Eriksson, J. E.; Patteson, A. E. The Molecular Biophysics of Extracellular Vimentin and Its Role in Pathogen-Host Interactions. Curr. Opin. Cell Biol. 85, 102233 (2023).

- 29. Pauling, L.; Corey, R. B.; Branson, H. R. The Structure of Proteins: Two Hydrogen-Bonded Helical Configurations of the Polypeptide Chain. Proceedings of the National Academy of Sciences 37, 205–211 (1951).
- 30. Er Rafik, M.; Doucet, J.; Briki, F. The Intermediate Filament Architecture as Determined by X-Ray Diffraction Modeling of Hard α -Keratin. Biophysical Journal 86, 3893–3904 (2004).
- 31. Harrington, M. J.; Gupta, H. S.; Fratzl, P.; Waite, J. H. Collagen Insulated from Tensile Damage by Domains That Unfold Reversibly: In Situ X-Ray Investigation of Mechanical Yield and Damage Repair in the Mussel Byssus. J. Struct. Biol. 167, 47–54 (2009).
- 32. Harrington, M. J.; et al. Pseudoelastic Behaviour of a Natural Material Is Achieved via Reversible Changes in Protein Backbone Conformation. Journal of the Royal Society Interface 9, 2911–2922 (2012).
- 33. Simmons, M.; et al. Invasive Mussels Fashion Silk-Like Byssus via Mechanical Processing of Massive Horizontally Acquired Coiled Coils. Proceedings of the National Academy of Sciences 120, e2311901120 (2023).
- 34. Yang, H.; Yang, S.; Kong, J.; Dong, A.; Yu, S. Obtaining Information about Protein Secondary Structures in Aqueous Solution Using Fourier Transform IR Spectroscopy. Nature Protocols 10, 382–396 (2015).
- 35. Jafari, M. J.; et al. Force-Induced Structural Changes in Spider Silk Fibers Introduced by ATR-FTIR Spectroscopy. ACS Applied Polymer Materials 5, 9433–9444 (2023).
- 36. Zhmurov, A.; et al. Mechanical Transition from α -Helical Coiled Coils to β -Sheets in Fibrin(ogen). J. Am. Chem. Soc. 134, 20396–20402 (2012).

- 37. Fudge, D. S.; Gardner, K. H.; Forsyth, V. T.; Riekel, C.; Gosline, J. M. The Mechanical Properties of Hydrated Intermediate Filaments: Insights from Hagfish Slime Threads. Biophysical Journal 85, 2015–2027 (2003).
- 38. Kreplak, L.; Doucet, J.; Dumas, P.; Briki, F. New Aspects of the α -Helix to β -Sheet Transition in Stretched Hard α -Keratin Fibers. Biophysical Journal 87, 640–647 (2004).
- 39. Miserez, A.; Guerette, P. A. Phase Transition-Induced Elasticity of α -Helical Bioelastomeric Fibres and Networks. Chemical Society Reviews 42, 1973–1995 (2013).
- 40. Mortimer, G. M.; Minchin, R. F. Cryptic Epitopes and Functional Diversity in Extracellular Proteins. The International Journal of Biochemistry & Cell Biology 81, 112–120 (2016).
- 41. Sapra, K. T.; et al. Nonlinear Mechanics of Lamin Filaments and the Meshwork Topology Build an Emergent Nuclear Lamina. Nat. Commun. 11, 6205 (2020).
- 42. Gosline, J.; et al. Elastic Proteins: Biological Roles and Mechanical Properties. Philos. Trans. R. Soc. Lond. B Biol. Sci. 357, 121–132 (2002).
- 43. Côté, I. M. Effects of Predatory Crab Effluent on Byssus Production in Mussels. Journal of Experimental Marine Biology and Ecology 188, 233–241 (1995).
- 44. Roberts, E. A.; et al. Resource Allocation to a Structural Biomaterial: Induced Production of Byssal Threads Decreases Growth of a Marine Mussel. Functional Ecology 35, 1222–1239 (2021).
- 45. Vahabikashi, A.; Adam, S. A.; Medalia, O.; Goldman, R. D. Nuclear Lamins: Structure and Function in Mechanobiology. APL Bioeng. 6, 011503 (2022).
- 46. Cho, S.; et al. Mechanosensing by the Lamina Protects against Nuclear Rupture, DNA Damage, and Cell-Cycle Arrest. Developmental Cell 49, 920–935.e925 (2019).

- 47. Danielsson, B. E.; et al. Nuclear Lamina Strain States Revealed by Intermolecular Force Biosensor. Nature Communications 14, 3867 (2023).
- 48. Djenoune, L.; et al. Cilia Function as Calcium-Mediated Mechanosensors That Instruct Left-Right Asymmetry. Science 379, 71–78 (2023).
- 49. van Megen, W. H.; Hoenderop, J. G. J. Bend or Break: The Primary Cilium as a Potential Regulator of Electrolyte Reabsorption in the Kidney. Current Opinion in Endocrine and Metabolic Research 34, 100506 (2024).
- 50. Pan, B.; et al. Tmc1 Forms the Pore of Mechanosensory Transduction Channels in Vertebrate Inner Ear Hair Cells. Neuron 99, 736–753.e736 (2018).
- 51. Omasits, U.; Ahrens, C. H.; Müller, S.; Wollscheid, B. Protter: Interactive Protein Feature Visualization and Integration with Experimental Proteomic Data. Bioinformatics 30, 884–886 (2014).
- 52. Gouy, M.; Guindon, S.; Gascuel, O. Seaview Version 4: A Multiplatform Graphical User Interface for Sequence Alignment and Phylogenetic Tree Building. Molecular Biology and Evolution 27, 221–224 (2010).
- 53. Jehle, F.; et al. Collagen Pentablock Copolymers Form Smectic Liquid Crystals as Precursors for Mussel Byssus Fabrication. ACS Nano 15, 6829–6838 (2021).

3.9. Supplementary material

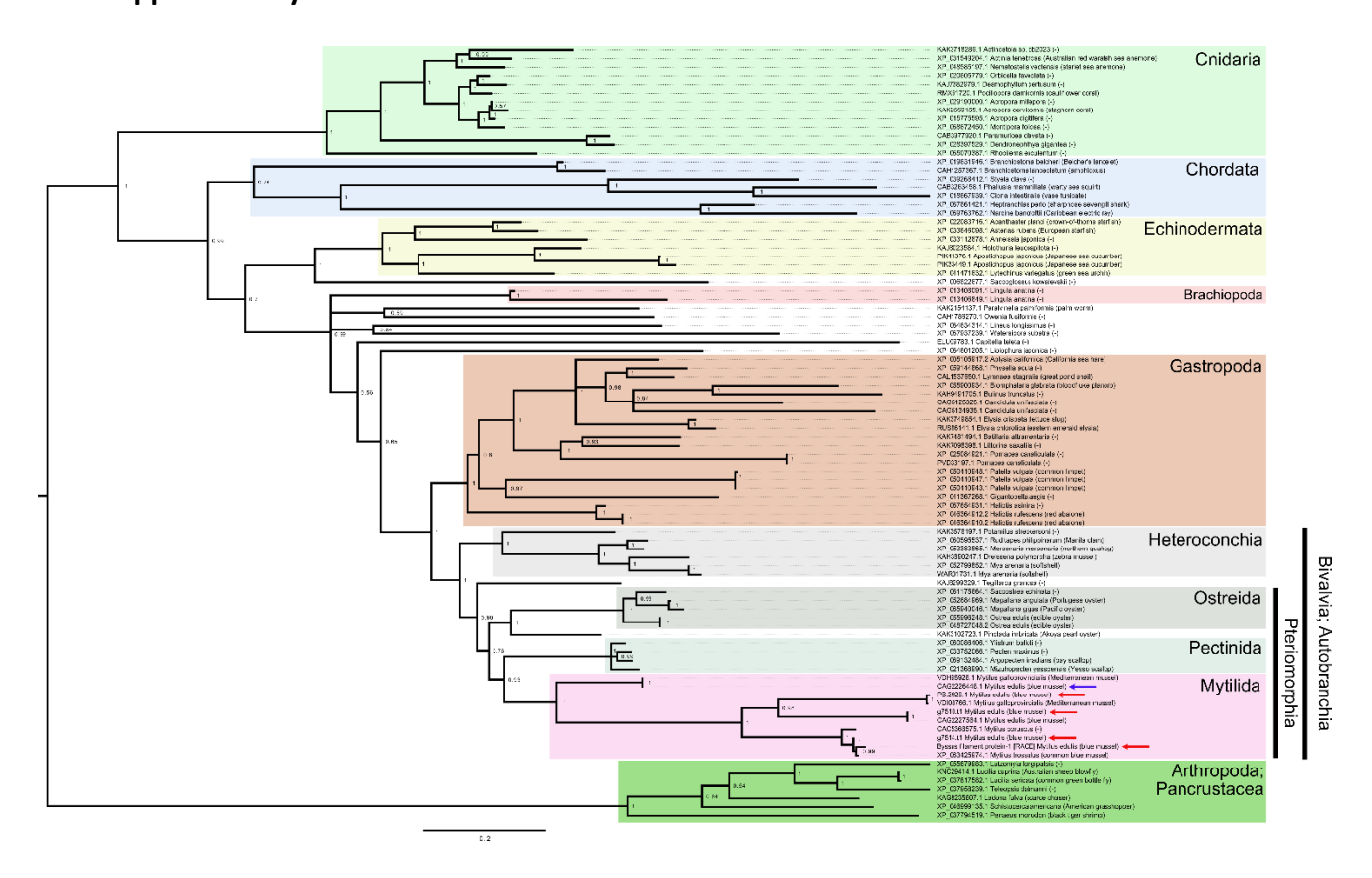


Figure S 3-1. .Sequences with similarity to M. edulis mussel stem protein 1 (MSP-1) from a broad phylogenetic range were identified via a BLASTp search against ClusteredNR (searching MSP-1 against standard NR returns hits only against the Autobranchia). Sequences were aligned using Clustal Omega¹⁰² and conserved blocks were extracted using Gblocks¹⁰³.A MrBayes v3.2.7a ¹⁰⁴ analysis was performed with the following parameters (lset rates=gamma; prset aamodelpr=mixed; mcmcp nruns=4 ngen=2,000,000 printfreq=1000 samplefreq=1000 nchains=3 savebrlens=yes temp=0.2 stoprule=yes;) and a 50% consensus tree was generated. Sequences, alignment, and Gblocked files are provided in the supplementary material. Taxonomic lineage information was obtained from NCBI Taxondb.



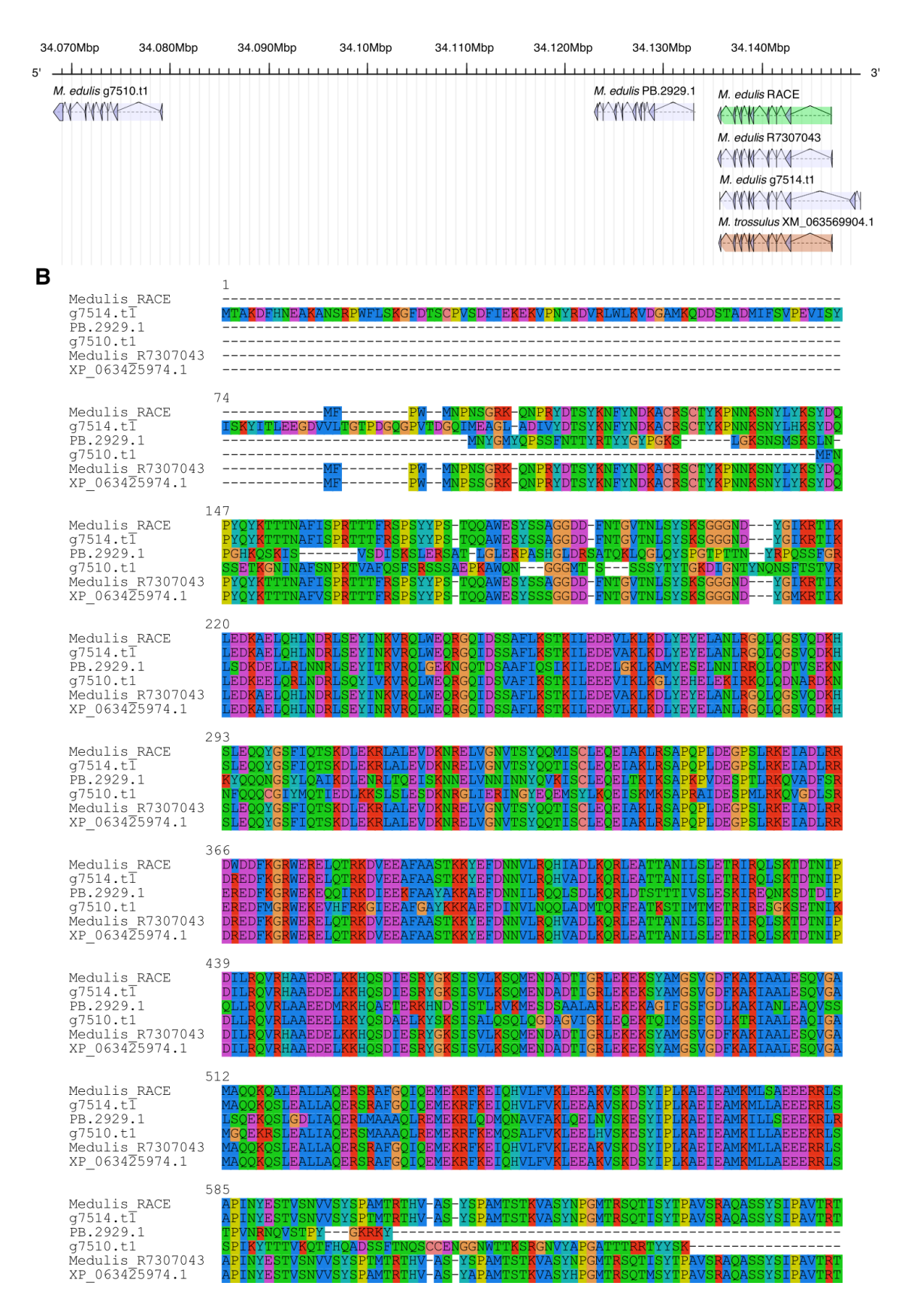


Figure S3-2..Genomic locations, exon/intron structures and sequence similarity of M. edulis and M. trosulus MSP-1 orthologs and paralogs. A. 3 copies of M. edulis MSP-1 are located on chromosome 2 from the M. edulis genome reported by Regan et al. (2024). One gene model from this genome assembly (g7514.t1) closely matches the sequence we were able to RACE in both 5' and 3' directions, however our 5' RACE fragments do not match the 5' end predicted by the gene model g7514.t1, and the closest contig from our transcriptome assembly independently concurs with our RACE data (R7307043). In addition, an ortholog from M. trossulus (XM_063569904.1) agrees with the 5' end of our RACE sequence in contrast to g7514.t1. Interestingly no signal sequences could be detected in any of these orthologous or paralogous gene models. B. An alignment of all sequences located on this chromosome highlights their similarity to each other.

Movie 3.1. 3D model reconstructed from FIB-SEM stacks acquired from the generator.

Chapter 4

4. Fabrication of Tunable Mechanical Gradients by Mussels via Bottom-Up Self-

Assembly of Collagenous Precursors

Preface

Within the overarching theme of investigating material interfaces in the mussel byssus, I shift my focus in this chapter from the living/non-living interface at the byssus stem root to the soft-hard interface between the distal and proximal regions of byssal threads. This particular interface plays a crucial role in mitigating mechanical stresses along the thread arising from crashing waves. However, the exact mechanism through which it does so remains unclear. It has been hypothesized that a compositional gradient of protein variants exists between the stiff distal and elastic proximal regions of the byssus, but little is known about the mechanical response, structure, and composition of this gradient at the micron scale. In this chapter, I harnessed a combination of advanced mechanical testing with video extensometry, confocal Raman spectroscopic imaging, and electron microscopy to identify a compositional, structural, and mechanical gradient on the scale of tens of microns. To further investigate the formation of this gradient, I collaborated with former graduate student Max Renner-Rao, who utilized vesicle purification protocol, SDS-PAGE, and mass spectrometry techniques to undertake in vitro fiber formation experiments. This chapter highlights the remarkable ability of the mussel to engineer interfaces for mitigating the mechanical mismatch between different materials. It provides insights into how the mussel controls protein assembly through complex regulatory mechanisms,

offering valuable lessons in materials science. Ongoing investigations into other interfaces within the byssus were also performed, but these are not included in this thesis.

Reprinted with permission from Youssef, L.; Renner-Rao, M.; Eren, E.D.; Jehle, F. Harrington, M. J.; Fabrication of Tunable Mechanical Gradients by Mussels via Bottom-Up Self-Assembly of Collagenous Precursors. ACS Nano 2023, 17, 3, 2294–2305. L.Y and M.R.R. contributed equally to this work. An incomplete portion of this manuscript exists as a chapter in a traditional thesis from Max Renner-Rao.

4.1. Abstract

Functionally graded interfaces are prominent in biological tissues and are used to mitigate stress concentrations at junctions between mechanically dissimilar components. Biological mechanical gradients serve as important role models for bioinspired design in technically and biomedically relevant applications. However, this necessitates elucidating exactly how natural gradients mitigate mechanical mismatch and how such gradients are fabricated. Here, we applied a cross-disciplinary experimental approach to understand structure, function, and formation of mechanical gradients in byssal threads – collagen-based fibers used by marine mussels to anchor on hard surfaces. The proximal end of threads is approximately 50-fold less stiff and twice as extensible as the distal end. However, the hierarchical structure of the distal-proximal junction is still not fully elucidated, and it is unclear how it is formed. Using tensile testing coupled with video extensometry, confocal Raman spectroscopy, and transmission electron microscopy on native threads, we identified a continuous graded transition in mechanics, composition, and nanofibrillar morphology, which extends several hundreds of microns and which can vary

significantly between individual threads. Furthermore, we performed in vitro fiber assembly experiments using purified secretory vesicles from the proximal and distal regions of the secretory glands (which contain different precursor proteins), revealing spontaneous self-assembly of distinctive distal- and proximal-like fiber morphologies. Aside from providing fundamental insights into the byssus structure, function, and fabrication, our findings reveal key design principles for bioinspired design of functionally graded polymeric materials.

4.2. Introduction

Embedded biomedical devices, such as brain machine interfaces, dental implants and prosthetics often produce large mechanical stresses at the interface between the two materials due to a mismatch in mechanical properties¹⁻⁴. The magnitude of the stiffness mismatch generated between the soft-hard interfaces largely determines the likelihood of structural failure and delamination at the contact zone^{3, 4}, and thus, technological malfunction. Currently, engineers have not developed an effective solution to completely avoid mismatches at interfaces^{1, 2, 5}; however, many biological organisms including spiders, squids, lobsters, mussels and various plants have independently evolved a material design strategy that effectively circumvents this universal engineering challenge – namely functional graidents.⁴ As a concrete example, the tip of a squid beak, used to crush prey, is 200-fold stiffer than its base which interfaces with the living tissue; yet, stress concentrations are avoided through a compositional and mechanical gradient in which cross-link density and material stiffness decreases progressively from the tip to the base⁶. More generally, mechanical gradients in nature originate from variations in factors such as biomolecular or mineral composition, as well as structural organization of components at

multiple hierarchical length scales⁴. Furthermore, gradients can be either continuous or discontinuous, and they can be localized within the entire volume of material or only within a confined zone present between dissimilar components.⁴ Mussel byssal threads are a prominent example of a functionally graded protein fiber (Fig. 4.1a),^{3, 7, 8} which makes them an ideal model system to investigate for inspiring functionally graded polymeric materials^{9, 10}.

Under the pressure of large hydrodynamic forces from crashing waves, survival of marine mussels (Mytilus edulis) is dependent on their ability to attach to the hard substratum by means of an extracellular collection of collagenous fibers called byssal threads (Fig. 4.1a-b). 11, 12 Byssal threads have two morphologically and mechanically distinct regions, known as the proximal (closer to the tissue) and distal (closest to the substrate) regions (Fig. 4.1b-d)^{11, 13, 14}. The distal region has a fibrous appearance and exhibits stiffness values of between 500-800 MPa, extensibilities of ~100%, a large hysteresis (~70%) during cyclic loading, and the capacity to self-heal following pseudoplastic damage^{11, 13}. In contrast, the proximal thread, which is corrugated in appearance superficially resembling an elephant's trunk, is at least 10-fold less stiff and twice as extensible 11, ¹³. It has been proposed that a gradual mechanical transition from distal to proximal thread functions to mitigate local stress concentrations inherent in linking the soft mussel tissue to hard rocky surfaces⁸, but the mechanical transition between the two regions is not well characterized. Both the distal and proximal regions are comprised primarily of a family of collagen-like structural proteins, known as preCols, which come in three distinct variants - preCol-D, -P and -NG (Fig. 4.1e)¹⁵⁻¹⁷. Every preCol variant has a similar central collagen domain and two histidine-rich domains (HRDs) located at the N- and C-termini¹⁸. However, between the collagen domains and

HRDs on both ends are variable flanking domains that differ significantly between the variants and are proposed to play a major role in determining the different mechanical properties between the two thread ends^{7, 14, 18}.

Correlated to the observed structural and mechanical differences (Fig. 4.1c-d), PreCol-P, which is heavily enriched in the soft and extensible proximal region of the threads, possesses flanking domains with sequences reminiscent of soft, elastomeric fibrous proteins such elastin and spider flagelliform silk¹⁵. In contrast, preCol-D, which is heavily enriched in the stiffer distal region of the thread, possesses flanking domains that resemble the sequences from stiff spider dragline silk polyalanine runs and glycine-rich spacers, which are known to assume beta sheet structure. 19-22 In addition to the preCols, there are two matrix proteins – thread matrix protein-1 (TMP-1) and proximal thread matrix protein-1 (PTMP-1)^{23, 24}. While TMP-1 is distributed throughout the whole threads, PTMP-1 is found exclusively in the proximal region²⁵, prompting hypotheses that it contributes to the observed morphological and mechanical differences of the proximal thread.²³, ²⁴ Indeed, it has been hypothesized that a gradient of the different preCol and matrix proteins variants is the key to understanding the byssal thread functional gradient^{7, 14, 26}. Yet, the mechanical, structural, and compositional transition between the proximal and distal thread regions has never been explicitly characterized across all relevant length scales, and, moreover, it is currently unclear how this gradient is fabricated by the mussel. Indeed, fabrication of byssal threads proceeds via secretion of liquid crystalline preCol precursors contained in micron-scale secretory vesicles, which are proposed to solidify induced by a subtle pH trigger.²⁷⁻³⁰ How this secretory process results in a high performance fiber with functionally graded properties is as of yet unknown.

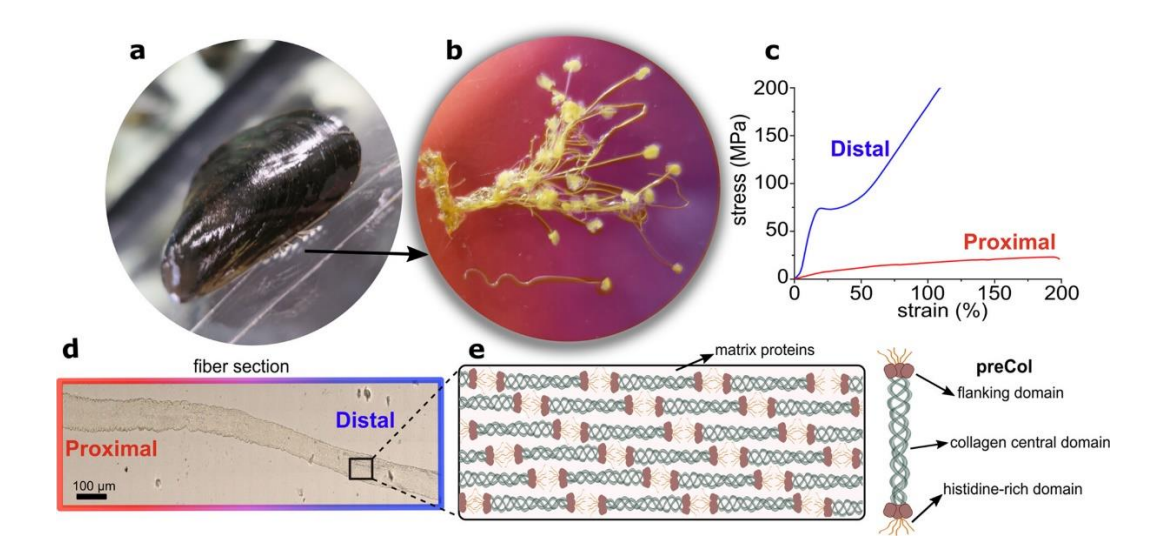


Figure 4.1.Hierarchical structure of the mussel byssus. Threads attaching a mussel to a hard surface. (b) Byssus removed from mussel comprised of many individual threads. Each thread has a wavy proximal region (left) and a distal straight region (right). (c) Characteristic pull to break stress—strain plots showing the tensile mechanical behavior of the separated distal (blue) and proximal (red) regions. ¹¹ (d) Magnified image of a longitudinal section for the transition region between distal and proximal. (e) The byssal thread core consists of collagenous proteins named preCols, which are organized in a semicrystalline manner and surrounded by matrix proteins. A single preCol has three domains: the central collagen, flanking, and histidine-rich domains. The goals of this study are two-fold: 1) understand the compositional, structural, and mechanical nature of the transition region between the distal and proximal regions from the micro- to the nanoscale and 2) elucidate the process by which the gradient is formed during byssus fabrication. To achieve these goals, we undertook a cross-disciplinary and multiscale experimental approach harnessing mechanical testing coupled with video-extensometery, transmission electron

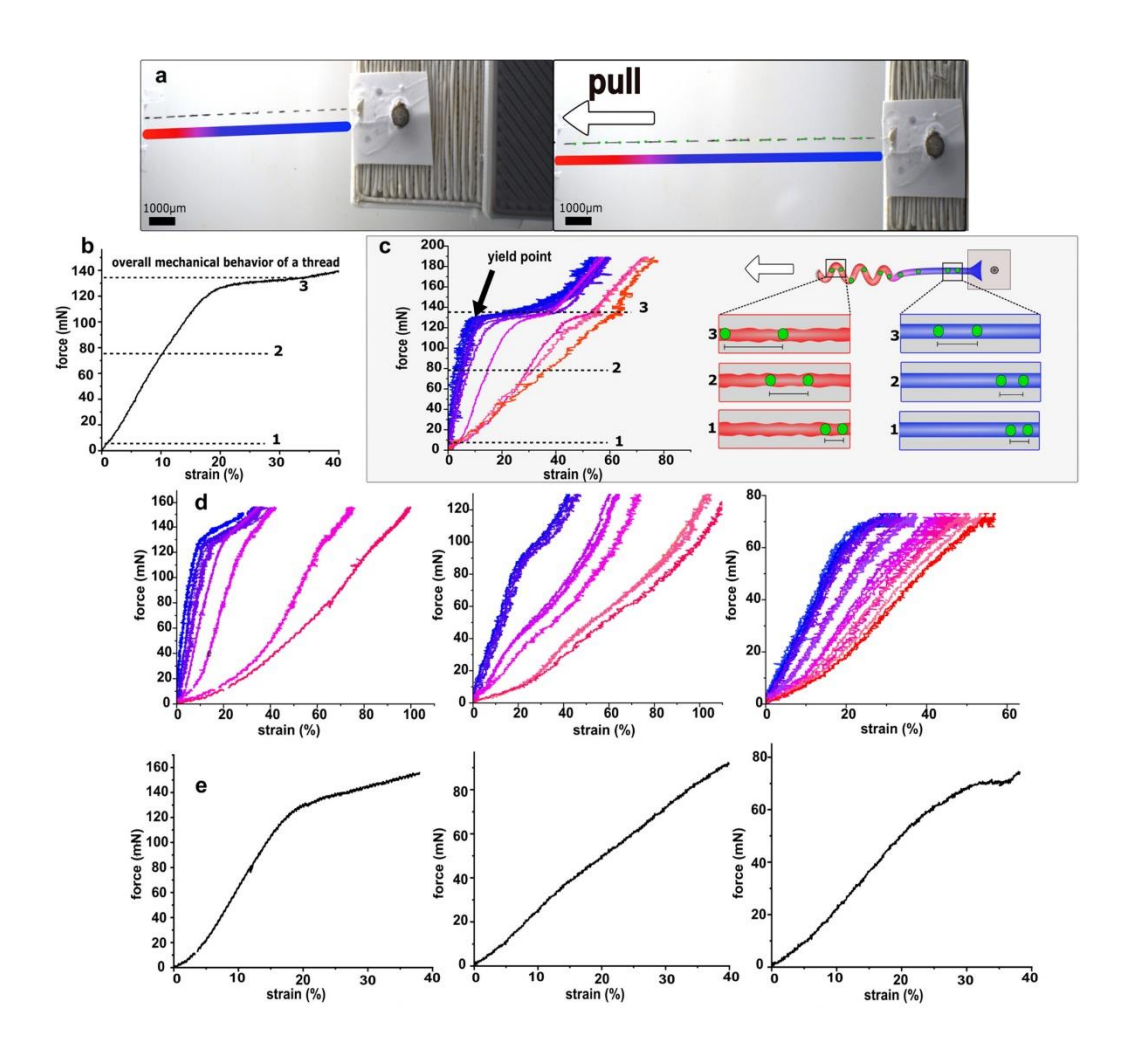
microscopy and confocal Raman spectroscopy. To further explore the gradient formation process, we purified intact core secretory vesicles from the distal and proximal regions of the foot and performed biochemical characterization and in vitro assembly experiments. Investigations provide a fundamental biochemical, structural, and mechanical understanding of the byssal thread gradient across the nanometer to micron to millimeter scales. Extracted insights are highly relevant for designing and fabricating functionally graded polymeric materials for both technical and biomedical applications.

4.3. Results

Microscale Mechanical Testing of Whole Byssal Threads with Video Extensometry

In order to record strains in localized regions of a whole byssal thread, we used mechanical tensile testing coupled with video extensometry. In this way, we aimed to determine the nature of the mechanical gradient in threads with sub-millimeter-scale resolution. Threads were marked with black acrylate paint spots along the entire length to generate sufficient contrast to act as positional markers for image tracking in the recorded videos (Fig. 4.2a, Supporting Fig. S4.1, Supporting Movie S4.1). Using a high-resolution camera to track the relative change in position of the paint spots across the entire length of individual byssal threads while mechanically stretching the fiber, we were able to calculate strain values of individual segments of the thread moving from the proximal to distal (Supporting Fig. S4.1). Strain values determined from video extensometry were correlated in real time to the force measured by the load cell, enabling the generation of force-strain curves for each individual segment moving from the distal to the proximal region (Fig. 4.2b-c). It was not feasible to plot force data as engineering stress because

the diameter of the fiber varies significantly moving from the distal to proximal region. However, since the entire thread experiences identical force along its length at any given moment, the force-strain plots allow us to visualize how different segments of the fiber strain differently under uniform mechanical load.



Photographs of the tensile test set up before and after stretching a fiber. Black paint spots on the thread were used for video extensometry to calculate local strains. Colored line beneath the thread shows the relative lengths of the distal (blue), transition (pink) and proximal regions (red).

(b) The overall mechanical behavior of the thread and the (c) force-strain plot showing the behaviors of each segment along this thread with color code matching the diagram in (a). Schematic illustrates the relative strains in the distal and proximal regions at the force values (1) before stretching, (2) pre-yield, and (3) post-yield. (d) Force-strain plots from three other threads highlighting the diversity of mechanical behavior of individual threads from the same byssus. (e) Whole thread force-strain plots corresponding to each thread in panel (d).

Consistent with the previous mechanical testing results for separated distal and proximal regions $^{11, 13, 31}$ (Fig. 4.1c), the distal zone (in blue) showed a prominent yield point and a plateau which indicates the transition of the thread from a high-stiffness phase to a low-stiffness phase while the proximal zone (in red) exhibits a much softer and more extensible response (Fig. 4.2b). The stark differences in mechanical response of these two regions is especially obvious by examining the strain values at specific forces before and after yield in the distal region. For instance, in the example thread shown in Figure 4.2b, before yield (F \approx 80 mN) segments in the distal region strain by only \approx 5% while the proximal-most segment exhibits a strain of \approx 40%. Conversely, after the distal yield plateau (F \approx 150 mN), the difference in strain values between distal and proximal segments becomes less prominent, at approximately 50% and 70% respectively. This indicates that at low applied forces prior to yield, the proximal region accounts for most of the total thread strain, while under higher loads beyond the yield plateau the distal and proximal region contribute more equally.

The mechanical response of the segments at the extreme ends of all threads tested are consistent with previous studies on separated distal and proximal regions. ^{11, 13} However, the mechanical behavior of the distal-proximal interface was never previously investigated. Here, we observed in all threads tested that there are segments (in pink), moving from the distal to the proximal regions, that exhibit a mechanical response that is intermediate to the canonical distal and proximal responses, suggesting the presence of a transition zone between the extremes (Fig. 4.2b-c). Notably, the closer a transition segment is located to the distal region, the more it resembles the distal behavior (i.e., stiff with a yield behavior) and the further it is, the more it behaves like a proximal region (i.e., soft with no yield behavior). Indeed, this change in mechanical behavior as a function of location along the byssus indicates the presence of a continuous gradient in a localized region of the thread on the scale of hundreds of microns.

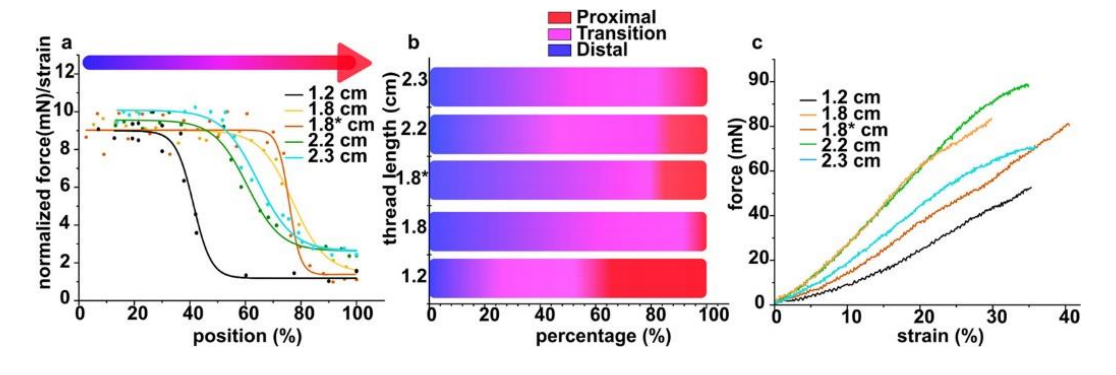


Figure 4.3. Variation in lengths of the proximal, transition and distal region and whole thread mechanics. (a) Stiffness profiles along the length of different threads from the same byssus. Changes in stiffness (slope of force-strain curve for each segment in video extensometry) were plotted moving from the distal to the proximal region as a function of relative distance along the thread. (b) Visualization of the relative lengths of the proximal, transition and distal regions in each thread based on data in panel (a). (c) The overall mechanical behavior of the whole threads

from panel (a). Force-strain curves for the individual segments comprising each thread can be found in Supporting figure S4.2.

While all threads tested exhibited a transition region with a continuous gradation of the mechanical response, the distribution of the transition gradient varied significantly between different threads (Fig. 4.2c), regardless of whether they originated from the same or different mussels and independent of their length. To compare the gradients between different threads, we calculated the slope of the linear elastic region of each segment in five different byssal threads (Fig. 4.3, Supporting Fig. S4.2). Slope values were then plotted as a function of the normalized distance along the length of the thread (expressed as a percentage of total length), starting from the distal and ending in the proximal region, as shown in Figure 4.3a. Examination of different byssal threads from a single mussel reveals an enormous variation in both the relative length of the proximal and distal regions of the fibers and in the length of the transition zone (Fig. 4.3b, Supporting Fig. S4.2). In some threads, the distal region comprises the majority of the length and in others the proximal dominates. In some threads there is a rather abrupt transition occurring over a short length, while in others it occurs over a larger length. It is worth mentioning that while the extension rate is held constant in all experiments and the entire thread experiences the same load, the different stiffness and extensibility of the proximal, transition and distal regions means that at any given moment, these different regions are experiencing a different instantaneous strain rate. Given the viscoelastic nature of these fibers^{20, 32}, this is highly relevant to the overall mechanical response. This topic is discussed further in the supporting information.

These different combinations of the distal:proximal ratios and the length of the transition region result in byssal threads with distinctive overall mechanical behaviors, when the force-strain curves of the entire thread are examined (Fig. 4.2d, 3c and Supporting Fig. S4.2 and S3). Given the diversity of different thread "types" observed, extracting clear rules relating thread morphology with specific features of whole thread performance was not straightforward. Nonetheless, we consistently observed that whole threads with a larger or softer proximal region tended to exhibit a longer "toe" region in the whole thread curve (an initial low stiffness region before increasing in stiffness). Conversely, whole threads that had a larger proportion of distal region were largely missing the prominent toe region, and typically exhibited a clear yield point at lower strains. However, depending on the relative length of the transition region, this relationship could be shifted in either direction. Furthermore, our observations contradict previous assertions that the distal and proximal regions make up 80% and 20% of the thread, respectively, in order to optimize energy dissipation during loading.³³ It was stated that the use of 20 % soft material, i.e. the proximal region, is important for force reduction and impact absorption³³, however, the unexpected variation in the distal:proximal ratios between individual threads (Fig. 4.3) indicates that threads do not always follow that rule. The potential biological role of this variation is unclear.

Structural Investigation of Byssus Gradient under STEM

To investigate the structural origin of the mechanical variation along the gradient transitioning from distal to proximal, we characterized the nanostructure of the fibers using scanning transmission electron microscopy (STEM) in high angle annular dark field (HAADF) mode (Fig. 4.4).

The osmium-stained collagen fibrils along the byssus are oriented parallel to the fiber axis; however, their nanoscale morphology varies significantly moving from the distal to proximal regions. Consistent with previous imaging studies using standard TEM 34 , the distal region exhibits a highly fibrillar structure with tightly packed sheets of fibers, whereas the fibrils in the proximal region are wavy and crimped. This wavy structure is reminiscent of the characteristic crimped structure of collagenous tissues including tendon, aortic wall and nerve sheath tissue 35 , but with a much tighter crimp ($100 - 200 \text{ nm} \text{ vs. } 1 - 100 \text{ }\mu\text{m}$, respectively). In images acquired from the transition region, we observed hybrid fibrils that combine features of both the proximal and distal regions – overall the fibrils possess less pronounced and looser waviness compared with proximal fibrils, yet they are not as straight as the distal fibrils (Fig. 4.4). This suggests that the graded transition in mechanical properties in the transition region may be dictated in part at the fibril morphology level, but what controls this morphology?

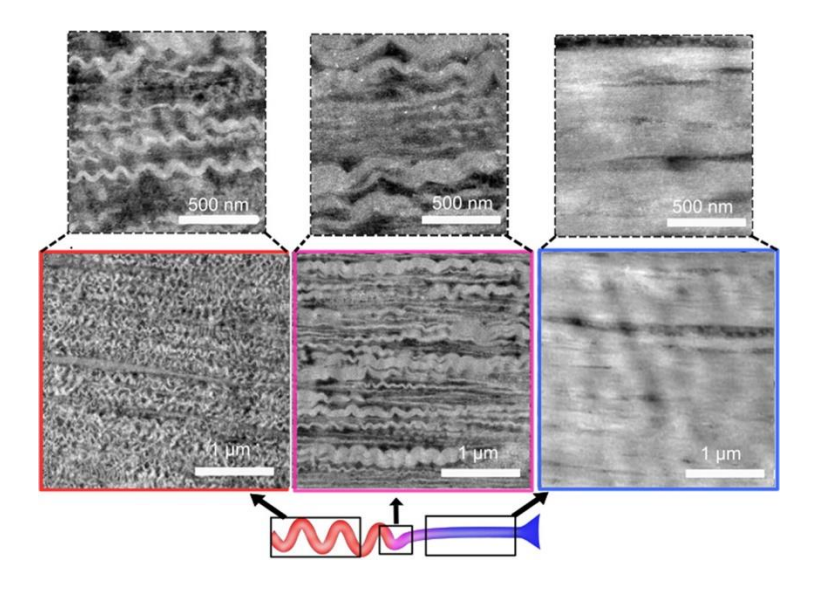


Figure 4.4. Ultrastructural analysis of byssal thread gradient structure. STEM images of the proximal (red), transition (purple), and distal (blue) regions of the byssus.

Tracking the Compositional Gradient in Byssus Using Confocal Raman Spectroscopy

While TEM reveals clear differences in the morphology of preCol nanofibrils within the proximal, distal and transition regions, it does not provide information about the composition of these different segments. Here, we utilized polarized confocal Raman spectroscopy to elucidate compositional variations across the transition region (Fig. 4.5 and Supporting Fig. S4.4). Polarization dependent Raman measurements of the proximal and distal thread performed with the polarizer oriented both parallel and perpendicular to the thread axis showed very little variation, indicating that observed differences in spectra along the thread arise largely from compositional differences and not differences in protein orientation (Supporting Fig. S 4.4a).³⁶ With regards to the amide I and amide III bands which reflect protein conformation, spectra acquired from the distal and proximal regions are mostly similar to one another with peak positions and profiles dominated by the collagen domain of the preCols (Fig. 4.5a).³⁶ However, there are several distinct differences in specific spectral regions that are unique to the distal and proximal regions. Taking molecular orientation into consideration, the proximal region shows more intense peaks at 1003 cm⁻¹, associated with phenylalanine³⁷ and in the region between 1570 -1620 cm⁻¹, possibly arising from the C=C stretching vibrations of rings in phenylalanine, histidine or tyrosine (Fig. 4.5a)^{37, 38}. These differences very likely reflect the different protein compositions of the distal and proximal threads - whereas the distal region was determined previously to be primarily comprised of preCol-D with lesser amount of preCol-NG and TMP-123, the proximal region is comprised primarily of preCol-P (66 %) and PTMP-1 (34%)8. Notably, preCol-P contains two-fold higher histidine content than preCol-D³⁹ and ptmp-1 has more than

twice the mol% of phenylalanine compared to any of the preCols²⁴ which is consistent with the observed peaks.

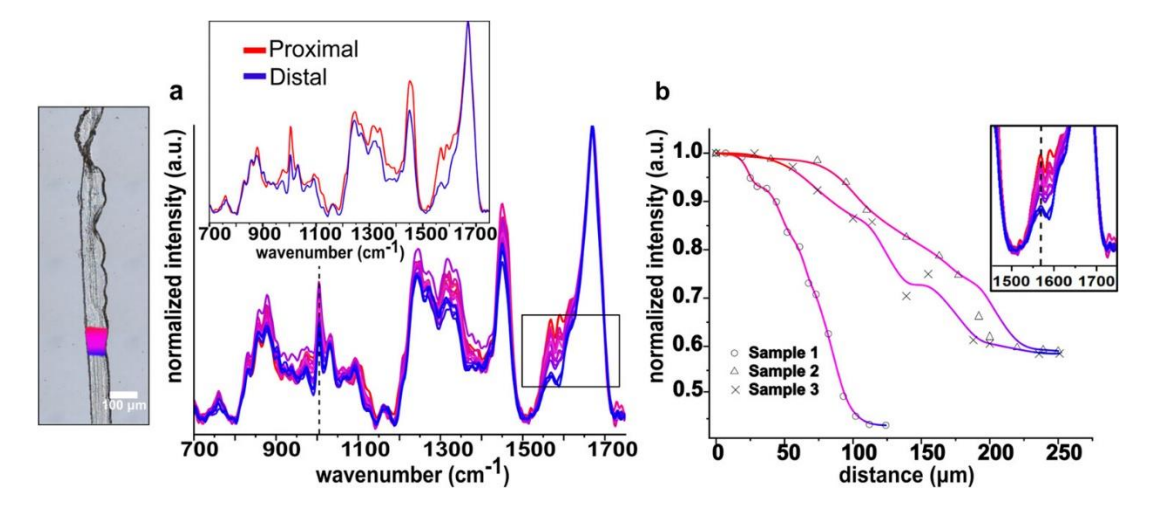


Figure 4.5. Confocal Raman spectroscopic mapping of the transition region of byssal threads (a) Raman spectra acquired from hyperspectral imaging across the transition region from proximal (red) to distal (blue). Thread photograph shows the imaged region with color matching where the same-colored spectra were acquired from. Spectra are normalized to the peak at 1670 cm⁻¹ present in amide I region. Clear differences are observed in the spectra, especially in the region from 1570 to 1590 cm⁻¹, which enables tracking of compositional changes across the interface.

(B) Plot of normalized peak intensity at 1570 cm⁻¹ (see inset) against distance across the transition region moving from the proximal to distal in three different threads, including data from panel (a). Spectra from the other two threads are found in Supporting Figure S4.4.

By performing confocal mapping across the entire transition region, we can track how spectra change as a function of position along the gradient with submicron-scale precision. Taking advantage of the distinct differences between the proximal and distal Raman spectra, we used the change in intensity of these characteristic peaks as a spectral marker for proximal-like vs.

distal-like composition (Fig. 4.5b). In all threads tested, the intensity of peaks indicative of the proximal region gradually decreased across the transition region, indicating a continuous gradual compositional change on the micron scale persisting over length of hundreds of microns. To plot the compositional change as a function of position, the peak intensities at 1570 cm⁻¹ for segments starting from the proximal to the distal region were normalized to the amide I peak intensity and plotted against distance along the thread (from the proximal to the distal side) (Fig. 4.5b, Supporting Fig. S 4.4b). It can be clearly seen that there is a continuous decrease in the intensity of this characteristic proximal peak across the entire transition region in all threads tested. However, similar to the mechanical gradient analysis, the length of the transition region varied between different threads. Although it was not possible to perform both Raman mapping and mechanical analysis on the same thread due to the necessity to cryosection threads for Raman measurements, we posit that the compositional and mechanical transition observed are correlated.

Spectroscopic Analysis of Distal and Proximal Thread Secretory Glands

Thus far, our analysis of the transition between the distal and proximal regions of byssal threads has revealed that the observed mechanical gradient arises from a continuous change in the protein composition occurring over hundreds of microns across the transition region, which is correlated with a concomitant transition in the nanofibrillar morphology. Here, we consider more closely how such a compositionally and structurally graded fiber might be formed with high spatial precision. Mussels produce each thread individually as a protein secretion into an elongated groove running along the ventral side of the foot secretory organ^{27, 40}. Surrounding the

groove are elongated glands that synthesize the byssal thread precursors and stockpile them in micron-scale secretory vesicles (Fig. 4.6a)^{27, 30, 41}. Here, we utilized confocal Raman spectroscopy to determine whether the compositional gradient present in native threads might originate in the storage of vesicles in the secretory tissue of the mussel. Spectra were collected from gland regions at the distal and proximal extremes of longitudinally cryo-sectioned mussel feet, revealing very strong similarities to the spectra acquired from the proximal and distal regions of the thread, respectively (Fig. 4.6a). Specifically, all spectra were dominated by conformational signals distinctive of collagen in the amide I and III bands; however, spectra collected from the proximal region of the core gland consistently exhibited higher intensity peaks in the characteristic regions identified above (1570-1620 cm⁻¹) and phenylalanine (1003 cm⁻¹).

Identification, purification, and assembly of core vesicle subpopulations

Raman spectroscopic investigation of the core gland suggests that the mussel stores different core proteins (e.g. preCol-D, preCol-P, PTMP-1) in different regions of the foot. However, currently, only one type of core vesicle has been identified in the foot which does not fit with the current observations. Moreover, the presence of non-byssal material in the foot section (e.g. cells, extracellular matrix, muscle) makes detailed characterization of these precursors challenging. Therefore, to reconcile the observation of different gland contents with the assumption that there is only one type of core vesicle^{30, 41}, we adapted a previously published method²⁸ for extracting and purifying the core secretory vesicles which contain these precursors in order to perform compositional analysis.

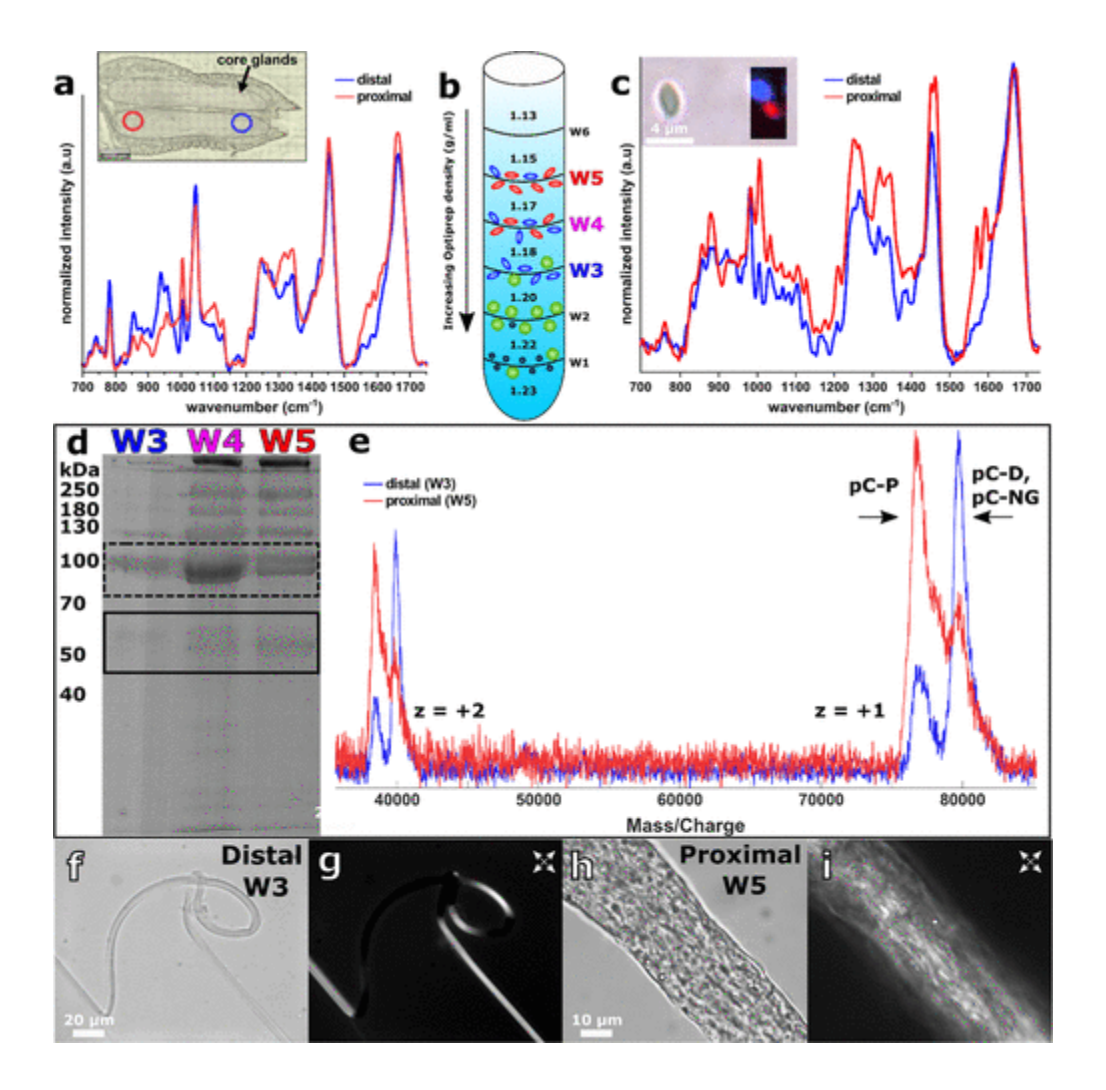


Figure 4.6.Biochemical characterization and assembly of precursor vesicles (a) Raman point scans from the core glands of a mussel foot section (inset). (b) Schematic representation of discontinuous density gradient fractions, with spheres representing plaque (green) or cuticle vesicles (black), and ellipses representing the distal (blue) or proximal (red) core vesicle subtypes. (c) Raman fingerprint of two representative vesicles obtained by purification. Inset shows a light microscopy image of vesicles from fraction W4 overlaid with a Raman map. (d) SDS-PAGE of purified fractions with variable distribution of preCol variants (dashed box) and potential matrix proteins (solid box). (e) MALDI-TOF spectra of purified fractions, with the most prominent peaks corresponding to singly and doubly charged ions of preCol variants. (f) Fiber drawn from distal

vesicle fractions (W3) have a smooth morphology and (g) high degree of alignment, demonstrated by polarized light microscopy (PLM, direction of slow and fast axis given by white arrows). (h) Fibers drawn from proximal vesicle are irregular with (i) a corrugated microstructure made visible by PLM.

Vesicle separation by density centrifugation was performed using a discontinuous density gradient of Optiprep with small step sizes (~20 mg/ml), producing 3 distinct fractions of core vesicles (W3, W4, & W5, Fig. 4.6b) which appeared morphologically similar using light microscopy. Comparing the Raman spectra of vesicles in these fractions reveals two distinct subpopulations, which strongly resemble the spectra acquired from the distal and proximal core glands, respectively, distinguished by the relative intensity of the previously mentioned characteristic peaks in the range of 1570-1590 cm⁻¹ (Fig. 4.6c). Notably, this spectral marker which is associated with proximal composition was unevenly distributed across the various fractions and was essentially absent in vesicles in the densest fraction (W3) of the gradient. Based on spectra acquired from the native thread (Fig. 4.5a) and the core glands (Fig. 4.6a), we posit that spheroidal vesicles lacking this marker contain distal precursors (e.g., preCol-D) while those displaying it contain proximal precursors (e.g., preCol-P, ptmp-1).

SDS-PAGE and MALDI-TOF mass spectrometry performed on the different vesicle fractions confirm the uneven distribution of preCol variants across the fractions with the smaller mass preCol-P (mass/charge ratio (m/z) 76750) lacking in fraction W3 and the larger preCol-D and preCol-NG found in reduced quantities in fraction W5 (m/z 79700) (Fig. 4.6d-e)⁷. Curiously, MALDI-TOF was unable to confirm whether the lower molecular weight bands visible on the gel

were the matrix proteins TMP-1 and PTMP-1 (~56 and 45 kDa, respectively), either because they failed to desorb or because their peaks are obscured by doubly charged preCol ions (Fig. 4.6e). While we can easily establish a minimum of two vesicle subpopulations (distal and proximal), the roughly even distribution of preCol variants in the intermediary fraction (W4) raises the possibility of individual vesicles containing a mixture of preCol-P, D, and NG. Even when the purification protocol is repeated using only distal foot tissue, 3 separate fractions are still obtained, all with similar distributions of preCols (Supporting Fig. S4.5). These findings suggest that the compositional gradients observed in the thread might originate from the secretion of different core vesicles localized in specific regions of the foot, but further work is required to determine whether there is a continuum of vesicle subtypes or whether their contents fall into discrete subpopulations.

Previous studies on purified preCols revealed that the solubilized proteins could be manually drawn into fibers, with assembly controlled through histidine deprotonation and extensional flow. 7,39 We replicated this process by lysing vesicles and raising the buffer pH above 6, creating thin (5 — 25 μ m), centimeter long fibers from a few microliters of vesicle suspension (Figure 4.6f-i). It is important to note here that in the earlier studies, preCols were purified from whole mussel feet in high purity, and were separated chromatographically from the matrix proteins, which is different from the current process in which all vesicle contents including the matrix proteins are solubilized. The fibers drawn from lysed distal vesicles (W3) are smooth and perfectly aligned along the fiber axis (Fig. 4.6f-g), resembling those obtained from purified preCols in previous studies 7,39 . In contrast, fibers drawn from proximal vesicles (W5) are much thicker, possess a

distinct corrugated microstructure and display weaker birefringence than their distal counterparts (Fig. 4.6h-i). While these structural features resemble those observed in the native proximal thread (Fig. 4.4), they are not found in fibers drawn from purified preCol-P in a previous study⁷, suggesting that the unique morphology of the proximal thread arises from the interaction of preCols with PTMP-1.

4.4. Discussion

Our findings indicate that mussels fabricate a continuous mechanically graded interface between the stiff distal and compliant proximal regions of the byssus biopolymer by mixing vesicles containing different preCol variants and specific matrix proteins in a controlled fashion. Previous studies have shown that the core protein precursors are stored within secretory vesicles as a smectic liquid crystal phase^{28, 30, 41, 42}, and that fluid vesicle contents will spontaneously coalesce and form fibrillar structure under appropriate conditions^{27, 28, 39}. The current work revealed that there are at least two different subtypes of core vesicles that contain different protein compositions. The different subtypes are apparently distributed throughout the core secretory glands such that vesicles enriched in proximal-specific proteins (i.e., preCol-P, PTMP-1) are stored at the proximal end of the gland and distal specific proteins (i.e., preCo—D), which is consistent with previous investigations^{8, 17, 24}.

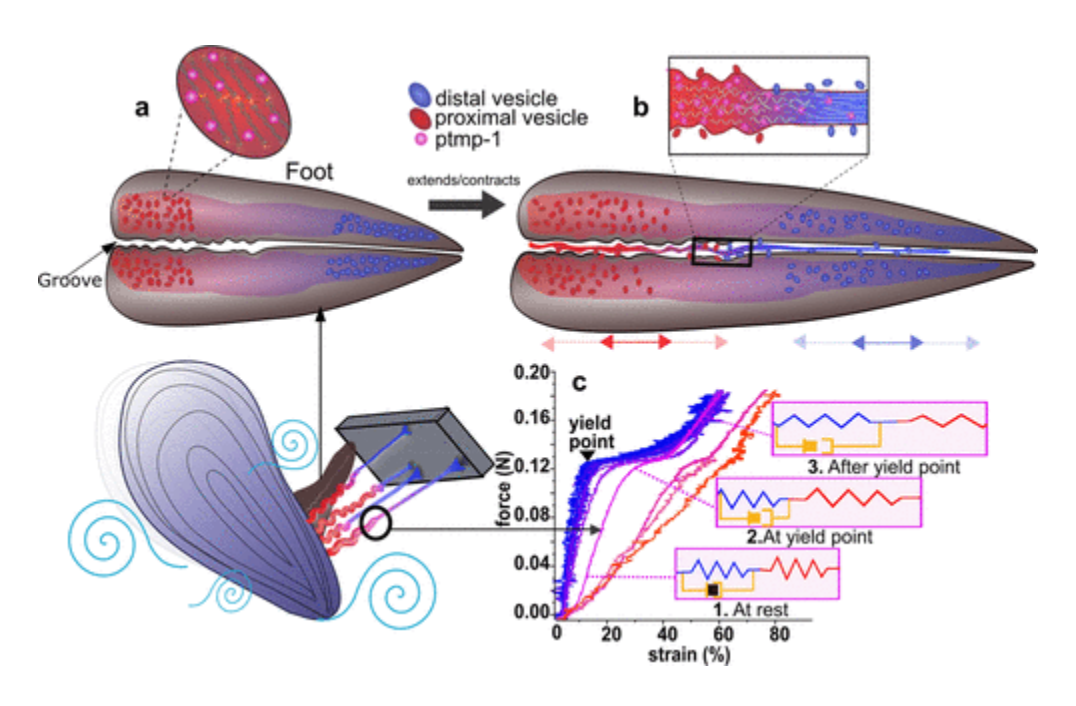


Figure 4.7.Model of byssal thread gradient formation and function. ((a) Schematic illustration of a mussel foot showing the localization of vesicles enriched in preCol-P (red) and preCol-D (blue) in core gland at proximal and distal ends of the foot before the mussel produces a thread. (b) Schematic illustrating how the proximal and distal ends of the core glands might independently extend during secretion of vesicles into the groove controlling the relative length of the proximal and distal thread regions in different threads. Mixing of proximal and distal vesicles at the interface between the two glands leads to self-assembly of a transition region that continuously changes in composition, structure and mechanics moving from one end to the other. (c) Schematic model of how molecular level mechanical response of different preCols might contribute to observed mechanical differences between the proximal, distal and transition regions. Flanking domains of preCol-D (represented by blue spring) initially resist deformation at low strain based on the presence of a strong sacrificial cross-link network mediated by histidinemetal cross-links (gold). Conversely, preCol-P flanking domains (red) based on elastin-like sequences extend easily even at low forces and initially provide the majority of deformation prior

to yield. During yield, the histidine-metal network fails, and load is transferred to the preCol-D flanking domains which then extend, allowing the distal thread to almost match the strain of the proximal region under the post-yield strains.

We posit that the transition region between the proximal and distal thread, which is comprised of a graded distribution of these different precursors, is formed spontaneously by mixing the contents of different vesicle subtypes during secretion based on their pre-organization in the secretory gland. At the nanoscale, this manifests as distinct fibrillar morphologies with the transition region consisting of a mixture of distal-like fibrous sheets and proximal-like wavy nanofibrils. Based on previous investigations^{25, 43, 44}, we hypothesize that PTMP-1 is responsible for producing characteristic wavy nanofibril morphology in both the proximal and transition regions. Previous studies with recombinant PTMP-1 suggest that the wavy morphology of the nanofibrils likely arises from the binding of von Willebrand factor type A domains of ptmp-1 to the collagen domains of preCols^{25, 43, 44}. Indeed, earlier studies showed that fibers formed from purified preCol-P in the absence of PTMP-1 possess a smooth fibrillar structure, even at the nanoscale⁷. However, it should be noted that the fibers formed from purified preCol-P were less stiff and more extensible than those produced from pure preCol-D⁷, suggesting that the mechanics of the proximal thread are influenced both by the native mechanics of preCol-P and the morphological changes induced by PTMP-1. Thus, by modulating the relative proportions of collagenous and collagen-binding components along the length of the fiber core via secretion of different vesicle subtypes, the mussel locally controls nanofibrillar morphology and mechanics.

In this way, the mussel fabricates a continuous mechanical gradient spanning over an order of magnitude stiffness from one end to the other.

Previous studies and the current work indicate that the distinctive mechanical behavior in the proximal and distal thread regions originates from the difference in the flanking domain sequence of preCol-D and -P^{7, 8, 15} and the matrix protein PTMP-1^{24, 25}. We present here a plausible model to explain how the various components work together at multiple length scales (Fig. 4. 7). Due to the presumed low stiffness of the elastin-like domains of preCol-P^{45, 46}, it is anticipated this will be the first component to extend under applied load on the whole thread. It seems probable that straightening of the wavy nanofibrils in the proximal and transition regions will also occur under this low force regime. As the elastin domains are stretched, forces will increase exponentially due to their entropic elastic-like deformation^{45, 46}, eventually reaching a critical level at which yield will occur in the distal region, which up to that point has not deformed much. Previous X-ray based studies indicate that at the distal thread yield point, histidine-metal coordination cross-links in the termini of preCols rupture, enabling the unfolding of cross beta sheet flanking domains allowing extension of the thread under essentially constant force 20, 47, 48. At the end of the yield plateau, further extension of the thread arises from essentially equal contributions of the distal and proximal regions by continued stretching of the flanking domains of all preCol variants. An interesting point to consider, is what happens in the transition region in which there is a mixture of distal and proximal like nanofibrils. Force-strain curves from transition segments exhibit an initial low stiffness region resembling a proximal response followed by a more distal-like stiff behavior, which indicates that the transition region mechanical behavior is

determined by the mixture of proximal and distal composition/structure indicated by Raman and STEM analysis.

One unanticipated finding of our study was that different threads possess very different gradients, in terms of the relative lengths of proximal, distal and transition regions. This is in contrast with a previous report from closely related mussel species (Mytilus californianus and Mytilus qalloprovincialis), which showed very little variation in the relative lengths of the proximal and distal regions between different threads¹¹. It was previously reported that *Mytilus edulis* threads are comprised 56% distal and 43% proximal based on analysis of seven threads (the authors provided mean values, but not standard deviation so interthread variation is unclear)⁴⁹. However, considering that analysis in these earlier studies was performed via visual or microscopic inspection of the threads based on morphological variation, it is not surprising that the transition region was excluded since this portion only becomes evident with more detailed analysis (e.g. video extensometry, confocal Raman, TEM). In any case, the inherent variability in the morphology and mechanical properties between threads (even when produced by the same mussel within a few minutes) is striking and begs the question of whether this might have a functional purpose and whether mussels might actively control the secretion process to create tailored gradients in the threads to control mechanical response of individual fibers (e.g., by extending the different regions of the foot by different proportions during thread formation (Fig. 4.7)). It is intriguing to imagine that the mussel might regulate thread gradient structure depending on specific factors in its habitat (e.g., water chemistry, temperature, substrate, local predation) or life history (e.g., age, position of thread in the byssus). At this point, we are unable

to answer this question conclusively; however, researchers might still draw inspiration from this hypothesis to create "bespoke" functionally graded polymer fibers and films.

4.5. Conclusion

Mechanical gradients are a biological strategy for mitigating stress concentrations at interfaces between components of mismatched mechanical stiffness and/or Poisson's ratio. Understanding how nature produces such functionally graded materials provides inspiration for how humans might produce advanced materials with potential technical and biomedical applications (e.g., as implant devices). The mussel byssus, in particular, provides inspiration for production of functionally grade polymer materials. Here, we clearly demonstrated that threads exhibit a continuous mechanical gradient extending from the soft proximal to stiff distal region on the scale of up to several hundreds of microns. This mechanical gradient is achieved through a gradient of nanofibrillar morphology, realized through variation in composition of different collagen precursor variants and matrix proteins at the nanoscale. The assembly of this complex hierarchical structure is achieved via secretion of at least two different subvariants of secretory vesicles containing different proteins mixtures and subsequent protein self-assembly. These findings provide further insights into how next generation functionally graded polymer materials can be fabricated. This is especially relevant given recent discoveries on the role of condensed liquid crystal preCol precursor phases in determining thread hierarchical structure ^{28, 30, 42}. Indeed, one could envision applying extracted concepts toward the instantaneous self-assembly of collagenous materials with tailored graded mechanical properties for applications in implants or tissue scaffolds for biomedical engineering.

4.6. Methods

Byssus Sample Preparation

Mussels, originating from Prince Edward Island, were purchased from the market and maintained in a tank at 12–15 °C with artificial seawater (Fluval Sea, USA; containing Ca, K, Mg and Sr). Mussels were attached to plexiglass using fishing line and rubber bands, where they start producing fresh threads within a few hours. After around 24 hours, the byssal threads produced were collected, placed in deionized water at 4 °C for direct use in various experiments. Foot tissue was dissected from mussels, directly embedded in a mold containing optimal cutting temperature (OCT) medium and frozen in liquid nitrogen-cooled isopentane. Following freezing, 3 μ m thick longitudinal sections were cut using a cryotome (Leica CM1520) at -20 °C.

Polarized Confocal Raman Spectroscopy

Confocal Raman spectroscopy was performed on hydrated $3\mu m$ thick thread sections which were cut using a cryotome at -23°C. Sections mounted on glass slides were placed on a motorized scanning stage (Witec Alpha300R, Ulm, Germany). A green laser (Nd/ YAG laser, λ = 532 nm) was focused by a confocal Raman microscope with a 50 x objective (Zeiss, NA = 0.75) to make individual point scans starting from the distal and ending in the proximal region. With laser power between 15-20 mW, single spectra were acquired by a thermoelectrically cooled CCD detector behind a 600-g/mm grating as a result of 120 accumulations and an integration time of 1 sec. Polarization effects were studied by varying the angles of polarized laser between 0°(perpendicular to fiber axis) and 90°(parallel to fiber axis). The collected data were analyzed using the ControlFIVE 5.1, WITec software. For the gradient profile plots measured on threads,

values were normalized according to the intensity of phenylalanine peak at 1003 cm⁻¹ and represented by the Sigmoidal -Boltzmann fit.

Using similar parameters Raman spectra were also obtained and analyzed on 5 µm thick sections of mussel feet and from purified vesicles. Single point measurements were collected from the proximal and distal sides of the core glands in foot tissue. Note that vesicles in the core gland of the foot are randomly oriented; thus, polarization dependent measurements were not relevant. Isolated vesicles were scanned in solution using a 100x oil-immersion objective (Zeiss, NA= 1.25) with a laser power of 10 mW and 10s integration per point. The Raman signal of the vesicles and that of the surrounding buffer were demixed using linear combinations of single spectra, a method built into the ControlFIVE software.

Mechanical Testing and Video Extensometry

Samples of various lengths were collected and fixed using cyanoacrylate glue (Henkel, LePage super-glue) at the opposite ends (proximal and distal side) of a window cut out from a waterproof paper. Once the glue was dry, the samples were stored for up to 2-3 days in water at 4°C. Samples were tested using tensile mechanical tester (CellScale UStretch) with a 0.5 N load cell, coupled with video extensometry using a camera with a ½" monochrome CCD sensor to obtain a resolution of 1280 pixels by 960 pixels.

In order to create contrast on the threads for video tracking, spots of acrylic paint were marked on threads with a distance that maximized the number of the drawn spots along the thread, while

not placing them too close for the video tracking software to differentiate as distinct features. Samples were loaded on the grips of the tester, immersed in water and stretched at an extension rate of 5 mm/min with a data output frequency of 5 Hz. The location of the paint spots and force were analyzed simultaneously using Ustretch (version 10.76) software, which relies on an image tracking engine based on a template matching algorithm (Supporting Fig. S4.1). The initial slopes of the force-strain curves below 20 % strain were fit and used as a measure of relative stiffness in each segment of the thread.

Scanning Transmission Electron Microscopy

Prior to STEM imaging, byssal thread samples were fixed and embedded for optimal contrast. Distal, transition, and proximal regions were cut from individual threads and fixed for 1 h at 4 °C in a buffer solution containing 2.5 % glutaraldehyde (Sigma Aldrich, 25 % solution), 1.5 % paraformaldehyde (formaldehyde diethyl acetal, Sigma Aldrich, 99 %) and 0.1 M cacodylate buffer, pH 7.4 (sodium cacodylate trihydrate, Sigma Aldrich). The samples were rinsed with 0.1 M cacodylate buffer having a pH of 7.4 for 3 x 10 min at 4 °C. They were subsequently treated with 1 % osmium tetroxide in water for 1 h at 4 °C, rinsed with distilled water for 3 x 5 min at 4 °C and dehydrated in ethanol of (50, 70, 90, 3 x 100 % for 10 min each step). Finally, samples were embedded in Epon resin at room temperature and polymerized at 65 °C for 48 h.

Sample sections of 70-80 nm were obtained using an ultramicrotome and mounted on carbon coated Cu grids. To determine the structural motifs of thread tissues at the nanoscale, scanning transmission electron microscopy (STEM) images were acquired with a Thermo Scientific Talos F200X G2 S/TEM equipped with a Ceta 16 M CMOS Camera, operated at 200 kV acceleration

voltage. STEM mode was used for high angle annular dark-field imaging at magnifications of 16500×, 46000×, 66000×, 130000×, and 185000×.

Vesicle extraction & purification

To separate the entire core vesicle population into subpopulations, we adapted a previously published density gradient centrifugation protocol²⁸. Briefly, the outer pigment and muscle lining of the foot was removed, leaving only glandular tissue which was then homogenized at a ratio of 0.5g of tissue to 5mL of 150mM citrate-phosphate buffer (pH 5.5) containing 500mM sucrose, 150mM EDTA, and 5mM ascorbic acid. The homogenate was filtered through a 0.5mm stainless steel mesh and 40 μm cell strainer and mixed 1:1 with homogenization buffer containing 30% iodixanol (Optiprep, Sigma). The homogenate solution was then layered on top of a discontinuous density gradient (30/27.5/25/22.5/20/17.5% Optiprep) and fractionated by centrifugation in an Eppendorf A-4-44 swinging bucket rotor for 200 minutes at 4000 x g, 4 °C. Three of the collected gradient interfaces contained core vesicles and will be hereby referred to as W3 (25/22.5% interface), W4 (22.5/20%), and W5 (20/17.5%).

Sodium dodecyl sulfate-polyacrylamide gel electrophoresis (SDS-PAGE)

Purified vesicle fractions were mixed 3:1 with 4X Laemmli sample buffer, sonicated for 5 minutes, and heated at 90 °C for 5 minutes. The contents of the lysed vesicles were then run on a discontinuous 10% mini-SDS gel using the Laemmli tris-glycinate electrode buffer system. Bands were visualized by staining the gel with Coomassie Blue R-250 (Bio-Rad) for 3 hours.

Matrix-assisted laser desorption ionization (MALDI) mass spectrometry

The mass of the proteins contained within the purified vesicle fractions was assessed by MALDI mass spectrometry with time-of-flight detection (MALDI-TOF) using a Bruker Autoflex III Smart Beam model (Bruker, Billerica, MA) in linear positive acquisition mode. Vesicles were mixed 1:1 with fresh homogenization buffer, pelleted by centrifugation at 15,000xg for 15 minutes, and resuspended in 50/49.9/0.1% acetonitrile/water/TFA; 1μ L of this mixture was spotted onto a MALDI target plate, air dried for 5 minutes, overlayed with a 1μ L drop of matrix solution (20mg/mL sinapinic acid in 50/49.9/0.1% acetonitrile/water/TFA), and air dried for another 5 minutes before irradiating the sample spot with a UV laser (Nd:YAG, λ = 355 nm) set to a pulse width of 5ns and variable frequency (maximum 200 Hz). A 20 kV acceleration voltage was used to propel singly and doubly charged peptides through the TOF detector.

Fiber formation

To obtain the fibers shown in Figure 4.6, 10 µl of purified vesicle suspension was dropped onto double-sided carbon tape (EMS, other hydrophobic surfaces such as uncoated PTFE also work), mixed 1:8 with 10mM MOPS buffer (pH 8.0) and left to rest for 10-20 minutes. Proteins fibers were drawn by touching stainless steel forceps to the liquid surface and slowly pulling away, as demonstrated previously. 7, 39 This assembly process also functioned when tested with Tris or phosphate buffers, and with non-metallic probes, such a plastic pipet tips. Although extremely short, fragile fibers can be obtained by rupturing the vesicles in pure water, the longest, most resilient fibers were obtained when lysed vesicles were above pH 6.1. Hydrated fibers were

imaged using a cross-polarized light microscope (Axio Scope.A1, Zeiss) equipped with a 6-megapixel CCD camera (Axiocam 505 color, Zeiss).

4.7. Acknowledgements

We thank A. Wahba of the McGill Chemistry Characterization (MC2) Facility for assistance with MALDI-TOF measurements and the staff at the Facility for Electron Microscopy Research (FEMR) for their support. M.J.H. acknowledges support from an NSERC Discovery Grant (RGPIN-2018-05243) and FRQNT Équipe grant (284991). L.Y. acknowledges support from an FRQNT Québec Merit fellowship.

4.8. References

- (1) Wellman, S. M.; Eles, J. R.; Ludwig, K. A.; Seymour, J. P.; Michelson, N. J.; McFadden, W. E.; Vazquez, A. L.; Kozai, T. D. Y., A Materials Roadmap to Functional Neural Interface Design. *Advanced Functional Materials* 2018, *28*, 1701269.
- (2) Gao, S.-S.; Zhang, Y.-R.; Zhu, Z.-L.; Yu, H.-Y., Micromotions and Combined Damages at the Dental Implant/Bone Interface. *International Journal of Oral Science* 2012, *4*, 182-188.
- (3) Waite, J. H.; Lichtenegger, H. C.; Stucky, G. D.; Hansma, P., Exploring Molecular and Mechanical Gradients in Structural Bioscaffolds. *Biochemistry* 2004, *43*, 7653-62.
- (4) Liu, Z.; Meyers, M. A.; Zhang, Z.; Ritchie, R. O., Functional Gradients and Heterogeneities in Biological Materials: Design Principles, Functions, and Bioinspired Applications. *Progress in Materials Science* 2017, *88*, 467-498.

- (5) Gong, S.; Yap, L. W.; Zhu, B.; Cheng, W., Multiscale Soft—Hard Interface Design for Flexible Hybrid Electronics. *Advanced Materials* 2020, *32*, 1902278.
- (6) Miserez, A.; Schneberk, T.; Sun, C.; Zok, F. W.; Waite, J. H., The Transition from Stiff to Compliant Materials in Squid Beaks. *Science* 2008, *319*, 1816-1819.
- (7) Harrington, M. J.; Waite, J. H., How Nature Modulates a Fiber's Mechanical Properties: Mechanically Distinct Fibers Drawn from Natural Mesogenic Block Copolymer Variants. *Advanced Materials* 2009, *21*, 440-444.
- (8) Waite, J.; Vaccaro, E.; Sun, C.; Lucas, J., Elastomeric Gradients: A Hedge against Stress Concentration in Marine Holdfasts? *Philosophical transactions of the Royal Society of London. Series B, Biological sciences* 2002, *357* 143-153.
- (9) Claussen, K. U.; Lintz, E. S.; Giesa, R.; Schmidt, H.-W.; Scheibel, T., Protein Gradient Films of Fibroin and Gelatine. *Macromolecular Bioscience* 2013, *13*, 1396-1403.
- (10) Claussen, K. U.; Scheibel, T.; Schmidt, H.-W.; Giesa, R., Polymer Gradient Materials: Can Nature Teach Us New Tricks? *Macromolecular Materials and Engineering* 2012, *297*, 938-957.
- (11) Bell, E.; Gosline, J., Mechanical Design of Mussel Byssus: Material Yield Enhances Attachment Strength. *J Exp Biol* 1996, *199*, 1005-17.
- (12) Carrington, E.; Waite, J. H.; Sara, G.; Sebens, K. P., Mussels as a Model System for Integrative Ecomechanics. *Annual Review of Marine Science* 2015, 7, 443-469.
- (13) Carrington, E.; Gosline, J., Mechanical Design of Mussel Byssus: Load Cycle and Strain Rate Dependence. *Amer.Malacol.Bull.* 2004, *18*, 135-142.

- (14) Hagenau, A.; Scheidt, H. A.; Serpell, L.; Huster, D.; Scheibel, T., Structural Analysis of Proteinaceous Components in Byssal Threads of the Mussel Mytilus Galloprovincialis. *Macromolecular Bioscience* 2009, *9*, 162-168.
- (15) Coyne, K. J.; Qin, X.-X.; Waite, J. H., Extensible Collagen in Mussel Byssus: A Natural Block Copolymer. *Science* 1997, *277*, 1830-1832.
- (16) Qin, X.-X.; Waite, J. H., A Potential Mediator of Collagenous Block Copolymer Gradients in Mussel Byssal Threads. *Proceedings of the National Academy of Sciences* 1998, *95*, 10517-10522.
- (17) Qin, X. X.; Waite, J. H., Exotic Collagen Gradients in the Byssus of the Mussel Mytilus-Edulis. *Journal Of Experimental Biology* 1995, *198*, 633-644.
- (18) Waite, J. H.; Qin, X.-X.; Coyne, K. J., The Peculiar Collagens of Mussel Byssus. *Matrix Biol.* 1998, *17*, 93-106.
- (19) Hagenau, A.; Papadopoulos, P.; Kremer, F.; Scheibel, T., Mussel Collagen Molecules with Silk-Like Domains as Load-Bearing Elements in Distal Byssal Threads. *J Struct Biol* 2011, *175*, 339-47.
- (20) Reinecke, A.; Bertinetti, L.; Fratzl, P.; Harrington, M. J., Cooperative Behavior of a Sacrificial Bond Network and Elastic Framework in Providing Self-Healing Capacity in Mussel Byssal Threads. *Journal of Structural Biology* 2017, *196*, 329-339.
- (21) Qin, X. X.; Coyne, K. J.; Waite, J. H., Tough Tendons Mussel Byssus Has Collagen with Silk-Like Domains. *J. Biol. Chem.* 1997, *272*, 32623-32627.
- (22) Arnold, A. A.; Byette, F.; Seguin-Heine, M. O.; LeBlanc, A.; Sleno, L.; Tremblay, R.; Pellerin, C.; Marcotte, I., Solid-State Nmr Structure Determination of Whole Anchoring Threads from the Blue Mussel *Mytilus Edulis*. *Biomacromolecules* 2013, *14*, 132-141.

- (23) Sagert, J.; Waite, J. H., Hyperunstable Matrix Proteins in the Byssus of Mytilus Galloprovincialis. *J Exp Biol* 2009, *212*, 2224-36.
- (24) Sun, C.; Lucas, J. M.; Waite, J. H., Collagen-Binding Matrix Proteins from Elastomeric Extraorganismic Byssal Fibers. *Biomacromolecules* 2002, *3*, 1240-1248.
- (25) Suhre, M. H.; Gertz, M.; Steegborn, C.; Scheibel, T., Structural and Functional Features of a Collagen-Binding Matrix Protein from the Mussel Byssus. *Nat Commun* 2014, *5*, 3392.
- (26) Waite, J. H.; Vaccaro, E.; Sun, C. J.; Lucas, J. M., Elastomeric Gradients: A Hedge against Stress Concentration in Marine Holdfasts? *Philosophical Transactions of the Royal Society of London Series B- Biological Sciences* 2002, *357*, 143-153.
- (27) Priemel, T.; Degtyar, E.; Dean, M. N.; Harrington, M. J., Rapid Self-Assembly of Complex Biomolecular Architectures During Mussel Byssus Biofabrication. *Nature Communications* 2017, *8*, 14539.
- (28) Renner-Rao, M.; Clark, M.; Harrington, M. J., Fiber Formation from Liquid Crystalline Collagen Vesicles Isolated from Mussels. *Langmuir* 2019, *35*, 15992-16001.
- (29) Trapaidze, A.; D'Antuono, M.; Fratzl, P.; Harrington, M. J., Exploring Mussel Byssus Fabrication with Peptide-Polymer Hybrids: Role of Ph and Metal Coordination in Self-Assembly and Mechanics of Histidine-Rich Domains. *European Polymer Journal* 2018, *109*, 229-236.
- (30) Jehle, F.; Priemel, T.; Strauss, M.; Fratzl, P.; Bertinetti, L.; Harrington, M. J., Collagen Pentablock Copolymers Form Smectic Liquid Crystals as Precursors for Mussel Byssus Fabrication.

 ACS Nano 2021, 15, 6829-6838.

- (31) Harrington, M. J.; Waite, J. H., Holdfast Heroics: Comparing the Molecular and Mechanical Properties of Mytilus Californianus Byssal Threads. *Journal of Experimental Biology* 2007, *210*, 4307-4318.
- (32) Aldred, N.; Wills, T.; Williams, D. N.; Clare, A. S., Tensile and Dynamic Mechanical Analysis of the Distal Portion of Mussel (Mytilus Edulis) Byssal Threads. *Journal of the Royal Society Interface* 2007, *4*, 1159-1167.
- (33) Qin, Z.; Buehler, M. J., Impact Tolerance in Mussel Thread Networks by Heterogeneous Material Distribution. *Nature Communications* 2013, *4*, 2187.
- (34) Vitellaro-Zuccarello, L.; De Biasi, S.; Bairati, A., The Ultrastructure of the Byssal Apparatus of a Mussel. V. Localization of Collagenic and Elastic Components in the Threads. *Tissue and Cell* 1983, *15*, 547-554.
- (35) Franchi, M.; Raspanti, M.; Dell'Orbo, C.; Quaranta, M.; De Pasquale, V.; Ottani, V.; Ruggeri, A., Different Crimp Patterns in Collagen Fibrils Relate to the Subfibrillar Arrangement. *Connective Tissue Research* 2008, *49*, 85-91.
- (36) Galvis, L.; Dunlop, J. W.; Duda, G.; Fratzl, P.; Masic, A., Polarized Raman Anisotropic Response of Collagen in Tendon: Towards 3d Orientation Mapping of Collagen in Tissues. *PLoS One* 2013, *8*, e63518.
- (37) Movasaghi, Z.; Rehman, S.; Rehman, I. U., Raman Spectroscopy of Biological Tissues. Applied Spectroscopy Reviews 2007, 42, 493-541.
- (38) Takeuchi, H., Raman Structural Markers of Tryptophan and Histidine Side Chains in Proteins. *Biopolymers* 2003, *72*, 305-317.

- (39) Harrington, M. J.; Waite, J. H., Ph-Dependent Locking of Giant Mesogens in Fibers Drawn from Mussel Byssal Collagens. *Biomacromolecules* 2008, *9*, 1480-1486.
- (40) Waite, J. H., The Formation of Mussel Byssus: Anatomy of a Natural Manufacturing Process. *Results Probl. Cell. Differ.* 1992, *19*, 27-54.
- (41) Vitellaro-Zuccarello, L., The Collagen Gland of *Mytilus Galloprovincialis*: An Ultrastructural and Cytochemical Study on Secretory Granules. *Journal of Ultrastructure Research* 1980, *73*, 135-147.
- (42) Hassenkam, T.; Gutsmann, T.; Hansma, P.; Sagert, J.; Waite, J. H., Giant Bent-Core Mesogens in the Thread Forming Process of Marine Mussels. *Biomacromolecules* 2004, *5*, 1351-1354.
- (43) Golser, A. V.; Scheibel, T., Routes Towards Novel Collagen-Like Biomaterials. *Fibers* 2018, 6, 21.
- (44) Yoo, H. Y.; Huang, J.; Li, L.; Foo, M.; Zeng, H.; Hwang, D. S., Nanomechanical Contribution of Collagen and Von Willebrand Factor a in Marine Underwater Adhesion and Its Implication for Collagen Manipulation. *Biomacromolecules* 2016, *17*, 946-953.
- (45) Urry, D. W.; Hugel, T.; Seitz, M.; Gaub, H. E.; Sheiba, L.; Dea, J.; Xu, J.; Parker, T., Elastin: A Representative Ideal Protein Elastomer. *Philos Trans R Soc Lond B Biol Sci* 2002, *357*, 169-84.
- (46) Baldock, C.; Oberhauser, A. F.; Ma, L.; Lammie, D.; Siegler, V.; Mithieux, S. M.; Tu, Y.; Chow, J. Y. H.; Suleman, F.; Malfois, M., et al., Shape of Tropoelastin, the Highly Extensible Protein That Controls Human Tissue Elasticity. *Proceedings of the National Academy of Sciences* 2011, 108, 4322-4327.

- (47) Krauss, S.; Metzger, T. H.; Fratzl, P.; Harrington, M. J., Self-Repair of a Biological Fiber Guided by an Ordered Elastic Framework. *Biomacromolecules* 2013, *14*, 1520-1528.
- (48) Schmitt, C. N. Z.; Politi, Y.; Reinecke, A.; Harrington, M. J., Role of Sacrificial Protein-Metal Bond Exchange in Mussel Byssal Thread Self-Healing. *Biomacromolecules* 2015, *16*, 2852-2861.
- (49) Mascolo, J. M.; Waite, J. H., Protein Gradients in Byssal Threads of Some Marine Bivalve Molluscs. *Journal of Experimental Zoology* 1986, *240*, 1-7.

4.9. Supplementary Materials

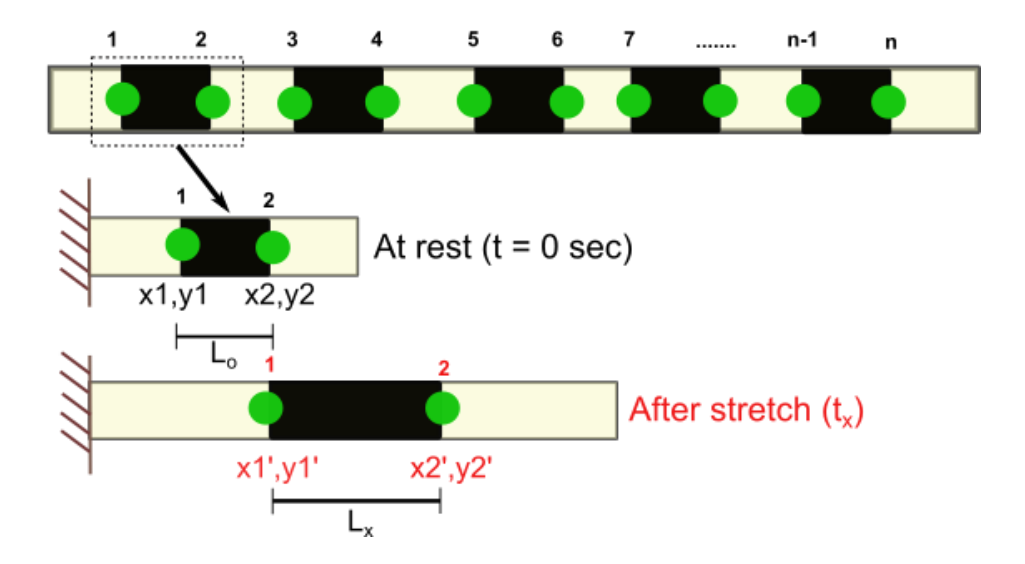


Figure S 4.7-1.Image tracking tool to determine the strain of individual segments comprising a thread as a function of time and applied force. Green dots represent our target source points for image tracking of each segment defined by the black paint spot on the thread. The image tracking tool in the UStretch software is based on a template matching algorithm. It defines a "patch" of pixels surrounding a selected source point and determines the optimal location of this point within a specified search region in each frame of the video. Our target source points were set at the interfaces between the acrylic black paint spots and the bare thread. Once the thread is stretched, the software will record the (x,y) coordinates of each point at each time point and match it to the force applied by the load cell on a thread (N) at that time. To calculate the strain of a small segment between 2 points (e.g., points 1 and 2 at time x), the initial length (L_0) between x1,y1 and x2,y2 at time point 0 and the final length (L_x) between x1',y1' and x2',y2' at time x are determined. Then, the strain at time x for an individual segment is calculated using the formula:

Strain % =
$$\frac{Lx - Lo}{Lo}x$$
 100

This strain is automatically calculated for each segment at each frame (time point) in the video.

Further considerations in extensometry experiments

The strain tracking feature in the software uses an algorithm which defines a "patch" of pixels surrounding the individual green points we marked on the source image (Fig. S4.1). This patch must be precisely marked at the interface between the edge of the black paint and the yellowish byssal thread because the software can only track the movement of pixels set between backgrounds displaying high contrast. Ideally, the patch of pixels being tracked should move uniformly in the direction of the applied load, reflecting the directionality of strain. However, there are certain artifacts that emerge that create challenges to perfectly track the patch, which results in noise in the signal (e.g., giving the appearance that strain is slightly oscillating. For example, since the thread is thin and the shape of the black paint spot on the surface deforms as it gets stretched along with the thread, two limitations are encountered here: 1) not having a high enough number of pixels in the patch to be used as the 'search region', which results in the software losing track of the green point as the images changes with time, and 2) changes in the contrast around the defined patch between the interface of black and white background on the thread because the black paint deforms and spreads once stretched. The two effects were minimized as much as possible respectively by 1) maximizing the number of pixels, while remaining on the thread, by altering the dimensions in the Source Template and Search Region in the software, and 2) carefully marking a fresh thread with paint using a fine pin to create clear borders at interface and then immersing the thread in a bath such that the water level is covering only the surface of a thread. Nonetheless, many samples still exhibit noise in the strain signal due to these artifacts.

An additional point to consider in these experiments is the actual strain rate experienced by different regions of the whole byssal thread. A characteristic feature of the byssal thread is that the material stiffness is different between the distal and proximal regions and gradually changes within the transition region resulting in different extensions of these different regions under the same applied load. This means that in an extension rate-controlled experiment, the actual strain rate experienced will vary in the different regions of the thread at any given time point. This is relevant because byssal threads are viscoelastic^{1, 2}, and the actual stiffness and overall mechanical response will vary depending on strain rate. Taking the force-strain curve in Figure 4.2c of the main text as an extreme example, the maximum difference in strain observed between the distal and proximal thread occurs in the lower force range prior to the distal yield point. In this case, during the same time period, the distal most portion stretches approximately from 0-4% strain while the proximal-most region stretches approximately from 0-80% strain, resulting in a roughly 20-fold difference in the strain-rate experienced by these two portions during this time period (simplifying to linear mechanical behavior). Interestingly, after the distal yield point occurs, the strain rates become closer to one another. Moreover, because of the viscoelastic nature of the threads, stretching them at slower or faster extension rates in another set of experiments might result in different relative strain responses of the distal and proximal threads, which would alter the relative strain rates experienced by the thread further.

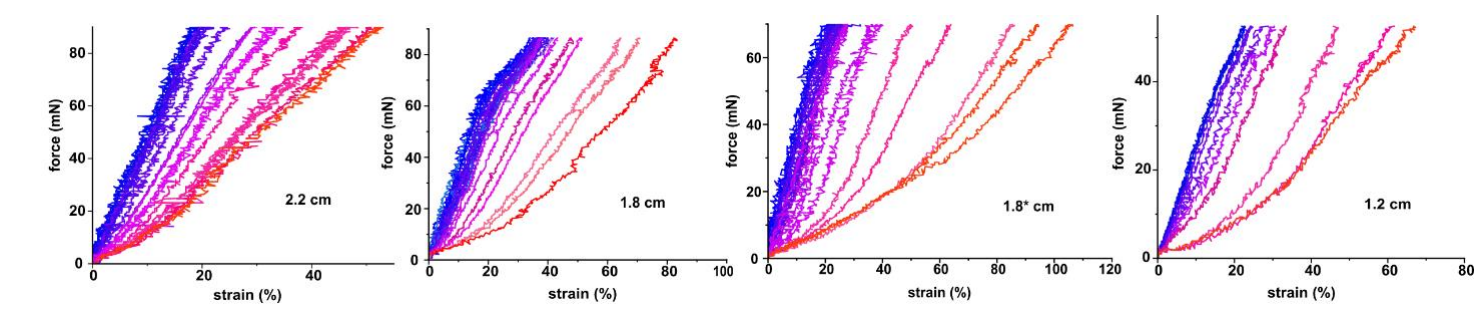


Figure S 4.7-2.Real-time mechanical response of different segments from four threads acquired from a single mussel (data from Figure 3.3 in the manuscript). Each thread was acquired from a single byssus taken from the same mussel, indicating that they were all produced in a short time window (around 24 hours). Strain data was acquired from video extensometry analysis during tensile testing for each thread as described in Supporting Fig. S4.1. Thread length is included on the side of each plot. Despite being from the same byssus, threads present different gradient behavior.

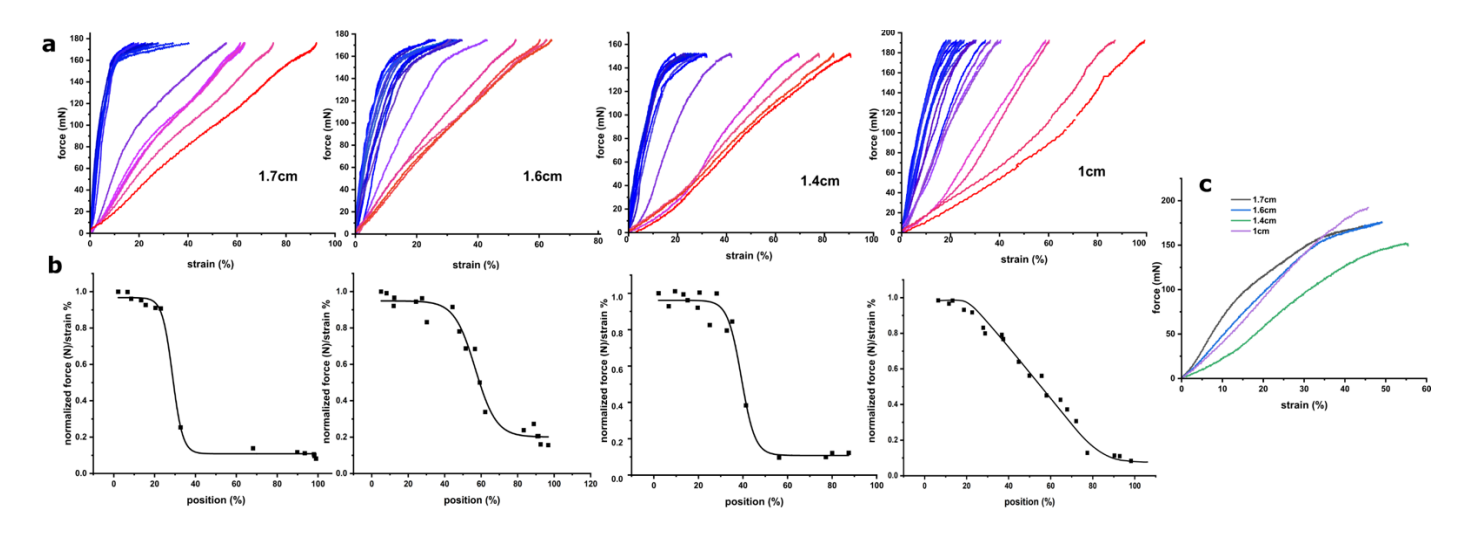


Figure S 4.7-3. Additional real-time mechanical response plots of different threads acquired from another mussel. a) Force versus strain plots for individual segments of threads of different lengths acquired from the same mussel byssus. b) Stiffness profiles along the length of different threads corresponding to the 4 threads in panel (a). c) The whole thread mechanical behavior of each thread from panel (a).

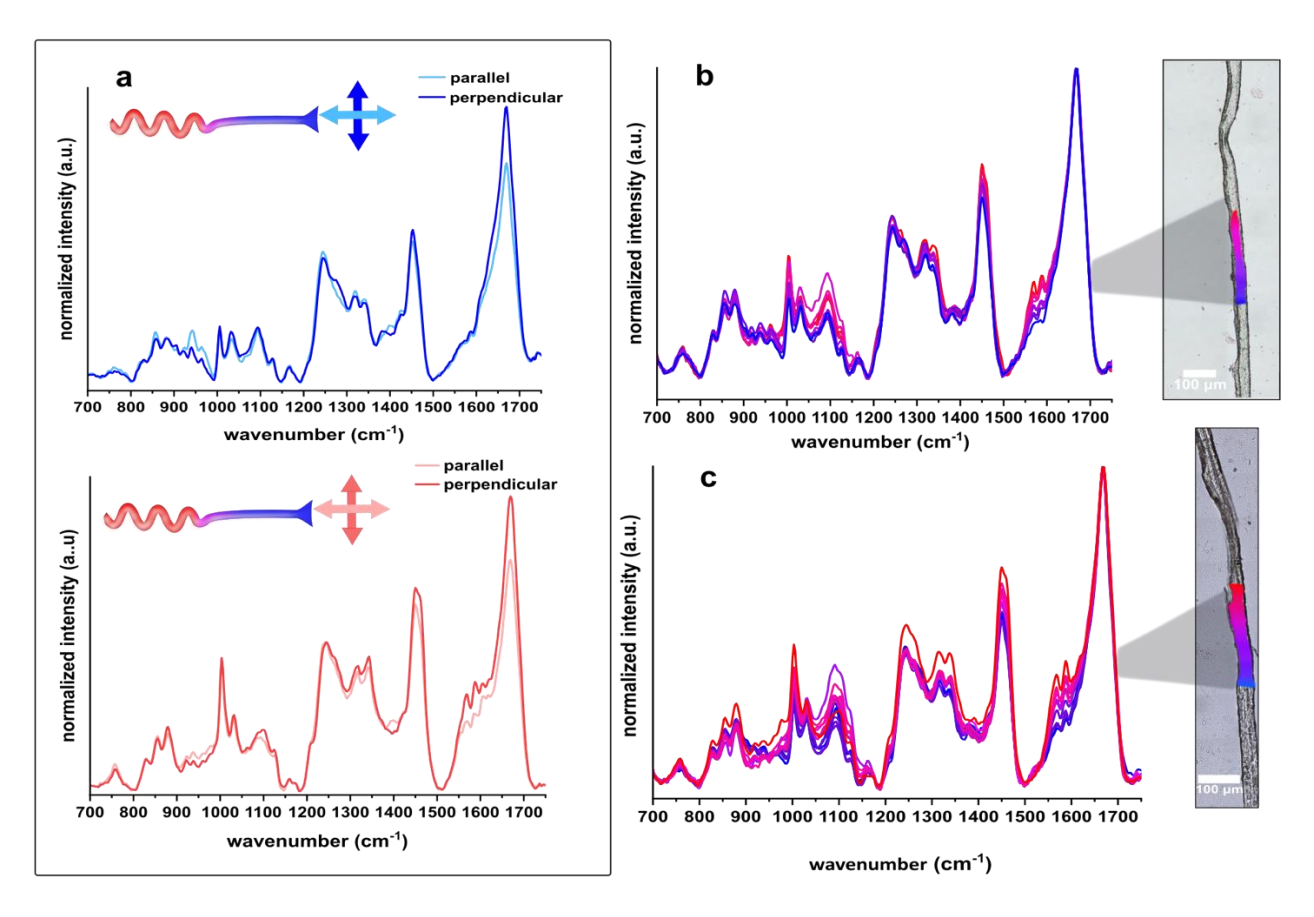


Figure S 4.7-4. Confocal Raman spectroscopy of byssal threads. a) Polarization dependent measurements on the distal (top – blue) and proximal (bottom – red) regions using a laser that is oriented 0°(perpendicular) or 90°(parallel) to the fiber axis. Spectra were normalized to the peak at 1003 cm⁻¹ corresponding to phenylalanine since it is expected to be isotropically oriented. b and c) Raman spectra acquired from hyperspectral imaging across the transition region from proximal (red) to distal (blue) of two different threads. Thread photographs show the imaged region, with color matching where the same-colored spectra were acquired from. Spectra are normalized to the peak at 1670 cm⁻¹ present in Amide I region. Tracking of the intensity of the peak at 1570 cm⁻¹ is plotted in Fig. 4.5b in the main manuscript.

While classical Raman spectroscopy primarily provides information about the chemical composition, polarized Raman spectroscopy can be used to acquire additional information about the anisotropic orientation of specific chemical bonds due to the tensorial nature of bond polarizability. In Supporting Fig. S4.3a, we measure the polarization dependence of the amide I band corresponding to vibrations of the C=O group of the protein backbone, showing only a small polarization dependence, allowing us to track compositional change while essentially overlooking orientation effects.

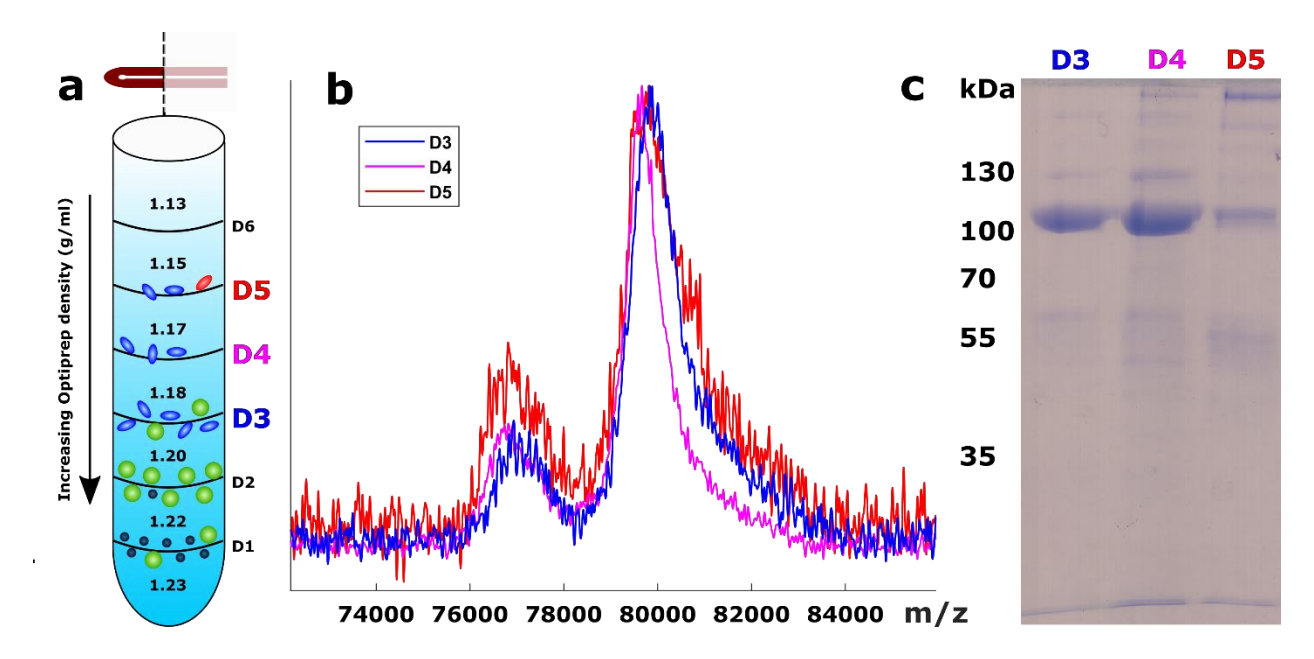


Figure S 4.7-5. Purification using only distal tissue. a) The purification protocol was repeated using the distal half of mussel feet, yielding 3 layers containing core vesicles. b) MALDI of these fractions reveal similar distributions of preCols (peaks normalized to highest value). c) SDS-PAGE confirms that all 3 layers contain very little preCol-P.

Supporting Movie S4.1. Video extensometry of a whole byssal thread. Video recorded of a whole byssal thread being stretched in water using a Ustretch tensile tester. Black spots are acrylic paint added to the thread before the experiment. The software tracks the movement of pixels associated with the interface between the painted and unpainted thread, as indicated by the green spots in the video.

References

- (1) Aldred, N.; Wills, T.; Williams, D. N.; Clare, A. S., Tensile and Dynamic Mechanical Analysis of the Distal Portion of Mussel (Mytilus Edulis) Byssal Threads. *Journal of the Royal Society Interface* 2007, *4*, 1159-1167.
- (2) Reinecke, A.; Bertinetti, L.; Fratzl, P.; Harrington, M. J., Cooperative Behavior of a Sacrificial Bond Network and Elastic Framework in Providing Self-Healing Capacity in Mussel Byssal Threads. *Journal of Structural Biology* 2017, *196*, 329-339.

5. Comprehensive Discussion

Natural materials exhibit remarkable mechanical properties by precisely controlling their composition and structure at interfaces to fulfill various survival needs⁷⁷. In addition to these properties, living organisms possess the ability to actively respond to external stimuli, which play a key role in guiding the assembly of basic molecular building blocks into complex hierarchically structured materials ³³. Nevertheless, synthetic biomimetic materials often fail to match the performance of their natural counterparts, despite natural materials being made from a limited set of building blocks ³³. This disparity highlights the need to further investigate the processes that allow organism to outperform, with a particular focus in this thesis on the Mytilus edulis mussels. Particularly, I explored the function of a high-performance byssus, which exhibits responsive adhesion at the living-nonliving interface and addresses mismatches at soft-hard interfaces. From this research, two overarching themes have emerged for deeper exploration: *i*) the design of dynamic biointerfaces, as discussed in Chapter 2 and 3 of this work, and *ii*) the development of "bespoke" graded polymers based on the proximal-distal gradient mentioned in Chapter 4.

i) Dynamic biointerface design :

With the restricted regenerative capacity of tissues in living-beings, interdisciplinary medical sciences in the last decades have made efforts to replace damaged tissues, restore lost functions, and continually bridge permanently emerging damages³³. One promising approach involves the integration of hard devices such as brain machine interfaces, prostheses to restore vision and hearing, and dental implants with the impaired soft tissues³³. Yet, this poses great design

challenges due the mechanical mismatch between the soft and hard materials, in addition to the complexities the devices can bring upon to soft tissue, such as inflammation and dissociation, once removal becomes necessary^{8,16}. Engineers have not yet come up with solutions to overcome these problems³, nor have there been reported in nature designs capable of mitigating interfacial stress and facilitating the release of devices. Here, we highlight a model system in mussels that relies on the dynamic response of cilia to modulate the interfacial strength with the non-living stem root. In particular, the cilia are in close contact with the discovered MSP-1 protein in the OLL, which undergoes structural changes under applied forces. To speculate on the significance of the activation of cilia and the structural changes of MSP-1 in relation to stem release, I will consider in the next paragraphs how one influences the other.

Many aquatic and terrestrial animals have evolved temporary adhesive systems including glues, suction organs, and miniature adhesive contacts to actively attach and detach during locomotion⁷⁸. Yet, these system have limited dynamic control⁷⁸. In fact, the most dynamic regulation of adhesion is observed in systems relying on interfacial forces, such as van der Waals interactions, since the detachment cycle neither requires chemical release agents, nor muscular action to neutralize pressure gradients (as for suction)⁷⁸. For instance, geckos use their pads to create attachment and detachment using millions of tiny hair-like structures called setae on their toes ⁷⁹. When the setae touch a surface, they make very close contact, allowing weak molecular forces to stick them to the surface⁷⁹. To let go, geckos change the angle of their toes, peeling the setae away from the surface, which reduces the van der Waals forces and allows them to detach⁷⁹. Here, considering that mussels need to constantly and rapidly regulate their adhesive strength in

unpredictable environments—ranging from turbulent water flows to pulling forces from predators—the mussel also favors the utilization of an adhesive system apparently dependent on van der Waals forces. In addition, the finding on the presence of billions of macroscopic motile cilia in intimate contact with the lamella suggests a function similar to that of gecko setae. This raises intriguing questions about the mechanisms within the cilia that could enable such adhesive interactions.

Cilia exhibit different types of collective motion, categorized based on their coordination and movement patterns⁸⁰. For instance, in metachronal motion, cilia move in a wave-like pattern with a phase delay between adjacent cilia, which enhances the efficiency of fluid transport⁸⁰. In contrast, asynchronous motion occurs when cilia beat independently, a behavior commonly observed in environments where local control of fluid flow is prioritized over global coordination⁸⁰. Although the specific type of motion exhibited by the cilia in at the living/non-living of the stem root is unknown, observations suggest they may function as separate subgroups (movie S2.1). Therefore, this implies that cilia may attempt to adopt different beating patterns, leading to varying spatial adhesive forces. As a result, the cilia will perhaps produce a weaker adhesive effect compared to scenarios where all the cilia beat synchronously, leading to less efficient attachment, depending on the phase relationship. Moreover, the beating frequencies of individual cilia may contribute to the processes. At higher speeds, maintaining precise coordination among the distinct cilia groups becomes challenging. This leads to small phase lag between cilia and reduced control over the balance between adhesive and detachment

forces generated by the ciliary motion. Conversely, slower beating of cilia can result in longer attachment times, potentially enhancing adhesion stability on lamellae surfaces.

An additional mechanism that can enhance interface strength is the mechanical interlocking between the septa and the lamellae. This phenomenon occurs at a larger scale and is primarily influenced by the micro- or macrostructure of the contact surfaces, with the objective of generating frictional forces. For instance, the remora's sucker features mineralized, aligned spines that interlock with the host's skin surface, facilitating the generation of high friction 81. The adhesion resulting from this mechanical interlocking mechanism is only compromised if the interlocking structures are subjected to deformation, such as fracture or bending⁸¹. While the contribution of these forces is possible, other mechanisms could also influence the regulation of the overall adhesive strength. Motile cilia can create directional upward strokes and push the soft lamellae sheets by its coordinated forces. During the recovery stroke, the cilium could in fact push the sheet downward, but such force is typically less intense compared to the effective stroke, as the cilium is in a relaxed state and the motion is often more fluid82. Cilia might also generate a propagating wave (metachronal motion)80, which could facilitate the movement of the sheet in the direction of the wave, resulting in a net upward displacement. However, proving these speculations can be challenging, as our interface is embedded within the tissue, and isolating it from the organism may disrupt the normal ciliary response by inadvertently triggering the mussel's nervous system.

Nevertheless, to regulate cilia movement, mussels must have relied on physical cues, especially given the constant mechanical stress exerted on the interface by the pulling of the byssus. This phenomenon, known as mechanotransduction, involves the transmission of mechanical forces into cellular responses. For example, when force-dependent regions of specific proteins are stretched, it can change the geometry and dimensions of the connections at the interface, as well as influence the spatial organization of signals associated with these proteins⁸³. To delve deeper into the mechanotransduction pathways, they can be categorized as follows: (1) structural domains that bear forces, unfolding under high force and refolding when the force diminishes, (2) disordered regions that adopt a more extended conformation under higher forces and a compact, random coil conformation under lower forces, (3) force-dependent rates of dissociation at protein-protein interfaces, (4) forces applied to exposed binding sites that alter their binding affinity with partners, and (5) forces applied to structural domains with cryptic binding sites, potentially relieving autoinhibition and activating binding interactions⁸³. Such processes predominantly take place at adhesion sites between the cell and its surrounding environment, including the extracellular matrix (ECM) and neighboring cells⁸³.

The relevance of mechanotransduction can be seen in MSP-1, which was seen to undergo a force-induced transition from an alpha-helix to a beta-sheet structure (Chapter 3). Positioned at the interface of the stem and the living tissue, particularly the cilia, which is well known for its role in signal transduction, signifies that MSP-1 is key component in responding to mechanical stresses. Previous research has explored the behavior of lamin filaments- structurally analogous to MSP-1 - under mechanical stress within the meshwork⁸⁴. The distinct regions of the stress-strain curve

were linked to molecular alterations in the α -helical coiled-coil structure of lamin⁸⁴. It was observed that a low-force regime precedes a sharp increase in stiffness, signifying strain-induced stiffening due to formation of beta sheets, that eventually results in filament failure⁸⁴. Yet, interestingly, at low forces, around 0.5 nN, lamins undergo reversible unfolding or sliding of the α-helical coiled-coil (rod domain)⁸⁴. This process acts as an initial protective mechanism, buffering mechanical shock to the nucleus and preserving the structural integrity of the lamina and nuclear contents⁸⁴. Conversely, once the yield point is reached, between 1.0 and 1.5 nN, plastic deformation begins, indicating an irreversible structural change⁸⁴. Assuming a similar regime in the MSP-1, while considering that the lamellae is heterogeneous (includes preCols in the core), the molecular changes in MSP-1 IFs will not evenly occur across the OLL. Since the core of the lamellae is made of a preCols, which will dissipate a significant amount of energy when the byssus is stretched, it is possible that the structural transition to beta sheet in MSP-1 will happen in a gradient, from at the core to the periphery of the OLL, that is the interface with cilia (depending on the magnitude of the force). Perhaps, at low forces, the transition may not even occur at the periphery of the OLL, or if it does, in a reversible manner, as observed in lamins. Therefore, this can create a "structural shield" to impede the response of cilia at low forces, presuming that the transition from alpha helices into beta sheets initiates cilia movement by some unknown biochemical pathways. In addition, the fact that it happens irreversibly at higher forces, signifies that this conversion is done just once for a specific purpose, such as escaping environments with extreme forces that can rupture the internal organs of the mussel tissue, strengthening the hypothesis on mechanosensory role in stem release as previously discussed.

Saying that, to fully understand the relationship between the cilia and the MSP-1, further neurochemical and biochemical characterization is required on the cilia.

Regardless of the ultimate purpose, it is for mussel's benefit to sustain itself with such a protein, while not over-fabricating it, since byssus assembly is energy consuming. Many organisms, such as caddisflies, velvet worms, sharks, whelks, squids, and including mussels, developed stimuliresponsive processes for the fabrication of high-performance material, which are often mechanochemical alterations such as pH changes and mechanical shearing³³. For instance, in mussels, prior to the secretion of plaque proteins, such precursors are stockpiled within a specialized plaque gland in spherical secretory vesicles³³. During secretion, vesicles are transported through numerous branching microchannels known as longitudinal ducts (LDs) that run through the plaque glands, resembling a microfluidic droplet process wherein the contents mix as they advance toward the distal depression of the mussel foot where the plaque is formed ³³. The proteins within the vesicles are stored as coacervates, under acidic and reducing conditions to later enable the spontaneous ex-vivo self-assembly of the plaque underwater. Here, according to the STEM and immunostaining images, the MSP-1 is stored in membrane-bound organelles in the ECM at the interface, which are highly possible to be transported through type III UPS pathway⁸⁵. Interestingly, the organelles involved in the UPS pathway can convert to secretory organelles after induction by stress⁸⁶. Similarly, MSP-1 might be secreted whenever mussels experience pulling forces to produce additional stem material that provides support for anchoring threads.

Nevertheless, the mechanism that drives the self-assembly of MSP-1 IFs into microfibrils to form the stem material, once released from the membrane, remains unclear at this point. This contrasts with preCols, where it is known that the liquid crystalline core vesicles isolated from mussels form fibers⁷⁶. Yet, studies on keratins, also classified as IFs, within wool and hair follicle cells, suggest that they behave in the same way as other systems of chiral rod-like macromolecules, with the added feature that, the mesophase may be either nematic or cholesteric⁸⁷. In addition, TEM images of a keratin IFs are seen to be arranged on a hexagonal basal lattice, with approximately a diameter of 7.5 nm, and the overall structure that is similar to that of other acknowledged liquid crystal structures, such as that of spider silk fibrils prior to extrusion⁸⁷. Other studies using X-ray diffraction showed that wool and quill alpha-helices lie approximately parallel to the long axis of the intermediate and are about 45 nm long constituting filaments only 10 nm in diameter⁸⁸ – dimensions comparable to the MSP-1 intermediate filaments previously mentioned. Part of such molecular packing of the coiled-coil rod domain lies in the regular linear distribution of acidic and basic residues that occur in the two segments⁸⁸. The acidic residues, aspartic acid and glutamic acid, having a highly significant periodicity, along with the basic residues, arginine and lysine, are out of phase with one another⁸⁸. This means that there are alternating bands of acidic and basic residues along both segments, which indicate that molecular assembly is likely to be specified to some extent by the maximization of intermolecular ionic interactions⁸⁸. Nevertheless, to apply these insights into the complex molecular and atomic assembly processes of MSP-1 assembly, highly interdisciplinary effort from various perspectives, including genomics/transcriptomics, material characterization, and chemistry is required. Overall, this process can enhance our understanding of how biochemical pathways integrate with

external stimuli to reveal the adaptability and regulatory mechanism governing the interface adhesion and cilia function in response to environmental changes.

ii) Design of "bespoke" graded polymers based on the distal/proximal gradient Another mechanism mussels have adapted to efficiently withstand mechanical stresses is reflected in the remarkable performance of their byssal threads, which combine extensibility with high stiffness for outstanding functionality. Such synergistic enhancement effects arise from the functional gradient established at the soft-hard interface between the proximal and distal regions. In this thesis, I have identified that such gradient formation is driven by the incorporation of diverse chemical components to achieve localized properties, particularly changes in stiffness within approximately 150 micrometers of length, which is relatively short compared to the overall length of the threads (1-2cm). In fact, it was shown that the localization of precursors in the core gland is crucial for creating the distinct proximal and distal portions of the thread and its interface. Yet, the formation of gradients with varying lengths at different locations of the thread —despite the precursor being stored in the same glands at opposite ends of the foot indicates that a highly regulated assembly process is necessary. This process may be facilitated by foot muscle contractions, enabling the precise mixing of different components at specific locations within the groove to finally crosslink into a graded fiber. Such compositional distribution of proteins plays a fundamental role in dictating the structure of proteins, and particularly in this study, the structure of the preCols fibers which are mainly composed of collagen.

Collagen is key component of biological materials found in heart, aorta, cornea and tendon⁸⁹, it varies in diameter and crimp period and amplitude – properties that have an important bearing on the mechanical properties⁹⁰. In tendons, the crimp structure functions like a spring, storing energy during stretching and releasing it when the load is removed^{88, 90}. This allows the fibers to efficiently transmit force from muscles to bones, with the crimp pattern tailored to meet the specific mechanical demands of the tissue^{88, 91}. In the byssus, crimping is partial at the transition region (relative to the proximal region), with varying diameters and periodicity of the waves possibly due to the presence of ptmp-1 around the preCol-P fibrils⁹². This likely enables the fiber to redistribute stress more evenly across the interface and accommodate both the elastic stretching of the crimped proximal portion and the stiffer properties of the straightened collagen fibers in the distal portion⁹³.

In addition to the crimps, the secondary structures in the elastin-like and beta sheet flanking domains of preCols play a pivotal role in the transition region, as described in Chapter 4. In fact, several organisms are known to integrate elastic and stiff proteins at the molecular level to develop multifunctional materials. For instance, the nanostructure of silk fibrils comprises two primary components: semi-amorphous regions and beta-sheet nanocrystals⁹⁴. The beta-sheet nanocrystals are embedded within a soft matrix, creating a composite structure. During stretching, the semi-amorphous regions unravel first, enabling silk's remarkable extensibility⁹⁴. On the other hand, the ultimate tensile strength and large-deformation mechanical properties of silk are governed by the robust beta-sheet nanocrystals⁹⁴. Similarly, the arthropod cuticle integrates chitin nanofibrils, which are composed of rigid crystalline and flexible amorphous

regions⁹⁵. These nanofibrils are stacked to form a layered structure that underpins the exoskeleton's exceptional load-bearing capacity⁹⁵. This combination is uniform throughout the entire material in silk and the cuticle, yet, in the byssus, it is confined to the transition region between the distinct byssus ends. Thus, this highlights that by solely manipulating nanoscale structures, it is possible to tailor material properties at the microscale without introducing new material constituents.

Understanding how such protein combinations are distributed within biological materials has inspired researchers to tune the mechanical properties of engineered protein-based materials⁹⁶. Particularly, structural proteins such as silk, squid ring teeth, elastin, collagen, and resilin have been a source of inspiration due to their tunable structural and mechanical features (e.g., β-sheets, helices, and nanofibrils)⁹⁶. With the advances in genetic engineering, the modification of amino acid sequences or domain composition of these proteins became conceivable, facilitating the biofabrication of high molecular weight recombinant structural proteins with monomer-level sequence control and low dispersity⁹⁶. This allows the exploration of novel structural proteins beyond those shaped by natural evolution⁹⁶. More importantly, by integrating the structural and functional attributes of natural proteins into de novo recombinant proteins, researchers can engineer new protein-based materials with properties defined from the molecular scale upward⁹⁶.

Particularly relevant to this topic are the engineered 'fusion proteins', which combine two or more types of tandem repeats into a single polypeptide chain⁹⁶. These are typically designed to

merge distinct mechanical and structural properties into a single biopolymer 96 . One of the most widely studied examples of fusion proteins is silk–elastin-like polypeptides , which combine ordered silk-like β -sheet-forming blocks with disordered, stimuli-responsive elastin-like blocks (VPGXG) in varying ratios 96 . Such fusion proteins provide a platform to fine-tune material properties, and potentially enables precise control over the properties at interfaces through the formation of gradient 96 , tuning the overall mechanics of the fiber. The core proteins of the byssus can be here a promising candidate. Still, it is worth mentioning that there has not been an optimal mechanical design identified for a byssus for a specific function since no evidence has been found to correlate the different gradient designs or the distal/proximal proportions in various threads with the external factors.

In order to apply this approach to protein building blocks, researchers have identified an effective strategy by employing a combined method that integrates materials engineering and digital processing⁹⁷. Such a strategy enables extrusion-based multimaterial additive manufacturing of tunable viscoelastic materials with continuous, high-contrast, and multidirectional stiffness gradients (e.g., cellulose-based materials) ⁹⁷. Specifically, custom code was developed to control three-dimensional printers and syringe pumps, allowing for the extrusion of filaments with varying compositions and/or cross-sections⁹⁷. The filaments are extruded in a solution phase, facilitating molecular diffusion across filament boundaries to create continuous gradients⁹⁷. By leveraging that precise control, it may also be possible to manipulate mussel proteins as well. For example, syringe pump diameters can be adjusted to mimic the dimensions of the mussel foot groove, enabling precise protein fusion along its length. Although such precise control of

biopolymers is a critical aspect of engineering functional materials, it represents only a portion of the complexity inherent in natural systems. The remarkable properties exhibited by many natural materials, such as hierarchical organization, and dynamic responsiveness—are predominantly achieved through the collaborative interplay between living cells and the non-living biopolymeric materials embedded within them ⁹⁶. Indeed, an emerging field of engineered living materials (ELMs) has been inspired by the complexity of natural systems and aims to blend polymeric materials with genetically modified cells to create synthetic materials with advanced functionality ⁹⁶. Materials, either fossil fuel-based polymers or natural biopolymers, are combined with engineered cells, ultimately to enable materials 'grow' autonomously, starting from a simple growth medium or implantation within engineered cells ⁹⁶. Recombinant structural proteins have emerged as a promising solution, since they provide a biocompatible framework that supports cell function ⁹⁶.

As a proof-of-concept, studies showcased recombinant fusion proteins inspired by natural systems, such as curli proteins and elastin⁹⁶. They were shown to self-assemble into soft, adaptable materials⁹⁶. While we are not yet at the stage of engineering living-ciliated cells that respond directly to mechanical cues, our model system lays a crucial foundation for advancing the function of living and non-living materials, particularly through its efficient release mechanism. Notably, substantial research has focused on developing artificial cilia that replicate the movement of biological cilia⁹⁸. Inspired by nature, these artificial structures are being designed for applications in microfluidic systems, such as lab-on-a-chip and organ-on-a-chip platforms⁹⁸. By leveraging actuation mechanisms—such as magnetic or electric fields—artificial

cilia can provide precise control and enhanced functionality for various advanced biomedical applications such as brain-machine interfaces and adaptive implants.

6. Final Conclusions and Summary

In recent years, bio-inspired design has emerged as an important approach in advancing materials science, particularly in the development of biomedical devices such as implants, prosthetics and brain machine interfaces⁹. Despite the promising potential of these technologies, many devices fail due to the mechanical mismatch between soft tissues and rigid components, leading to stress concentrations at the interface¹. Additionally, complications may arise when devices need to be removed from tissues, i.e. improper tissue detachment from the device, leading to inflammation⁴⁰. While nature effectively mitigates stress concentrations at junctions between mechanically dissimilar components through functional gradients³⁷, there have been few examples of strong yet easily releasable mechanisms. In this thesis, I focused on how mussels serve as an ideal model for understanding the regulation of strength, detachment, and potential mechanosensing at living-nonliving interfaces, as well as how to design gradients between soft and hard interfaces. These topics were addressed in the following chapters:

In **Chapter 2**, I concentrated on the biointerface between the non-living mussel byssus stem root and living tissue. Mussels possess the remarkable ability to jettison their byssus and regenerate a new one in just a few hours—a process that remains poorly understood despite its biological significance. Using advanced techniques such as histology, confocal Raman mapping, phase contrast-enhanced microcomputed tomography, and electron microscopy, I characterized the complex structure and composition of this biointerface. The results revealed a sophisticated junction, consisting of biopolymer sheets interdigitated with living extracellular matrix. This interface is in intimate adhesive contact with motile epithelial cilia that control the strength of

the biointerface and mediate stem release through their collective movement, which is regulated by neurochemical signaling. I propose that this neurochemical regulation involves a complex sensory pathway through which mussels respond to environmental stresses, ultimately allowing them to release and relocate their byssus. This chapter contributes to our understanding of how mussels control their adhesion strength, offering new insights into the design of bioinspired interfaces for applications in soft robotics and biomimetic adhesion systems.

Chapter 3 of this thesis delved into the identification of a novel protein within the mussel byssus stem root. This protein, which resembles intermediate filaments (IF-like), was localized in the non-collagenous portion of the byssus matrix. Using antibody staining, I was able to pinpoint the protein's specific localization within the lamella and the secretory vesicles. Spectroscopic analysis and X-ray diffraction data indicated that this protein is secreted in an alpha-helical conformation but can be mechanically converted into a beta-sheet structure, a transformation that is likely to have importance for mechanical purposes. I hypothesize that the protein's ability to transition from an alpha-helix to a beta-sheet may play a crucial role in toughening the interface between the byssus and the living tissue, enhancing the byssus's mechanical performance. Moreover, the protein's structural transition may serve as a solid-state mechanosensory mechanism, enabling mussels to adapt to varying mechanical stresses in their environment. This discovery not only opens new paths for designing biomaterials with dynamic mechanical responses that can adapt to changes in environmental conditions.

Finally, in Chapter 4 of this thesis, I investigated the structure, function, and formation of the mechanical gradient in mussel byssal threads, using a cross-disciplinary experimental approach. It was known that the mechanical properties of these fibers vary significantly from the elastomeric proximal end to the stiff distal end. Yet, how such mismatch is mitigated at the interface had not been fully elucidated. To address this gap, I applied a combination of tensile testing, video extensometry, confocal Raman spectroscopy, and transmission electron microscopy on native byssal threads. The results revealed a continuous, graded transition in mechanics, composition, and nanofibrillar morphology that spans several hundred microns and can vary significantly between individual threads. Furthermore, in conjunction with Dr. Max Renner-Rao's studies on characterizing purified secretory vesicles from both the proximal and distal regions of the mussel's secretory glands, it was discovered that vesicles spontaneously selfassemble, in correlation with their local distribution across the foot, into distinct proximal- and distal-like fiber morphologies. These findings offer valuable insights not only into the structure and function of the byssus but also into the fabrication processes that drive the formation of functionally graded interfaces. Moreover, these results provide design principles for the development of tunable bioinspired polymeric materials.

7. Main References

- (1) Long, Y.; Li, J.; Yang, F.; Wang, J.; Wang, X. Wearable and Implantable Electroceuticals for Therapeutic Electrostimulations. *Adv Sci (Weinh)* **2021**, *8* (8), 2004023. DOI: 10.1002/advs.202004023 From NLM.
- (2) Magisetty, R.; Park, S. M. New Era of Electroceuticals: Clinically Driven Smart Implantable Electronic Devices Moving towards Precision Therapy. *Micromachines (Basel)* **2022**, *13* (2). DOI: 10.3390/mi13020161 From NLM.
- (3) Seymour, R. B. Surfaces, interfaces, and colloids—principles and applications, by Drew Myers, VCH, Weinheim, Germany, 1991, 433 pp. *Journal of Polymer Science Part A: Polymer Chemistry* **1992**, *30* (7), 1507-1507. DOI: https://doi.org/10.1002/pola.1992.080300732.
- (4) Jeevahan, J.; Chandrasekaran, M.; Britto Joseph, G.; Durairaj, R. B.; Mageshwaran, G. Superhydrophobic surfaces: a review on fundamentals, applications, and challenges. *Journal of Coatings Technology and Research* **2018**, *15* (2), 231-250. DOI: 10.1007/s11998-017-0011-x.
- (5) Zhang, J. Bonding at Surfaces/Interfaces. In *Encyclopedia of Tribology*, Wang, Q. J., Chung, Y.-W. Eds.; Springer US, 2013; pp 247-249.
- (6) Horiuchi, S.; Terasaki, N.; Miyamae, T. Introduction—Interfaces in Adhesion and Adhesive Bonding. In *Interfacial Phenomena in Adhesion and Adhesive Bonding*, Horiuchi, S., Terasaki, N., Miyamae, T. Eds.; Springer Nature Singapore, 2024; pp 1-15.
- (7) Scognamiglio, F.; Travan, A.; Rustighi, I.; Tarchi, P.; Palmisano, S.; Marsich, E.; Borgogna, M.; Donati, I.; de Manzini, N.; Paoletti, S. Adhesive and sealant interfaces for general surgery applications. *Journal of Biomedical Materials Research Part B: Applied Biomaterials* **2016**, *104* (3), 626-639. DOI: https://doi.org/10.1002/jbm.b.33409.

- (8) Berglundh, T.; Persson, L.; Klinge, B. A systematic review of the incidence of biological and technical complications in implant dentistry reported in prospective longitudinal studies of at least 5 years. *Journal of Clinical Periodontology* **2002**, *29* (s3), 197-212. DOI: https://doi.org/10.1034/j.1600-051X.29.s3.12.x.
- (9) Sandak, A.; Butina Ogorelec, K. Bioinspired building materials—lessons from nature. *Frontiers in Materials* **2023**, *10*, Review. DOI: 10.3389/fmats.2023.1283163.
- (10) Winkler, S. M.; Harrison, M. R.; Messersmith, P. B. Biomaterials in fetal surgery. *Biomater Sci* **2019**, *7* (8), 3092-3109. DOI: 10.1039/c9bm00177h From NLM.
- (11) Bonham, V.; Roberts, D. Mytilus edulis (common blue mussel). *CABI Compendium* **2022**. DOI: 10.1079/cabicompendium.73755.
- (12) Nowotny, S.; Berger, L.-M.; Spatzier, J. 1.18 Coatings by Laser Cladding. In *Comprehensive Hard Materials*, Sarin, V. K. Ed.; Elsevier, 2014; pp 507-525.
- (13) Huang, X.; Etsion, I.; Shao, T. Effects of elastic modulus mismatch between coating and substrate on the friction and wear properties of TiN and TiAlN coating systems. *Wear* **2015**, *338*-339, 54-61. DOI: https://doi.org/10.1016/j.wear.2015.05.016.
- (14) Cui, W.; Qin, G.; Duan, J.; Wang, H. A graded nano-TiN coating on biomedical Ti alloy: Low friction coefficient, good bonding and biocompatibility. *Materials Science and Engineering: C* **2017**, *71*, 520-528. DOI: https://doi.org/10.1016/j.msec.2016.10.033.
- (15) Vishwakarma, V.; Kaliaraj, G. S.; Kirubaharan, A. M. K. Advanced Alloys and Coatings for Bioimplants. *Coatings* **2022**, *12* (10), 1525.

- (16) Waite, J. H.; Lichtenegger, H. C.; Stucky, G. D.; Hansma, P. Exploring molecular and mechanical gradients in structural bioscaffolds. *Biochemistry* **2004**, *43* (24), 7653-7662. DOI: 10.1021/bi049380h From NLM.
- (17) Huang, G.; Wang, L.; Wang, S.; Han, Y.; Wu, J.; Zhang, Q.; Xu, F.; Lu, T. J. Engineering three-dimensional cell mechanical microenvironment with hydrogels. *Biofabrication* **2012**, *4* (4), 042001. DOI: 10.1088/1758-5082/4/4/042001.
- (18) Gasik, M.; Lambert, F.; Bacevic, M. Biomechanical Properties of Bone and Mucosa for Design and Application of Dental Implants. *Materials* **2021**, *14* (11), 2845.
- (19) Shrivas, S.; Samaur, H.; Yadav, V.; Boda, S. K. Soft and Hard Tissue Integration around Percutaneous Bone-Anchored Titanium Prostheses: Toward Achieving Holistic Biointegration.

 ACS Biomaterials Science & Engineering 2024, 10 (4), 1966-1987. DOI: 10.1021/acsbiomaterials.3c01555.
- (20) Liu, C.; Lin, J.; Tang, L.; Liu, Z.; Jiang, Z.; Lian, K. Design of metal-polymer structure for dental implants with stiffness adaptable to alveolar bone. *Composites Communications* **2021**, *24*, 100660. DOI: https://doi.org/10.1016/j.coco.2021.100660.
- (21) Mohammed Ibrahim, M.; Thulasingam, C.; Nasser, K. S.; Balaji, V.; Rajakumar, M.; Rupkumar, P. Evaluation of design parameters of dental implant shape, diameter and length on stress distribution: a finite element analysis. *J Indian Prosthodont Soc* **2011**, *11* (3), 165-171. DOI: 10.1007/s13191-011-0095-4 From NLM.
- (22) Portillo-Lara, R.; Tahirbegi, B.; Chapman, C. A. R.; Goding, J. A.; Green, R. A. Mind the gap: State-of-the-art technologies and applications for EEG-based brain-computer interfaces. *APL Bioeng* **2021**, *5* (3), 031507. DOI: 10.1063/5.0047237 From NLM.

- (23) Redolfi Riva, E.; Micera, S. Progress and challenges of implantable neural interfaces based on nature-derived materials. *Bioelectronic Medicine* **2021**, *7* (1), 6. DOI: 10.1186/s42234-021-00067-7.
- (24) Wang, X.; Sun, X.; Gan, D.; Soubrier, M.; Chiang, H.-Y.; Yan, L.; Li, Y.; Li, J.; Yu, S.; Xia, Y.; et al. Bioadhesive and conductive hydrogel-integrated brain-machine interfaces for conformal and immune-evasive contact with brain tissue. *Matter* **2022**, *5* (4), 1204-1223. DOI: https://doi.org/10.1016/j.matt.2022.01.012.
- (25) Qian, X.; Liao, C. Engineering liquid metal-based implantable electrodes toward brain-machine interfaces. *Health Sciences Review* **2023**, *9*, 100118. DOI: https://doi.org/10.1016/j.hsr.2023.100118.
- (26) Liu, H.; Xuan Gan, M.; Zhai, W.; Song, X. Design and additive manufacturing of root analogue dental implants: A comprehensive review. *Materials & Design* **2023**, *236*, 112462. DOI: https://doi.org/10.1016/j.matdes.2023.112462.
- (27) Reddy, M. S.; Sundram, R.; Eid Abdemagyd, H. A. Application of Finite Element Model in Implant Dentistry: A Systematic Review. *J Pharm Bioallied Sci* **2019**, *11* (Suppl 2), S85-s91. DOI: 10.4103/jpbs.Jpbs 296 18 From NLM.
- (28) Dunlop, J. W. C.; Weinkamer, R.; Fratzl, P. Artful interfaces within biological materials. *Materials Today* **2011**, *14* (3), 70-78. DOI: https://doi.org/10.1016/S1369-7021(11)70056-6.
- (29) Sandak, A.; Butina Ogorelec, K. Bioinspired building materials-lessons from nature. *Frontiers in Materials* **2023**, *10*, 15. DOI: 10.3389/fmats.2023.1283163.

- (30) Allameh, S. M.; Lenihan, A. Chapter 2 Introduction to bio-inspired materials: Design, processing and applications. In *Biomimicry for Materials, Design and Habitats*, Eggermont, M., Shyam, V., Hepp, A. F. Eds.; Elsevier, 2022; pp 25-56.
- (31) Lurie-Luke, E. Product and technology innovation: what can biomimicry inspire? *Biotechnol Adv* **2014**, *32* (8), 1494-1505. DOI: 10.1016/j.biotechadv.2014.10.002 From NLM.
- (32) Shinde, S.; Mane, R.; Vardikar, A.; Dhumal, A.; Rajput, A. 4D printing: From emergence to innovation over 3D printing. *European Polymer Journal* **2023**, *197*, 112356. DOI: https://doi.org/10.1016/j.eurpolymj.2023.112356.
- (33) Tan, Y. L.; Leow, Y.; Min Wong, J. H.; Loh, X. J.; Goh, R. Exploring Stimuli-Responsive Natural Processes for the Fabrication of High-Performance Materials. *Biomacromolecules* **2024**, *25* (9), 5437-5453. DOI: 10.1021/acs.biomac.4c00718.
- (34) Wang, Y.; Naleway, S. E.; Wang, B. Biological and bioinspired materials: Structure leading to functional and mechanical performance. *Bioactive Materials* **2020**, *5* (4), 745-757. DOI: https://doi.org/10.1016/j.bioactmat.2020.06.003.
- (35) Wickramasinghe, S.; Do, T.; Tran, P. Flexural behavior of 3D printed bio-inspired interlocking suture structures *MSAM* **2022**, *1* (2). DOI: 10.18063/msam.v1i2.9.
- (36) Ha, J.; Choi, S. M.; Shin, B.; Lee, M.; Jung, W.; Kim, H.-Y. Hygroresponsive coiling of seed awns and soft actuators. *Extreme Mechanics Letters* **2020**, *38*, 100746. DOI: https://doi.org/10.1016/j.eml.2020.100746.
- (37) Liu, Z.; Meyers, M. A.; Zhang, Z.; Ritchie, R. O. Functional gradients and heterogeneities in biological materials: Design principles, functions, and bioinspired applications. *Progress in Materials Science* **2017**, *88*, 467-498. DOI: https://doi.org/10.1016/j.pmatsci.2017.04.013.

- (38) Font Tellado, S.; Balmayor, E. R.; Van Griensven, M. Strategies to engineer tendon/ligament-to-bone interface: Biomaterials, cells and growth factors. *Advanced Drug Delivery Reviews* **2015**, *94*, 126-140. DOI: https://doi.org/10.1016/j.addr.2015.03.004.
- (39) Wang, D.; Zhang, X.; Huang, S.; Liu, Y.; Fu, B. S.-c.; Mak, K. K.-l.; Blocki, A. M.; Yung, P. S.-h.; Tuan, R. S.; Ker, D. F. E. Engineering multi-tissue units for regenerative Medicine: Bone-tendon-muscle units of the rotator cuff. *Biomaterials* **2021**, *272*, 120789. DOI: https://doi.org/10.1016/j.biomaterials.2021.120789.
- (40) Adler, L.; Buhlin, K.; Jansson, L. Survival and complications: A 9- to 15-year retrospective follow-up of dental implant therapy. *J Oral Rehabil* **2020**, *47* (1), 67-77. DOI: 10.1111/joor.12866 From NLM.
- (41) Berglundh, T.; Persson, L.; Klinge, B. A systematic review of the incidence of biological and technical complications in implant dentistry reported in prospective longitudinal studies of at least 5 years. *J Clin Periodontol* **2002**, *29 Suppl 3*, 197-212; discussion 232-193. DOI: 10.1034/j.1600-051x.29.s3.12.x From NLM.
- (42) Abyzova, E.; Dogadina, E.; Rodriguez, R. D.; Petrov, I.; Kolesnikova, Y.; Zhou, M.; Liu, C.; Sheremet, E. Beyond Tissue replacement: The Emerging role of smart implants in healthcare. *Materials Today Bio* **2023**, *22*, 100784. DOI: https://doi.org/10.1016/j.mtbio.2023.100784.
- (43) Aguilera, M. A.; Thiel, M.; Ullrich, N.; Luna-Jorquera, G.; Buschbaum, C. Selective byssus attachment behavior of mytilid mussels from hard- and soft-bottom coastal systems. *Journal of Experimental Marine Biology and Ecology* **2017**, *497*, 61-70. DOI: https://doi.org/10.1016/j.jembe.2017.09.009.

- (44) Denny, M. W.; Gaylord, B. Marine ecomechanics. *Ann Rev Mar Sci* **2010**, *2*, 89-114. DOI: 10.1146/annurev-marine-120308-081011 From NLM.
- (45) PRICE, H. A. STRUCTURE AND FORMATION OF THE BYSSUS COMPLEX IN MYTILUS (MOLLUSCA, BIVALVIA). *Journal of Molluscan Studies* **1983**, *49* (1), 9-17. DOI: 10.1093/oxfordjournals.mollus.a065695 (acccessed 1/2/2025).
- (46) Carrington, E.; Waite, J. H.; Sarà, G.; Sebens, K. P. Mussels as a Model System for Integrative Ecomechanics. *Annual Review of Marine Science* **2015**, *7* (Volume 7, 2015), 443-469. DOI: https://doi.org/10.1146/annurev-marine-010213-135049.
- (47) Lamarck, J.-B.-P.-A. d. M. d. Histoire naturelle des animaux sans vertèbres ... précédée d'une introduction offrant la détermination des caractères essentiels de l'animal, sa distinction du végétal et des autres corps naturels, enfin, l'exposition des principes fondamentaux de la zoologie; Verdière, 1815.
- (48) Boston Society of Natural, H.; Boston Society of Natural, H.; Boston Society of Natural, H. *Proceedings of the Boston Society of Natural History*; Boston Society of Natural History, 1848.
- (49) McDonald, J. H.; Seed, R.; Koehn, R. K. Allozymes and morphometric characters of three species of Mytilus in the Northern and Southern Hemispheres. *Marine Biology* **1991**, *111*, 323-333.
- (50) Inoue, K.; Onitsuka, Y.; Koito, T. Mussel biology: from the byssus to ecology and physiology, including microplastic ingestion and deep-sea adaptations. *Fisheries Science* **2021**, *87* (6), 761-771. DOI: 10.1007/s12562-021-01550-5.

- (51) Bell, E. C.; Gosline, J. M. Mechanical Design of Mussel Byssus: Material Yield Enhances Attachment Strength. *Journal of Experimental Biology* **1996**, *199* (4), 1005-1017. DOI: 10.1242/jeb.199.4.1005 (acccessed 1/2/2025).
- (52) Coyne, K. J.; Waite, J. H. In Search Of Molecular Dovetails in Mussel Byssus: From The Threads to The Stem. *Journal of Experimental Biology* **2000**, *203* (9), 1425-1431. DOI: 10.1242/jeb.203.9.1425 (acccessed 1/2/2025).
- (53) Waite, J. H.; Andersen, N. H.; Jewhurst, S.; Sun, C. Mussel Adhesion: Finding the Tricks Worth Mimicking. *The Journal of Adhesion* **2005**, *81* (3-4), 297-317. DOI: 10.1080/00218460590944602.
- (54) Priemel, T.; Degtyar, E.; Dean, M. N.; Harrington, M. J. Rapid self-assembly of complex biomolecular architectures during mussel byssus biofabrication. *Nature Communications* **2017**, *8* (1), 14539. DOI: 10.1038/ncomms14539.
- (55) Holten-Andersen, N.; Mates, T. E.; Toprak, M. S.; Stucky, G. D.; Zok, F. W.; Waite, J. H. Metals and the Integrity of a Biological Coating: The Cuticle of Mussel Byssus. *Langmuir* **2009**, *25* (6), 3323-3326. DOI: 10.1021/la8027012.
- (56) Hagenau, A.; Papadopoulos, P.; Kremer, F.; Scheibel, T. Mussel collagen molecules with silk-like domains as load-bearing elements in distal byssal threads. *Journal of Structural Biology* **2011**, *175* (3), 339-347. DOI: https://doi.org/10.1016/j.jsb.2011.05.016.
- (57) Bailey, A. J.; Macmillan, J.; Shrewry, P. R.; Tatham, A. S.; Waite, J. H.; Vaccaro, E.; Sun, C.; Lucas, J. M. Elastomeric gradients: a hedge against stress concentration in marine holdfasts? *Philosophical Transactions of the Royal Society of London. Series B: Biological Sciences* **2002**, *357* (1418), 143-153. DOI: doi:10.1098/rstb.2001.1025.

- (58) Suhre, M. H.; Gertz, M.; Steegborn, C.; Scheibel, T. Structural and functional features of a collagen-binding matrix protein from the mussel byssus. *Nature Communications* **2014**, *5* (1), 3392. DOI: 10.1038/ncomms4392.
- (59) Qin, X.; Waite, J. H. Exotic Collagen Gradients in the Byssus of the Mussel Mytilus Edulis. Journal of Experimental Biology 1995, 198 (3), 633-644. DOI: 10.1242/jeb.198.3.633 (acccessed 1/2/2025).
- (60) Coyne, K. J.; Qin, X. X.; Waite, J. H. Extensible collagen in mussel byssus: a natural block copolymer. *Science* **1997**, *277* (5333), 1830-1832. DOI: 10.1126/science.277.5333.1830 From NLM.
- (61) Waite, J. H.; Qin, X.-X.; Coyne, K. J. The peculiar collagens of mussel byssus. *Matrix Biology* **1998**, *17* (2), 93-106. DOI: https://doi.org/10.1016/S0945-053X(98)90023-3.
- (62) Reinecke, A.; Bertinetti, L.; Fratzl, P.; Harrington, M. J. Cooperative behavior of a sacrificial bond network and elastic framework in providing self-healing capacity in mussel byssal threads. *Journal of Structural Biology* **2016**, *196* (3), 329-339. DOI: https://doi.org/10.1016/j.jsb.2016.07.020.
- (63) Qin, X. X.; Waite, J. H. A potential mediator of collagenous block copolymer gradients in mussel byssal threads. *Proc Natl Acad Sci U S A* **1998**, *95* (18), 10517-10522. DOI: 10.1073/pnas.95.18.10517 From NLM.
- (64) Waite, J. H.; Harrington, M. J. Following the thread: Mytilus mussel byssus as an inspired multi-functional biomaterial. *Canadian Journal of Chemistry* **2022**, *100* (3), 197-211. DOI: 10.1139/cjc-2021-0191.

- (65) Vincent, L.; Engler, A. J. 5.504 Effect of Substrate Modulus on Cell Function and Differentiation. In *Comprehensive Biomaterials*, Ducheyne, P. Ed.; Elsevier, 2011; pp 51-63.
- (66) Abbasi, M.; Abdollahzadeh, A.; Bagheri, B.; Ostovari Moghaddam, A.; Sharifi, F.; Dadaei, M. Study on the effect of the welding environment on the dynamic recrystallization phenomenon and residual stresses during the friction stir welding process of aluminum alloy. *Proceedings of the Institution of Mechanical Engineers, Part L: Journal of Materials: Design and Applications* **2021**, *235* (8), 1809-1826. DOI: 10.1177/14644207211025113.
- (67) Harrington, M. J.; Waite, J. H. Holdfast heroics: comparing the molecular and mechanical properties of Mytilus californianus byssal threads. *Journal of Experimental Biology* **2007**, *210* (24), 4307-4318. DOI: 10.1242/jeb.009753 (acccessed 1/2/2025).
- (68) Vaccaro, E.; Waite, J. H. Yield and Post-Yield Behavior of Mussel Byssal Thread: A Self-Healing Biomolecular Material. *Biomacromolecules* **2001**, *2* (3), 906-911. DOI: 10.1021/bm0100514.
- (69) Schmitt, C. N. Z.; Politi, Y.; Reinecke, A.; Harrington, M. J. Role of Sacrificial Protein–Metal Bond Exchange in Mussel Byssal Thread Self-Healing. *Biomacromolecules* **2015**, *16* (9), 2852-2861. DOI: 10.1021/acs.biomac.5b00803.
- (70) Callister, W. D.; Rethwisch, D. G. *Materials science and engineering : an introduction*; Wiley, 2020.
- (71) Gosline, J.; Lillie, M.; Carrington, E.; Guerette, P.; Ortlepp, C.; Savage, K. Elastic proteins: biological roles and mechanical properties. *Philos Trans R Soc Lond B Biol Sci* **2002**, *357* (1418), 121-132. DOI: 10.1098/rstb.2001.1022 From NLM.

- (72) Harrington, M. J.; Waite, J. H. How Nature Modulates a Fiber's Mechanical Properties: Mechanically Distinct Fibers Drawn from Natural Mesogenic Block Copolymer Variants. *Advanced Materials* **2009**, *21* (4), 440-444. DOI: https://doi.org/10.1002/adma.200801072.
- (73) Tamarin, A. An ultrastructural study of byssus stem formation in Mytilus californianus. Journal of Morphology 1975, 145 (2), 151-177. DOI: https://doi.org/10.1002/jmor.1051450204.
- (74) Roberts, E. A.; Newcomb, L. A.; McCartha, M. M.; Harrington, K. J.; LaFramboise, S. A.; Carrington, E.; Sebens, K. P. Resource allocation to a structural biomaterial: Induced production of byssal threads decreases growth of a marine mussel. *Functional Ecology* **2021**, *35* (6), 1222-1239. DOI: https://doi.org/10.1111/1365-2435.13788.
- (75) Côté, I. M. Effects of predatory crab effluent on byssus production in mussels. *Journal of Experimental Marine Biology and Ecology* **1995**, *188* (2), 233-241. DOI: https://doi.org/10.1016/0022-0981(94)00197-L.
- (76) Jehle, F.; Priemel, T.; Strauss, M.; Fratzl, P.; Bertinetti, L.; Harrington, M. J. Collagen Pentablock Copolymers Form Smectic Liquid Crystals as Precursors for Mussel Byssus Fabrication.

 ACS Nano 2021, 15 (4), 6829-6838. DOI: 10.1021/acsnano.0c10457.
- (77) Pitta Kruize, C.; Panahkhahi, S.; Putra, N. E.; Diaz-Payno, P.; van Osch, G.; Zadpoor, A. A.; Mirzaali, M. J. Biomimetic Approaches for the Design and Fabrication of Bone-to-Soft Tissue Interfaces. *ACS Biomaterials Science & Engineering* **2023**, *9* (7), 3810-3831. DOI: 10.1021/acsbiomaterials.1c00620.
- (78) Federle, W.; Labonte, D. Dynamic biological adhesion: mechanisms for controlling attachment during locomotion. *Philosophical Transactions of the Royal Society B: Biological Sciences* **2019**, *374* (1784), 20190199. DOI: doi:10.1098/rstb.2019.0199.

- (79) Tian, Y.; Pesika, N.; Zeng, H.; Rosenberg, K.; Zhao, B.; McGuiggan, P.; Autumn, K.; Israelachvili, J. Adhesion and friction in gecko toe attachment and detachment. *Proceedings of the National Academy of Sciences* **2006**, *103* (51), 19320-19325. DOI: doi:10.1073/pnas.0608841103.
- (80) Cui, Z.; Wang, Y.; den Toonder, J. M. J. Metachronal Motion of Biological and Artificial Cilia. *Biomimetics* **2024**, *9* (4), 198.
- (81) Burn, A.; Schneiter, M.; Ryser, M.; Gehr, P.; Rička, J.; Frenz, M. A quantitative interspecies comparison of the respiratory mucociliary clearance mechanism. *European Biophysics Journal* **2022**, *51* (1), 51-65. DOI: 10.1007/s00249-021-01584-8.
- (82) Gueron, S.; Levit-Gurevich, K. Energetic considerations of ciliary beating and the advantage of metachronal coordination. *Proc Natl Acad Sci U S A* **1999**, *96* (22), 12240-12245. DOI: 10.1073/pnas.96.22.12240 From NLM.
- (83) Guo, Y.; Yan, J.; Goult, B. T. Mechanotransduction through protein stretching. *Current Opinion in Cell Biology* **2024**, *87*, 102327. DOI: https://doi.org/10.1016/j.ceb.2024.102327.
- (84) Zhmurov, A.; Kononova, O.; Litvinov, R. I.; Dima, R. I.; Barsegov, V.; Weisel, J. W. Mechanical transition from α -helical coiled coils to β -sheets in fibrin(ogen). *J Am Chem Soc* **2012**, *134* (50), 20396-20402. DOI: 10.1021/ja3076428 From NLM.
- (85) Rabouille, C. Pathways of Unconventional Protein Secretion. *Trends in Cell Biology* **2017**, *27* (3), 230-240. DOI: 10.1016/j.tcb.2016.11.007 (accessed 2025/01/02).
- (86) Maricchiolo, E.; Panfili, E.; Pompa, A.; De Marchis, F.; Bellucci, M.; Pallotta, M. T. Unconventional Pathways of Protein Secretion: Mammals vs. Plants. *Front Cell Dev Biol* **2022**, *10*, 895853. DOI: 10.3389/fcell.2022.895853 From NLM.

- (87) McKinnon, A. J. The self-assembly of keratin intermediate filaments into macrofibrils: Is this process mediated by a mesophase? *Current Applied Physics* **2006**, *6* (3), 375-378. DOI: https://doi.org/10.1016/j.cap.2005.11.022.
- (88) Parry, D. A. D.; Steinert, P. M. Intermediate filaments: molecular architecture, assembly, dynamics and polymorphism. *Quarterly Reviews of Biophysics* **1999**, *32* (2), 99-187. DOI: 10.1017/S0033583500003516 From Cambridge University Press Cambridge Core.
- (89) Pelley, J. W. 20 Tissue Biochemistry. In *Elsevier's Integrated Biochemistry*, Pelley, J. W. Ed.; Mosby, 2007; pp 179-190.
- (90) Joyce, E. M.; Liao, J.; Schoen, F. J.; Mayer, J. E., Jr.; Sacks, M. S. Functional collagen fiber architecture of the pulmonary heart valve cusp. *Ann Thorac Surg* **2009**, *87* (4), 1240-1249. DOI: 10.1016/j.athoracsur.2008.12.049 From NLM.
- (91) Wang, J. H. C. Mechanobiology of tendon. *Journal of Biomechanics* **2006**, *39* (9), 1563-1582. DOI: https://doi.org/10.1016/j.jbiomech.2005.05.011.
- (92) Golser, A. V.; Scheibel, T. Routes towards Novel Collagen-Like Biomaterials. *Fibers* **2018**, *6*. DOI: 10.3390/fib6020021.
- (93) Meyers, M. A.; Chen, P.-Y.; Lin, A. Y.-M.; Seki, Y. Biological materials: Structure and mechanical properties. *Progress in Materials Science* **2008**, *53* (1), 1-206. DOI: https://doi.org/10.1016/j.pmatsci.2007.05.002.
- (94) Nova, A.; Keten, S.; Pugno, N. M.; Redaelli, A.; Buehler, M. J. Molecular and Nanostructural Mechanisms of Deformation, Strength and Toughness of Spider Silk Fibrils. *Nano Letters* **2010**, *10* (7), 2626-2634. DOI: 10.1021/nl101341w.

- (95) Oh, D.; Cha, Y. J.; Nguyen, H.-L.; Je, H.; Jho, Y.; Hwang, D.; Yoon, D. Chiral nematic self-assembly of minimally surface damaged chitin nanofibrils and its load bearing functions. *Scientific Reports* **2016**, *6*, 23245. DOI: 10.1038/srep23245.
- (96) Shire, E.; Coimbra, A. A. B.; Barba Ostria, C.; Rios-Solis, L.; López Barreiro, D. Molecular design of protein-based materials state of the art, opportunities and challenges at the interface between materials engineering and synthetic biology. *Molecular Systems Design & Engineering* **2024**, *9* (12), 1187-1209, 10.1039/D4ME00122B. DOI: 10.1039/D4ME00122B.
- (97) Giachini, P. A. G. S.; Gupta, S. S.; Wang, W.; Wood, D.; Yunusa, M.; Baharlou, E.; Sitti, M.; Menges, A. Additive manufacturing of cellulose-based materials with continuous, multidirectional stiffness gradients. *Science Advances* **2020**, *6* (8), eaay0929. DOI: doi:10.1126/sciadv.aay0929.
- (98) UI Islam, T.; Wang, Y.; Aggarwal, I.; Cui, Z.; Eslami Amirabadi, H.; Garg, H.; Kooi, R.; Venkataramanachar, B. B.; Wang, T.; Zhang, S.; et al. Microscopic artificial cilia a review. *Lab Chip* **2022**, *22* (9), 1650-1679. DOI: 10.1039/d1lc01168e From NLM.